A MASS-WEIGHTED UPWIND-BASED CONTROL VOLUME FINITE-ELEMENT METHOD FOR STEADY TWO-DIMENSIONAL VISCOUS COMPRESSIBLE FLOWS

HAO ZHOU

A MASS-WEIGHTED UPWIND-BASED CONTROL VOLUME FINITE-ELEMENT METHOD FOR STEADY TWO-DIMENSIONAL VISCOUS COMPRESSIBLE FLOWS

BY

HAO ZHOU

A thesis submitted to the School of Graduate Studies
in partial fulfillment of the requirements for the degree of
Master of Engineering

Faculty of Engineering & Applied Science
Memorial University of Newfoundland

April, 1997

St. John's Newfoundland Canada

ABSTRACT

The formulation and implementation of a mass-weighted upwind-based control volume finite element method (CVFEM) for steady, two-dimensional, viscous compressible internal flows is reported in this thesis. In the development of this method, a CVFEM for steady, quasi-one-dimensional, viscous compressible flows was also formulated. The proposed method is a colocated shock capturing formulation. Polygonal control volumes are constructed around each node in the finite-element mesh, and discretized forms of the governing equations are obtained by deriving algebraic approximations to integral conservation equations for each control volume.

The proposed methods are formulated using the velocity components, pressure, and temperature as the dependent variables: density is calculated from an equation of state. Linear interpolation is applied to pressure and diffused scalars, and a mass weighted upwind function is applied to the convected scalars. An interpolation function incorporating a pseudo-velocity and a pressure gradient is used to represent mass conserving velocities; this allows the development of a colocated method valid for compressible flows. The discretized forms of the governing equations are solved using an iterative algorithm. In this algorithm, linearized forms of the discretized momentum and continuity equations are solved in a segregated manner by using a tridiagonal matrix algorithm.

The proposed quasi-one- and two-dimensional CVFEM's are applied to several inviscid and viscous compressible fluid flow problems, and the solutions generated are compared with theoretical, numerical, and experimental results available in the literature. This comparison shows that the proposed CVFEM's can generate solutions that are in agreement with the expected physical behaviour of some com-

pressible flows and with the available results. The results suggest further research is required in the evaluation and enhancement of the mass-weighted interpolation functions currently used, however, as the shock smearing in the proposed method is excessive, and the accuracy of solution is not satisfactory.

ACKNOWLEDGEMENTS

I would like to take this opportunity to thank my supervisor, Dr. N.A. Hookey, for the patience, guidance, and support that he has extended towards me during the course of this research program. His critical reviews of my work and his dedication to teaching made my graduate studies at Memorial University of Newfoundland an enjoyable and rewarding experience.

I would like to thank the staff of the Center for Computer Aided Engineering for providing technical assistance and free computing time. The use of these computers greatly facilitated the computational work undertaken in this thesis.

Finally, the day-to-day support, love and encouragement that my wife Xiejun provided for me kept me on an even keel, and allowed me to remain focussed on my research.

Contents

List of Figures

List of Tables

Nomenclature

Symbol	Description
A	matrix of a system of linear equations
A_e	area of a triangular element
a_i, a_n, d_i	coefficients in the discretized forms of the x, y momentum and continuity equations
a, b, c	coefficients in the interpolation functions for p and ϕ^d
c_p	constant pressure specific heat
C_1, C_2, C_3	coefficients in the algebraic approximation of the integrated convection-diffusion flux across a control volume face
d	pressure coefficient derived from the momentum equations
det	determinant
ds	differential area
D_i^u, D_i^v	coefficients in the algebraic representation of the pressure gradients $(\frac{\partial p}{\partial x})$ and $(\frac{\partial p}{\partial y})$, respectively
E_1, E_2, E_3, F	coefficients in the algebraic approximation of the integrated mass flux across a control volume face
f	constant used in the MAW scheme
$\vec{g}$	mass flux vector
h	height of a duct in quasi-one-dimensional problems; half-height of the planar converging-diverging nozzle
h_B	height of the bump in a channel with a circular arc bump on one wall
$\vec{i}, \vec{j}$	unit vectors in the x and y directions, respectively

$\vec{J}$	combined convection-diffusion flux
k	thermal conductivity
L	length dimension
L_t	length of the convergent portion of the planar converging-diverging nozzle
L_e	length of the divergent portion of a converging-diverging nozzle
M	Mach number
$\dot{m}$	mass flow rate
N	total number of nodes in a discretized domain
$\vec{n}$	outward unit vector normal to the differential area ds, or to a boundary
p	pressure
R	gas constant
S	volumetric source term
$\mathcal{S}$	generalized source term that includes S and pressure gradients
S_c, S_p	coefficients in the linearized expression for the source terms
Δs	area of a control volume surface
T	temperature
$\hat{u}, \hat{v}$	pseudo-velocities (derived from the momentum equations)
u, v	velocity components in the x and y directions, respectively
$\vec{v}$	velocity vector
$\Delta V, \partial V$	control volume, and surface of the control volume, respectively
x, y	axes and coordinates in the Cartesian coordinate system

Greek Symbols

α	under-relaxation parameter

β	angle of the wall in the divergent portion of a converging-diverging nozzle
δ_x, δ_L	boundary layer thickness at a position x, and at the end of a calculation domain, respectively
Γ	diffusion coefficient for ϕ
$\epsilon_i^u, \epsilon_i^v, \epsilon_i^p, \epsilon_i^T$	normalized change in u_i, v_i, p_i and T_i, respectively. between two successive iterations
θ	oblique shock angle in a shock-boundary layer interaction; angle of the wall in the convergent portion of a planar converging-diverging nozzle
μ	dynamic viscosity
Φ	nodal value of ϕ
ρ	mass density
ϕ	scalar dependent variable
Ω	calculation domain

Subscripts

aft	post-shock conditions in quasi-one-dimensional problems
av	average value within an element
$calc$	calculated value
e	denotes an element
e, E, w, W, P	values at locations in a one-dimensional finite-volume grid
i	value at node i
$ip1, ip2, ip3$	integration points 1, 2 and 3 used in the MAW scheme, respectively
M	value at the midpoint of a side of a triangular element
max, min	maximum and minimum values, respectively

n	neighbour node of node i
o	stagnation conditions
O	value at the centroid of an element
shk	conditions at a shock in the test problems
$spec$	specified value
u, v, p, T, ρ, ϕ	identify the coefficients in the u, v, p, T, ρ, ϕ interpolation functions, respectively
th	value at the throat of a converging-diverging nozzle
x, y	components in the x and y directions, respectively
y	conditions after a shock in two-dimensional problems
$1, 2$	inlet and exit conditions in the test problems
$1, 2, 3$	values at nodes 1, 2 and 3, respectively

Superscripts

k	control volume face k, where $k = 1, 2, 3$
$*$	calculated value from a previous iteration
$\sim$	denotes terms which result from the linearization of the mass flow, or flux, with respect to velocity
$\bullet$	denotes terms which result from the linearization of the mass flow, or flux, with respect to density
$\circ$	denotes terms which result from the evaluation of the mass flow, or flux, using available values of density and velocity
$\vec{}$	denotes a vector quantity

Chapter 1

Introduction

1.1 Aims and Motivation of the Thesis

The primary purpose of this thesis is to develop a mass-weighted upwind-based Control Volume Finite Element Method (CVFEM) for steady, two-dimensional, viscous compressible internal fluid flow problems. The method will be valid for use over a wide range of Mach numbers, from subsonic to supersonic flow speeds. The proposed method is the result of an effort to enhance the capabilities of some of the earlier CVFEM's [1]-[13] developed for two-dimensional compressible and/or incompressible flows. The proposed CVFEM is developed from the works of Hookey [9] and Saabas [10]. The secondary goal of this thesis is to test the "mass weighted" interpolation function proposed by Schneider and Raw [11] and implemented later by Saabas [10] in the context of compressible flows.

The computer simulation of the flows of interest requires: (1) a mathematical model of the physical problem, which in its general form, includes partial differential equations and boundary conditions that govern the distribution of the unknown dependent variables in the region of interest; (2) a numerical method for the solution of the mathematical model in regular- and irregular-shaped calculation domains; and (3) a computer implementation of the numerical method. The mathematical

model in conjunction with a given numerical solution procedure is referred to as a numerical model. In this thesis, emphasis is placed on the development of a numerical solution procedure. The mathematical model used is not new. Briefly, it assumes the fluid is an ideal gas that is compressible and Newtonian, and the two-dimensional Navier-Stokes equations and the continuity equation govern the motion of the fluid.

The CVFEM proposed in this thesis employs three-node triangular elements to discretize two-dimensional calculation domains. Each element is further discretized in such a way that upon assembly of all elements, control volumes are formed around each node in the calculation domain. Element-based interpolation functions for the dependent variables and the subdomain-type Method of Weighted Residuals (MWR) is used to derive algebraic approximations to the governing equations. In conventional finite element methods (FEM's), the Galerkin method of weighted residuals is used, where the weighting and interpolation functions are equivalent. In CVFEM's, however, for each node in the calculation domain, the weighting function is set equal to one over a suitably chosen control volume associated with the node, and zero elsewhere. Control volume finite element methods for fluid flow and heat transfer, therefore, involve the imposition of physical conservation principles on finite control volumes in the calculation domain, which makes them amenable to easy physical interpretation, and their solutions satisfy global conservation requirements, even for coarse grids.

The proposed method is restricted to the solution of steady two-dimensional flows, however, its basic formulation can be extended to unsteady flows using the procedures described in [14]. In addition, extensions to three-dimensional problems can be performed by incorporating the ideas from the CVFEM proposed by Saabas [10]. In the formulation of the proposed CVFEM, the fluid is assumed to be a

perfect gas with constant specific heat. Although realistic compressible flows are usually turbulent, the proposed CVFEM has been developed in the context of the well understood physical behaviour of laminar Newtonian fluid flows, mainly to facilitate the formulation, implementation, and testing of the proposed method.

The CVFEM's in [1]–[13] are conservative[1]: their formulations ensure conservation of the appropriate scalar variables over contiguous and non-overlapping control volumes, and consistent calculation of fluxes across the boundaries of the control volumes, which together ensure conservation of the appropriate dependent variables over the control volume and the calculation domain [22]. The proposed CVFEM, which is an extension of those in [1]–[13], is also conservative. In addition, it may be classified as a shock capturing or smearing method: all discontinuities, such as shocks, are automatically captured by the method, but these discontinuities are smeared over several grid points. Discontinuous or extremely rapid changes in the dependent variables are approximated by finite gradients. The degree of smearing induced depends on the manner in which the integral conservation is enforced, and the type of interpolation functions used. Shock capturing methods are in contrast to shock fitting methods, where shocks are treated as internal boundaries in the calculation domain, and are, therefore, maintained as sharp discontinuities: the Rankine-Hugoniot relations [16] and satisfaction of flow compatibility conditions are used to determine conditions across the shock. In shock fitting methods, the presence of shocks must be known a priori, however, shock capturing methods do not require such knowledge, as all discontinuities within the flow field are automatically captured. The compressible flow CVFEM proposed by Hookey [9] was also a shock capturing method, but employed adaptive grids to reduce the physical

[1]Those finite-difference schemes which maintain the discretized version of the conservation statement exactly (except for round-off errors) for any mesh size over an arbitrary finite region containing any number of grid points are said to have the *conservative property [30].*

smearing of shocks inherent to such methods. The proposed CVFEM attempts to address problems experienced at incompressible outflow boundaries when using the CVFEM of Hookey [9]. The interpolation schemes used by Saabas [10] were successful in avoiding these difficulties in a colocated CVFEM for incompressible flow. The proposed CVFEM will, therefore, attempt to incorporate the successful portion of both CVFEM's into one method.

Since the proposed numerical method was developed in a CVFEM context, no review will be given to the other numerical methods for compressible or incompressible fluid flow, for example the methods developed in the context of finite-difference methods (FDM's), finite-volume methods (FVM's), and finite-element methods (FEM's). A rather thorough review of these methods can be found in [9].

1.2 A Review of CVFEM's

Control volume finite element methods offer a combination of the geometric flexibility of finite element methods and the ease of physical interpretation associated with finite volume methods. The formulation of a CVFEM involves the following steps [4]:

1. Discretization of the calculation domain into elements, and a further discretization into control volumes associated with the nodes of each element.

2. Prescription of appropriate element-based interpolation functions for the dependent variables.

3. Derivation of discretization equations, which are algebraic approximations to the governing differential equations. The subdomain method of weighted residuals is used to derive algebraic forms of the integral conservation equation for each control volume.

4. An element by element assembly of the discretization equation.

5. Prescription of a procedure to solve the resulting discretization equations.

The main features that distinguish the CVFEM's that have been developed for the simulation of fluid flow problems are the type of discretization, interpolation, and solution techniques employed. The choice of interpolation function is influenced by the domain discretization employed, as only certain functions are applicable to the desired equal-order (or colocated) discretization. The following subsections review the CVFEM's that have been developed for the simulation of incompressible and/or compressible fluid flows, and the types of interpolation schemes used in these methods.

1.2.1 CVFEM's for Fluid Flow Problems

It has been demonstrated by Patankar [14] that an unrealistic and checkerboard numerical solution can result when a linear interpolation scheme is used for pressure. Similar difficulties are also encountered in the discretization of the continuity equation if both velocity and density are interpolated linearly [9]. In the proposed method, density is calculated using the equation of state and is expressed in terms of pressure. To avoid unrealistic solutions, special precautions are necessary if a colocated storage scheme is to be used.

One way to avoid such difficulties in orthogonal grid FDM's is the use of staggered grids to store velocity components and pressure at different locations in the calculation domain [14]. An advantage of grid staggering is that pressures are stored at the faces of the momentum control volumes, which ensures that pressures at adjacent, not alternate, nodes are used to evaluate the pressure gradients in the momentum equations. Similarly, checkerboard density and velocity fields would be prevented due to the staggered storage [9]. The limitations of this staggered

storage are that two different families of control volumes are used for the momentum and continuity equations, and mass conservation is not strictly satisfied over the momentum control volumes. Further, two different control volume sets lead to tedious and complicated bookkeeping, and these difficulties are compounded in three-dimensional flow problems.

An unequal-order CVFEM for incompressible flows was proposed by Baliga and Patankar [1]. In this method, the domain is first discretized by six-node triangular elements. These "macroelements" are then divided into four three-node "subelements" by joining the midpoints each side of a macroelement. Pressure is stored at the vertices of the macroelements, and velocity is stored at the vertices of all subelements, which results in an unequal-order scheme that avoids pressure harmonics in the solution. A mixed order interpolation scheme is applied to this formulation in which pressure is interpolated linearly in the macroelements, and the velocity components are interpolated by flow-oriented upwind type functions within the subelements. Polygonal control volumes used to discretize the continuity equation are constructed around the vertices of the macroelements, while those used to discretize the momentum equations are constructed around the vertices of the subelements. This formulation has been used in conjunction with SIMPLE, SIMPLER, and SIMPLEC [2, 6, 8] solution algorithms. Several disadvantages are associated with this formulation, because of the use of two types of elements and control volumes: (1) mass conservation is not strictly satisfied over the momentum control volumes and the velocities at the vertices of the macroelements do not explicitly enter the discretized continuity equation; (2) the discretized equation for pressure is quite different from that of the other dependent variables and a separate equation solver is required; (3) the two different control volume sets lead to tedious and complicated bookkeeping, and these difficulties would be compounded

in three-dimensions; (4) excessively fine grids for velocity, and thus an expensive computation, are needed in problems with relatively large pressure gradients since the velocity discretization is finer than the pressure discretization in this method; and (5) given an equal number of velocity nodes, an equal-order discretization would provide a much better approximation of boundary irregularities than this unequal-order formulation.

To circumvent the problems associated with the unequal-order storage methods, Prakash and Patankar [3] introduced a CVFEM using an equal-order velocity-pressure interpolation, where pressure and velocity nodes are colocated. Within each element, the velocity components (when treated as transported scalars) are interpolated using flow-oriented (FLO) upwind functions (without source term effects), and the pressure is interpolated linearly. The mass flow field is obtained from linear interpolation of a pseudo-velocity field and pressure. The domain discretization again involves the formation of polygonal control volumes about each node in the calculation domain. The velocities in the continuity equation are interpolated by using a modified form of the discretized momentum equation derived for that control volume. The velocity at each node is split into two parts: one is a function of the nodal velocities and any volumetric source term (excluding the pressure gradient); and the other is related to the appropriate pressure gradient over that control volume. Consequently, at each node within the domain, a pseudo-velocity field and a pressure coefficient can be defined. These two values are then interpolated linearly within each element, to provide an interpolation scheme for the 'mass conserving' velocities. When interpolating the 'mass conserving' velocities within an element, the element pressure gradient is used in conjunction with a pressure coefficient. In this way, spurious harmonics in the pressure field, commonly encountered in early equal-order FEM's are avoided. A SIMPLER type algorithm is used

to solve the resulting discretization equations. This method has been extended to three-dimensions by LeDain Muir and Baliga [15].

In an attempt to refine his previous equal-order method, Prakash [4] proposed a second method. Here, the interpolation of velocity within an element is performed using flow-oriented upwind type functions that include the effects of pressure gradients and other source terms in the stream direction (FLOS). The same interpolation function is used to derive algebraic approximations to both the momentum and continuity equations. It is the explicit inclusion of the appropriate pressure gradients in the velocity interpolation functions that prevents the appearance of spurious oscillations of velocity and pressure. Pressure is interpolated linearly. But convergence difficulties have been reported by Prakash [4] when a SIMPLEC solution scheme is applied to solve the discretized momentum and continuity equations.

Hookey and Baliga [7, 8] modified the interpolation function of Prakash [4] to include source term effects in directions parallel and normal to the mean flow within each element. Furthermore, they introduced a SIMPLEC type solution algorithm in which they derived very complete pressure-correction equations [9]. The resulting pressure-correction equation, however, involved up to twenty-five neighbouring nodes in two-dimensional problems, and this would make extensions to three-dimensional problems impractical. In [9], Hookey successfully reduced the number of neighbouring nodes in the discretized equations. The maximum neighbouring nodes for two-dimensional problems was reduced to eight for both pressure and velocity equations. This method was, therefore, better suited for three-dimensional formulations. The discretized momentum and continuity equations were solved in a coupled manner using a Coupled Equation Line Solver (CELS). The CELS solves the coupled equations simultaneously along a grid line in the calculation domain, and iteratively improves the overall solution by successively sweeping the domain

line by line, in alternating directions, until a desired level of convergence is obtained [9].

In [11]-[13], Schneider and Raw have also proposed an equal-order colocated CVFEM. Based on quadrilateral elements rather than triangular elements, this CVFEM also uses different interpolation functions: linear interpolation is applied to the diffusion terms, a MAss Weighted (MAW) upwind scheme is used for convection terms, and the convection terms in the momentum equations explicitly include the pressure gradients to couple the velocity and pressure fields to prohibit harmonic pressure fields. The use of triangular elements is believed to be more efficient for irregular-shaped domains and adaptive grid methods, because triangular elements allow more freedom in the placement of nodes within the calculation domain. Schneider and Raw used a direct banded solver for the solution of the algebraic discretization equations of two-dimensional problems. In three-dimensions, the cost of such a solution method is prohibitive.

Combining a modified version of the MAW upwind scheme in triangular elements with the use of a pseudo-velocity field and the pressure gradient to define 'mass conserving' velocities, Saabas [10] developed an equal-order CVFEM for the simulation of three-dimensional turbulent incompressible fluid flow. This method overcomes the problems with outflow boundaries inherent with the method developed by Hookey [9], and forms the basis for the CVFEM developed in this thesis for the simulation of compressible flows.

1.2.2 Interpolation Schemes

As discussed in the previous subsection, there are some basic considerations involved in the solution of fluid flow problems to prevent spurious solutions in colocated CVFEM's. The equal-order CVFEM's that have been developed have used some

form of coupling between pressure and velocity, usually at the interpolation function levels, to prevent solution harmonics. The development of appropriate interpolation functions must also consider the following: (1) prevention of negative coefficients in the discretized equations; (2) minimization of false diffusion that arises due to locally one-dimensional upwinding; and (3) suitable coupling between velocity and pressure to permit colocated methods. This subsection discusses the interpolation functions used in the previous CVFEM's, and presents the interpolation functions used in the proposed CVFEM.

Linear interpolation was applied successfully in early FDM's for heat transfer problems. But it gave physically unrealistic oscillatory solutions for convection-diffusion problems when the grid Peclet number was greater than two [14]. This difficulty occurred, because linear interpolation of the convection term gave rise to negative coefficients in the discretization equations and this led to divergence. Attempts to overcome this difficulty led to the development of upwind difference schemes [9].

In the CVFEM's of Baliga et al. [1]–[10], the dependent variables are interpolated by flow-oriented upwind type functions. These functions eliminate the oscillatory solutions that occur with linear interpolation of convection terms, and provide a more realistic approximation of the physical behaviour of the dependent variable within an element. To reduce false diffusion, which may be incurred when locally one-dimensional upwinding is used, the interpolation functions are defined with respect to a locally flow-oriented co-ordinate system specific to each element. These functions are derived by solving a simplified version of the appropriate governing equation within the element, written in terms of flow-oriented coordinates. In [4], a source term was included in the interpolation function to provide for a source-related variation of the dependent variable in a direction parallel to the lo-

cal flow direction. In [6, 7, 8], this source-related term was modified to account for a source influence in directions both parallel and normal to the local flow direction. The inclusion of this source term was shown to improve the quality of solution in convection-diffusion problems involving sources [6, 7].

It was found that formulations that included source effects, especially the pressure gradient, in the element-based interpolation functions for the convected scalar, allow for equal-order colocated formulations in flow problems [6, 7]. Thus, this approach appears attractive: the same interpolation function can be used for velocities in the momentum and continuity equations, and spurious oscillations of the pressure or velocity fields can be avoided.

It is not necessary, however, to use the same interpolation functions in both continuity and momentum equations. It may actually be disadvantageous to do so. The basic philosophy when developing an interpolation function should be to choose the appropriate, and physically meaningful, type of interpolation for the terms in which the interpolated scalar appears. This was done in Prakash and Patankar [3], where the velocity was interpolated using an upwind scheme for the convective term, and a linear scheme for the diffusion and 'extra viscous terms', and the 'mass conserving' velocity was linearly interpolated by a pseudo-velocity and pressure gradient.

In the context of quadrilateral elements, Schneider and Raw [11] introduced a positive-coefficient upwinding procedure, in which the coefficients that arise due to the algebraic approximation of the convection fluxes are assured to be positive at an elemental level, and hence at a control volume level. In [12], an upwinding formulation was presented that was similar in form to the positive coefficient scheme, however, the directionality of the flow was more closely approximated, reducing false diffusion, but allowing for the appearance of some negative coefficients. For

the problems tested, it was found that the magnitude of the negative coefficients were such that they did not pose any difficulties. The effects of diffusion, both parallel and normal to the mean flow direction, and source terms, were also explicitly accounted for in the interpolation function for the convected scalar. In this method, the pressure gradients were included in the interpolation functions for velocities at an elemental level, this interpolation scheme allowed for the development of an equal-order colocated formulation for incompressible flow problems.

In the context of triangular elements, Prakash [5] introduced the donor-cell CVFEM scheme as a means of ensuring positive coefficients. This approach stated that the value of a dependent variable convected out of a control volume must be the value of the dependent variable at the node within the control volume. Although it guarantees positive coefficients, this approach takes little account of the directionality of the flow, and takes no account of the effects of diffusion and source terms on the interpolation of the convected scalar. The positive influence coefficient scheme proposed by Schneider and Raw [11] is a more attractive approach to eliminate negative coefficients, even though it involves more computations.

In this thesis the MAW scheme developed by Saabas [10] will be used for the first time in the development of a CVFEM applied to compressible and incompressible flows. This interpolation will permit the development of a colocated method, and should eliminate the outflow difficulties in the CVFEM of Hookey [9] when it is used to solve purely incompressible flow problems.

1.3 Key Features in the Formulation of the Proposed CVFEM

For reasons of economy and simplicity, many ideas used in the proposed two-dimensional CVFEM were first tested in a quasi-one-dimensional formulation. The

derivation of both the one- and two-dimensional CVFEM's are presented in chapters 2 and 3, respectively. To avoid repetition, the key features in both formulations are discussed in this section. The topics included here are as follows: (1) choice of the dependent variables; (2) the necessity of special procedures for the colocated methods; (3) appropriate upwinding of the dependent variables; (4) linearization procedures for the governing equations; (5) physical boundary conditions and their numerical implementation; and (6) the solution methods used.

1.3.1 Dependent Variables

The proposed CVFEM's are based on the so-called primitive variables, i.e. the velocity components (u,v), temperature (T), and pressure (p). The continuity equation is used as an equation for pressure, the momentum equations are used to solve for the velocity components, the energy equation is solved for temperature, and density is calculated from an equation of state.

1.3.2 Colocated Dependent Variable Storage

A colocated storage is applied to all the dependent variables in the proposed CVFEM. To prevent spurious harmonic solutions the flow-oriented upwind type function proposed by Prakash and Patankar [3], in which the mass flow field in each element is determined from linear interpolation of pseudo-velocity and pressure fields, is employed. The use of the pseudo-velocity and pressure in the discretization of the continuity equation provides the necessary coupling between velocity and pressure. This method was formulated in the context of the SIMPLER solution algorithm [14]. Saabas [10] employed a similar method to colocated dependent variable storage in a three-dimensional incompressible CVFEM.

1.3.3 Upwinding of the Dependent Variables

The MAW scheme first introduced by Schneider and Raw [11] and later implemented by Saabas [10] in the context of a triangular element CVFEM, is used as the interpolation formula for the convected scalars in this thesis. As previously mentioned, the evaluation of the MAW scheme in the context of compressible flows is a secondary goal of this thesis.

1.3.4 Linearization Procedures

In CVFEM's, the discretized forms of the governing equations are obtained by formulating suitable algebraic approximations of integral conservation statements applied to control volumes constructed around each node in the calculation domain. In steady state problems, the conservation of a particular scalar variable requires a balance between the net transport of this variable out of the control volume by convection and diffusion fluxes, and the net generation of the variable within the volume. Volume integration of source terms is used to determine net generation, and net transport is evaluated from the integration of convection-diffusion fluxes over the surface of the control volume. These fluxes must be linearized in an appropriate manner with regard to the dependent variables in order to obtain the discretized equations. The solution to a fluid flow problem is obtained using an iterative procedure in which linearized discretization equations are solved during each iteration. The scheme used to linearize the mass flux is discussed in this section.

The derivation of the discretized form of the continuity equation involves integration of the mass flux, $\rho\vec{v}$, over the faces of a control volume. For compressible flows, the mass flux is nonlinear, and if it is linearized using densities from a previous iteration and treating velocity as the current unknown, convergence difficulties

could arise. In the steady acceleration of a supersonic flow through a diverging duct, when the density is initially assumed constant throughout the duct, the velocity would decrease to satisfy mass conservation. The decreased velocity would cause pressure to increase through momentum considerations. The increased pressure would lead to an increased density, when the equation of state is used to update density, which when substituted into the continuity equation further reduces the velocity. This numerical behaviour is opposite to that of the physical flow, and causes divergence.

Linearization of the mass flux can also be achieved using available velocities, and treating density implicitly, or as the current unknown. This approach, however, is viable only at high supersonic flow speeds, where changes in velocity become negligible. For a steady decelerating subsonic flow through a diverging duct, if the velocity is initially assumed to be constant throughout the duct, density would decrease to satisfy mass conservation. This change in density would cause pressure to decrease, through the equation of state, and when this decreased pressure is substituted into the momentum equations the velocity would increase. The increased velocity, when substituted into the continuity equation, would further decrease density, and this physically unrealistic behaviour continues until divergence.

To overcome these difficulties, a linearization that takes into account the roles of both density and velocity in the satisfaction of mass conservation has to be formulated. This is accomplished by recognizing the dual role of pressure in compressible flows: it acts on both velocity and density, through momentum and state equations, respectively, to ensure mass conservation. A suitable formulation involves a full Newton-Raphson linearization of the mass flux, $\vec{g}$:

$$\vec{g} = \vec{\tilde{g}} + \vec{\bullet}{g} - \vec{\circ}{g} \tag{1.1}$$

where, $\tilde{g}$ is linearized with respect to velocity, $\dot{g}$ is linearized with respect to density, and $\mathring{g}$ is evaluated from available values of both density and velocity.

1.3.5 Boundary Conditions

The necessary boundary conditions for a numerical solution of a fluid flow problem are discussed in this section. Further details on the implementation of these boundary conditions will be given in later chapters.

The boundary conditions applied to compressible flows depend upon the type of flow, subsonic or supersonic, that exists at the boundary in question. In this subsection, boundary conditions for inviscid subsonic and supersonic flows are discussed first, and then the boundary conditions for viscous flows will be presented.

Inviscid Subsonic Flows

At subsonic inflow boundaries, the velocity components, u, v, pressure, p, and temperature, T, are all specified. To define the mass entering the calculation domain it is necessary to specify the pressure, which, along with the specified temperature, is used to determine the density at inlet. This specified density, the inlet geometry, and the specified velocities together determine the inlet mass flow.

In subsonic inviscid flows, the influence of pressure is elliptic, as a pressure disturbance will eventually be felt everywhere in the calculation domain. The proposed numerical method accounts for this elliptic behaviour by interpolating pressure linearly. With this elliptic treatment, a downstream boundary condition for pressure becomes necessary. In the proposed method, the static pressure at outflow boundaries is specified.

The proposed method has been developed for viscous compressible flows, however, it may be used to solve for inviscid flows by setting viscosity equal to zero. At solid boundaries, a tangency condition is demanded by defining the dot product of

the velocity vector and a unit normal to the wall to be zero:

$$\vec{v} \cdot \vec{n} = 0 \tag{1.2}$$

At outflow boundaries, to ensure that no diffusive effects are encountered, the diffusion transport of momentum and energy is effectively set equal to zero using:

$$\vec{\nabla}\phi \cdot \vec{n} = 0 \tag{1.3}$$

where ϕ is a general scalar dependent variable.

Inviscid Supersonic Flows

In supersonic flows, as in subsonic flows, the specification of the inlet mass flow rate is required, and this is done by specifying u, v, p, and T at inflow boundaries.

Inviscid supersonic flows are hyperbolic, and outflow boundary conditions are not physically propagated upstream into the calculation domain, therefore, no boundary conditions are applied or needed at outflow boundaries. To allow solutions for inviscid flows with the proposed viscous CVFEM, the gradients of u, v, and T are set to zero at outflow boundaries using Eq. (1.3).

Viscous Compressible Flows

Viscous flows always have elliptic influences due to the presence of the viscous terms, however, the boundary conditions are very similar to those used for inviscid flows, except that the no-slip condition is always used on solid walls. Wall boundary conditions for the energy equation are either the fixed temperature value or adiabatic type, Eq. (1.3). Inflow boundary conditions are the same as for inviscid flows, but the elliptic behaviour that is now present requires special treatment at outflow boundaries. This special treatment is the same as that used in the solution

of inviscid flows with the proposed viscous flow CVFEM: it involves the specification of zero diffusion at the outflow boundary for velocity and temperature, using Eq. (1.3).

1.3.6 Solution of the Discretized Equations

In the proposed CVFEM, a coupled set of nonlinear algebraic equations for velocity, pressure, and temperature are obtained as approximations of the corresponding integral conservation equations. The nonlinearities in the equations are resolved by Picard iteration, in which the coefficients in these equations are evaluated using the most recent field values. A segregated solution method is used, rather than a coupled method, to solve the final algebraic equations. The segregated solution method is believed to have the following advantages: (1) less storage is required, as coefficients do not have to be stored simultaneously; and (2) the advancement in the solutions of each dependent variable do not have to be matched in each iteration. With regard to the second point, it is not necessary to solve for all the dependent variables to the same level of convergence in each iteration, emphasis can be placed on the solution of the pressure field in order to ensure that mass conservation is enforced more completely at each iteration. As the momentum equations are inherently nonlinear, and are solved through an iterative process, it is not necessary to solve the nominally linear algebraic equations exactly in each iteration. More detail about the solution procedures will be given in a later chapter.

1.4 Summary

The main ideas and motivations behind the development of the proposed CVFEM were presented in this chapter. The derivation of a CVFEM for quasi-one-dimensional CVFEM is presented in Chapter 2, the formulation of a two-dimensional CVFEM

is discussed in Chapter 3, and the testing of the proposed CVFEM formulations is presented in Chapter 4.

Chapter 2

Formulation of the Proposed Quasi-One-Dimensional CVFEM

2.1 Introduction

The main purpose of this thesis is to formulate and implement a CVFEM for steady, two-dimensional, viscous compressible fluid flows. For reasons of economy and simplicity, however, many ideas were initially tested in the context of quasi-one-dimensional problems. The following topics will be used to present the formulation of the one-dimensional CVFEM in this chapter: (1) definition of the governing equations; (2) domain discretization details; (3) derivation of control volume integral conservation equations; (4) specification of element-based interpolation functions for the dependent variables; and (5) derivation of discretized forms of the conservation equations and boundary conditions.

2.2 Governing Equations

The governing differential equations for steady, quasi-one-dimensional, viscous compressible flow of a perfect gas through a duct of variable area, w, are:

Continuity:

$$\frac{d}{dx}(\rho w u) = 0 \tag{2.1}$$

Momentum:

$$\frac{d}{dx}(\rho w u u) = -w\frac{dp}{dx} + \frac{d}{dx}\left(\mu w \frac{du}{dx}\right) + S^u w + \frac{1}{3}\frac{d}{dx}\left(\mu \frac{d}{dx}(uw)\right) \tag{2.2}$$

Energy:

$$\frac{d}{dx}(\rho w u T) = \frac{d}{dx}\left(\frac{k}{c_p} w \frac{dT}{dx}\right) + w\frac{S^T}{c_p} + \frac{1}{c_p}\left(uw\frac{dp}{dx}\right) \tag{2.3}$$

State:

$$\rho = \frac{p}{RT} \tag{2.4}$$

where u is the velocity, p is the pressure, ρ is the density, μ is the dynamic viscosity, T is the absolute temperature, k is the thermal conductivity, c_p is the specific heat at constant pressure. R is the gas constant, and S^u and S^T are the volumetric source, or generation, terms for the momentum and energy equation, respectively. The proposed CVFEM is formulated for variable fluid properties, but c_p was assumed constant mainly to keep the energy equation relatively uncomplicated. It should be noted that, if required, the viscous dissipation term may be included in S^T.

These differential equations may be cast in the following conservative forms [9]:

$$\frac{dJ}{dx} = Sw \tag{2.5}$$

$$\frac{dg}{dx} = 0 \tag{2.6}$$

where, J is the combined convection-diffusion transport, S is a source term, and g

is the mass flow, ρwu. Equation (2.5) represents the momentum equation when:

$$J = \rho wuu - \mu w\frac{du}{dx} \quad ; \quad S = S^u - \frac{dp}{dx} + \frac{1}{3w}\frac{d}{dx}\left(\mu\frac{d}{dx}(uw)\right) \tag{2.7}$$

and the energy equation when:

$$J = \rho wuT - \frac{k}{c_p}w\frac{dT}{dx} \quad ; \quad S = S_T = \frac{S^T}{c_p} + \frac{u}{c_p}\frac{dp}{dx} \tag{2.8}$$

Applying the appropriate conservation principle to a control volume V, which is fixed in space, integral forms of Eqs. (2.5) and (2.6) can be obtained:

$$\int_{\partial V}\frac{dJ}{dx}\,dx = \int_V Sw\,dx \tag{2.9}$$

$$\int_{\partial V}\frac{dg}{dx}\,dx = 0 \tag{2.10}$$

where ∂V is the surface of the control volume, and V is the volume of the control volume.

2.3 Domain Discretization

In the proposed equal-order one-dimensional CVFEM, the calculation domain is discretized by a distribution of nodes in the x direction, and all dependent variables are stored at all of the nodes. The variation in the area of the duct is approximated by a piecewise linear curve. Control volume (cv) faces are placed midway between the nodes in the calculation domain. A sample discretization of a variable area duct is illustrated in Fig. 2.1, with the duct shape shown by the solid line.

Piecewise linear approximation of the duct boundary does not provide as accurate a formulation as would result if the functional representation of the actual duct was used to define the area variation of the control volume. The linear area variation used here was chosen for its simplicity and generality, and also to be consistent with the proposed two-dimensional CVFEM, in which boundary surfaces

are approximated with piecewise linear curves. The placement of control volume faces midway between nodes was also chosen for simplicity. The control volumes employed fill the entire calculation domain, do not overlap, and their boundaries do not coincide with nodes, except at the domain boundary. These characteristics help to formulate a CVFEM that possesses the conservative property [30].

2.4 Integral Conservation Equations for a Control Volume

With reference to the control volume surrounding node i in Fig. 2.1, Eqs. (2.9) and (2.10) can be written as:

$$J_0 - \int_V Sw\, dx + \left(\begin{array}{l} \text{Similar contributions from other} \\ \text{elements associated with node } i \end{array} \right) + \left(\begin{array}{l} \text{Boundary contributions,} \\ \text{if applicable} \end{array} \right) = 0 \qquad (2.11)$$

$$g_0 + \left(\begin{array}{l} \text{Similar contributions from other} \\ \text{elements associated with node } i \end{array} \right) + \left(\begin{array}{l} \text{Boundary contributions,} \\ \text{if applicable} \end{array} \right) = 0 \qquad (2.12)$$

Where the subscript 0 indicates the centroid of the element 1-2, which by definition is the position of the control volume face.

2.5 Interpolation Functions

To derive algebraic approximations to the integral conservation equations, interpolation functions for the fluid properties, sources, duct area, and dependent variables must first be defined. The functions used in this thesis are described in this section.

2.5.1 Interpolation of μ, k, c_p, and S

Values of μ, k and c_p are supplied at the centroid of each element, and these centroidal values are assumed to prevail over the corresponding element. The source terms, S^u and S^T, in the momentum and energy equations, respectively, are linearized using Taylor's expansion [14], if required, and expressed as follows:

$$S^u = S_c^u + S_p^u u_{av} \tag{2.13}$$

$$S^T = S_c^T + S_p^T T_{av} \tag{2.14}$$

where S_c represents terms independent of the superscripted variable, and S_p provides for a linear dependence of S on the corresponding variable. The values of S_c and S_p are calculated at the centroid of each element, and assumed to prevail within the element. The average of the appropriate dependent variable, used in the linearized source term, is assumed to be the arithmetic mean of the corresponding values at the two nodes of the element.

2.5.2 Interpolation of Area

The variable area of a duct, w, is interpolated linearly within an element:

$$w = a_w x + b_w \tag{2.15}$$

this results in a piecewise linear approximation to the duct shape, as shown by the dashed lines in Fig. 2.1. The coefficients a_w and b_w in Eq. 2.15 are defined by the duct areas at the two nodes of the element, and the x coordinates of the nodes.

2.5.3 Interpolation of Pressure

Within an element, the pressure is interpolated linearly:

$$p = a_p x + b_p \tag{2.16}$$

The coefficients a_p and b_p in Eq. (2.16) are defined by the nodal pressures and x coordinates, as shown in Appendix A. Using Eq. (2.16), and the derivations in Appendix A, the pressure gradient can be expressed as follows:

$$\frac{dp}{dx} = a_p = \frac{p_1 - p_2}{x_1 - x_2} \tag{2.17}$$

Since a_p is constant within an element, $(-dp/dx)$ can be included in S_c^u, Eq. (2.13).

2.5.4 Interpolation of Velocity

In the proposed CVFEM, different functions are used to interpolate velocity in the convection and diffusion terms in Eq. (2.1), and in a mass conserving velocity used to evaluate the mass flow term ρwu.

Interpolation of a Convected Velocity

The MAW interpolation scheme [10] is used to evaluate velocity when it is a convected scalar. In the context of this one-dimensional CVFEM, the MAW scheme reduces to a pure upwind scheme, therefore, the value of the convected velocity on the cv face is simply the value of velocity at the upwind node.

$$\begin{aligned} &\text{if} \quad u_i > 0, \quad u_o = u_i \\ &\text{if} \quad u_i < 0, \quad u_o = u_{i+1} \end{aligned} \tag{2.18}$$

The MAW scheme will be discussed in Chapter 3.

Interpolation of Mass Conserving Velocity

The mass conserving velocity, u^m, which is used in the mass flow, ρwu, is interpolated by assuming a linear variation of a pseudo-velocity, $\hat{u}$, and pressure coefficient, d^u. The mass conserving velocity can be written as follows for each node within the domain:

$$u_i^m = \hat{u}_i - d_i^u \left(\frac{dp}{dx_i}\right)_e \tag{2.19}$$

where the subscript, e, on the pressure gradient indicates that the elemental pressure gradient is being used. The pseudo-velocity and pressure coefficients are evaluated from the discretized form of the momentum equation. If one divides the discretized momentum equation for node i, Eq. 2.27, by the coefficient multiplying u_i, then $\hat{u}_i$ is the sum of all terms on the R.H.S. of the equation, except for the pressure terms, divided by this coefficient; the pressure coefficient d_i^u is the volume of the control volume divided by the u_i coefficient.

The pseudo-velocities, $\hat{u}_i$, and the pressure coefficients, d_i^u, are known at the nodal points. In order to determine the values of these quantities on the control volume faces within an element, linear interpolation of the nodal values is used:

$$\hat{u}_i = a_{\hat{u}}\, x + b_{\hat{u}} \tag{2.20}$$

$$d_i^u = a_d^u\, x + b_d^u \tag{2.21}$$

The evaluation of the $\hat{u}_i$ and d_i^u terms will be discussed in Section 2.6.3.

Interpolation of a Diffused Velocity

When velocity is treated as a diffused scalar, for example in the viscous term of Eq. (2.2), it is interpolated linearly within an element.

2.5.5 Interpolation of Temperature

Temperature is interpolated in a similar manner to velocity. In convection terms, it is interpolated using the MAW, or pure upwind scheme:

$$\begin{aligned} &\text{if} \quad u_i > 0, \quad T_o = T_i \\ &\text{if} \quad u_i < 0, \quad T_o = T_{i+1} \end{aligned} \tag{2.22}$$

and in diffusion terms, the temperature is interpolated linearly:

$$T = a_T\, x + b_T \tag{2.23}$$

2.6 Derivation of the Discretized Equations

To obtain algebraic approximations of the integral conservation equations for a control volume, Eqs. (2.9) and (2.10), the element contributions to Eqs. (2.11) and (2.12) are derived and assembled in an appropriate manner. Algebraic approximations of the boundary contributions are then evaluated, if applicable, and added to the element contributions. The procedures involved in deriving algebraic approximations of the control volume integral conservation equation and the boundary conditions are described in this section.

2.6.1 Momentum Equation

Within each element, the combined convection-diffusion transport, Eq. (2.7), is evaluated at the control volume face, or centroid of the element, indicated by subscript 0. Substitution of the velocity interpolation functions into Eq. (2.7), and evaluating the expression at the control volume face gives:

$$J_0 = \left((\rho w u)_0 + \frac{\mu w_0}{x_2 - x_1}\right) u_1 - \frac{\mu w_0}{x_2 - x_1} u_2 \tag{2.24}$$

Rearranging J_0 in terms of the nodal velocities gives the following:

$$J_0 = c_1 u_1 + c_2 u_2 \tag{2.25}$$

Integration of the source term over the volume enclosed by the element is given by:

$$\int_{vol_1} S_u \, dx = S_c^u vol_1 + d_{11} u_1 + d_{12} u_2 + vol_1 \frac{dp}{dx} \tag{2.26}$$

Detailed derivations of the coefficients c_1, c_2, d_{11} and d_{12} in Eqs. (2.25) and (2.26) are included in Appendix B.

Expressions similar to Eq. (2.25) can be derived for the integrated flux across the control volume face in each element, and when these expressions are added,

appropriately, with the volume integrated source, Eq. (2.26), and any applicable boundary contribution, the discretized form of the integral equation representing conservation of momentum is completed. The resulting equation can be cast in the following form for a node i:

$$a_i^u u_i = \sum_n a_n^u u_n + b_i^u p_i + \sum_n b_n^u p_n + c_i^u \tag{2.27}$$

where the summation is over the two nodes that neighbour node i in Fig. 2.1. The assembly of Eq. (2.27) is demonstrated in Appendix C.

2.6.2 Energy Equation

The integral equation representing conservation of energy is discretized in a similar manner to the momentum equation, with the dynamic viscosity, μ, replaced by k/c_p, and S_u replaced by S_T. The integration of the convection-diffusion flux at the control volume face in an element, and the volume integration of the source term is described in Appendix B. The resulting algebraic approximation of the integral conservation equation can be written in the following form:

$$a_i^T T_i = \sum_n a_n^T T_n + b_i^T \tag{2.28}$$

The assembly of Eq. (2.28) is described in Appendix C.

2.6.3 Continuity Equation

Introduction

The discretization of the continuity equation will be discussed in this section. The approach taken here is to use particular forms of the discretized momentum equation, Eq. (2.27), to define two new nodal fields which will be used in the prescription of suitable interpolation functions for the mass conserving velocities. Equation

(2.27) can be rearranged as follows:

$$u_i = \frac{\sum a_n^u u_n + c_i^u}{a_i^u} - \frac{\overline{(\partial p/\partial x_i)}\Delta V}{a_i^u} \tag{2.29}$$

In this expression, $\overline{(\partial p/\partial x_i)}$ is the average of the pressure gradient acting over a control volume centered at node i of volume ΔV. Defining $\hat{u}_i$ and d_i^u as:

$$\hat{u}_i = \frac{\sum a_n^u u_n + c_i^u}{a_i^u} \tag{2.30}$$

$$d_i^u = \frac{\Delta V}{a_i^u} \tag{2.31}$$

then Eq. (2.29) can be rewritten as:

$$u_i = \hat{u}_i - d_i^u \frac{\overline{\partial p}}{\partial x_i} \tag{2.32}$$

Similar expressions can be written for each node in the computational domain. It should be noted that the pseudo-velocity, $\hat{u}_i$, and the pressure coefficient, d_i^u, fields should be evaluated before the discretized momentum equation is under-relaxed as will be considered in section 3.7.1. Furthermore, the Dirichlet boundary conditions on the velocity components (if any) are incorporated into the pseudo-velocity fields as follows: at the points where the velocity is specified, the appropriate $\hat{u}_i$ is set equal to the specified velocity, and the corresponding d_i^u is set equal to zero. In this way, the velocity information available on the boundary is incorporated directly into the discretized equation for continuity.

When the continuity equation is discretized, the mass flow is linearized with respect to density, ρ, and velocity, u:

$$\vec{g} = \vec{\tilde{g}} + \vec{\bullet}{g} - \vec{\circ}{g} \tag{2.33}$$

where $\vec{\tilde{g}}$ is linearized with respect to velocity, $\vec{\bullet}{g}$ is linearized with respect to density, and $\vec{\circ}{g}$ is determined from available values of density and velocity. To generate

an algebraic approximation to the control volume mass conservation equation, Eq. (2.10), it is necessary to evaluate the mass flowing across the control volume face in each element. These approximate expressions for the mass flows are then assembled in an appropriate manner to give the final discretized form of the continuity equation. The following subsections briefly illustrate how each of the terms in Eq. (2.33) is evaluated at the control volume face in an element, indicated by subscript 0. This discussion uses the nomenclature in Fig. 2.1.

Algebraic Approximation of $\tilde{g}_0$

The mass conserving velocity, Eq. (2.19), is used to evaluate the velocity in the $\tilde{g}_0$ term. Linear interpolation is used to evaluate the pseudo-velocity and the pressure coefficient at the control volume face, and the algebraic approximation of $\tilde{g}_0$ can be defined as follows:

$$\tilde{g}_0 = (\rho w)_0 \left(\hat{u}_0 - d_0^u \frac{p_2 - p_1}{x_2 - x_1} \right) \tag{2.34}$$

where ρ_0 is evaluated explicitly using the MAW scheme.

Algebraic Approximation of $\dot{g}_0$

To evaluate $\dot{g}_0$, the equation of state, Eq. (2.4), is used implicitly to define the mass flow rate, and the resulting expression is evaluated at a control volume face as follows:

$$\dot{g}_0 = \frac{w_0 u_0}{R T_1} p_1 \tag{2.35}$$

In the proposed CVFEM, the density is interpolated in an upwind manner, by upwinding both the temperature and pressure in this equation. The value of u_0 in Eq. (2.35) is the linearly interpolated mass conserving velocity at the control volume face.

Algebraic Approximation of $\mathring{g}_0$

The remaining term to be approximated in Eq. (2.33) is $\mathring{g}_0$, which is evaluated with available densities and velocities:

$$\mathring{g}_0 = \rho_0 \, w_0 \, u_0 \tag{2.36}$$

where ρ_0 and u_0 are interpolated linearly.

Complete Algebraic Approximation of the Linearized Mass Flow

The complete form of the algebraic approximation of the mass flowing across a control volume face is assembled by adding Eqs. (2.34), (2.35) and (2.36). The resulting expression can be written in terms of the nodal pressures:

$$g_0 = E_1 \, p_1 + E_2 \, p_2 + B_0 \tag{2.37}$$

where the complete derivation of E_1, E_2 and B_0 is included in Appendix B.

Final Form of the Discretized Continuity Equation

Expressions similar to Eq. (2.37) can be derived for the control volume faces in the two elements which make contributions to the control volume for node i. When these expressions are added appropriately, along with any boundary contributions, the discretized form of the integral mass conservation statement for a control volume is completed. The resulting equation can be cast in the following form:

$$a_i^p \, p_i = \sum_n a_n^p \, p_n + b_i^p \tag{2.38}$$

where the summation is over the two nodes neighbouring node i in Fig. 2.1. The assembly of Eq. (2.38) is demonstrated in Appendix C.

2.6.4 Boundary Conditions

During the discussion of the discretized forms of the governing equations, mention was made of the addition of applicable boundary contributions. If a node is within the calculation domain, no boundary contributions are required, and the equation as derived from the element contributions alone is complete. For the nodes on inflow and outflow boundaries of a quasi-one-dimensional domain, the integrated flux out of the domain, across the domain boundary, must be calculated and added to the discretized equation. The following subsections describe the evaluation of this integrated flux, and the implementation of applicable boundary conditions.

Specified Value Boundary

The specified value boundary condition is very easy to apply. When the value of a dependent scalar at node i, ϕ_i, is to be given a specified value, ϕ_{spec}, the discretized equation for node i is written in the following trivial form:

$$\phi_i = \phi_{spec} \tag{2.39}$$

This equation is implemented in the context of the discretized equations by setting all calculated coefficients equal to zero, and then redefining:

$$a_i^{\phi} = 1 \quad ; \quad b_i^{\phi} = \phi_{spec} \tag{2.40}$$

This procedure is used to overwrite coefficients in the discretized momentum, energy and continuity equations to specify boundary values of u, T, and p, respectively.

Inflow and Outflow Boundaries

At inflow and outflow boundaries, if the value of ϕ is not specified, the gradient of ϕ is set equal to zero at the boundary:

$$\frac{d\phi}{dx} = 0 \tag{2.41}$$

This equation effectively sets the diffusion transport equal to zero at the boundary. A convective flux will exist across inflow and outflow boundaries, however, and this flux must be added appropriately to the discretized equations to complete their assembly. In this quasi-one-dimensional formulation the nodal value of ϕ is assumed to prevail over the area at that node, therefore, the specification of inflow and outflow boundaries is quite simple.

To complete the assembly of the discretized momentum and energy equations at inflow and outflow boundaries, the flux across the boundary has to be incorporated into these equations. The integrated flux of ϕ out of the control volume across a boundary surface at node i is defined as $(\rho_i u_i w_i)\phi_i$, where u_i is directed out of the calculation domain, therefore, the discretized equation can be completed by adding $(\rho_i\, u_i\, w_i)$ to a_i^{ϕ}. At inflow boundaries, the velocity is directed into the control volume, therefore, the mass flow into the domain is subtracted from a_i^{ϕ}.

The completion of the discretized form of the continuity equation is performed in a different manner, because of the linearization of the mass flow, Eq. (2.33). A detailed derivation is given in Appendix B. As shown in Appendix B, the mass flow out of the domain at node i can be cast in terms of the boundary pressure, p_i, and its neighbouring nodal pressure, p_{i-1}:

$$\bar{g}_i = E_i^p\, p_i + E_{i-1}^p\, p_{i-1} + F_i^p \tag{2.42}$$

where E_i^p, E_{i-1}^p and F_i^p are defined in Appendix B. To complete the discretized form of the continuity equation, the coefficients in Eq. (2.42) should be added to the coefficients in Eq. (2.38) as follows:

$$a_i^p = a_i^p + E_i^p \tag{2.43}$$

$$a_n^p = a_n^p - E_{i-1}^p \tag{2.44}$$

$$b_i^p = b_i^p - F_i^p \tag{2.45}$$

where, the index n in Eq. (2.44) is equal to $i-1$ in this case.

2.7 Solution of the Discretized Equations

The discretized form of the governing equations derived in the previous section for quasi-one-dimensional fluid flow problems constitutes a set of nonlinear algebraic equations for velocity, pressure, and temperature. The nonlinearities in the equations are handled with an iterative successive substitution procedure, in which coefficients in the nominally linear discretized equations are evaluated from available values of the required variables. The steps used in the iterative solution algorithm for the one-dimensional CVFEM are similar to those used in the two-dimensional method described in Chapter 3: they will be discussed in detail in Section 3.7. To promote convergence of the solution algorithm, the discretized equations are also under-relaxed, as described in Section 3.7.1

2.8 Conclusion

The formulation of a CVFEM valid for steady, quasi-one-dimensional viscous compressible flows has been presented in this chapter. The formulation of a two-dimensional CVFEM developed as an extension of this work is presented in Chapter 3. Some results generated by the one-dimensional CVFEM are presented in Chapter 4.

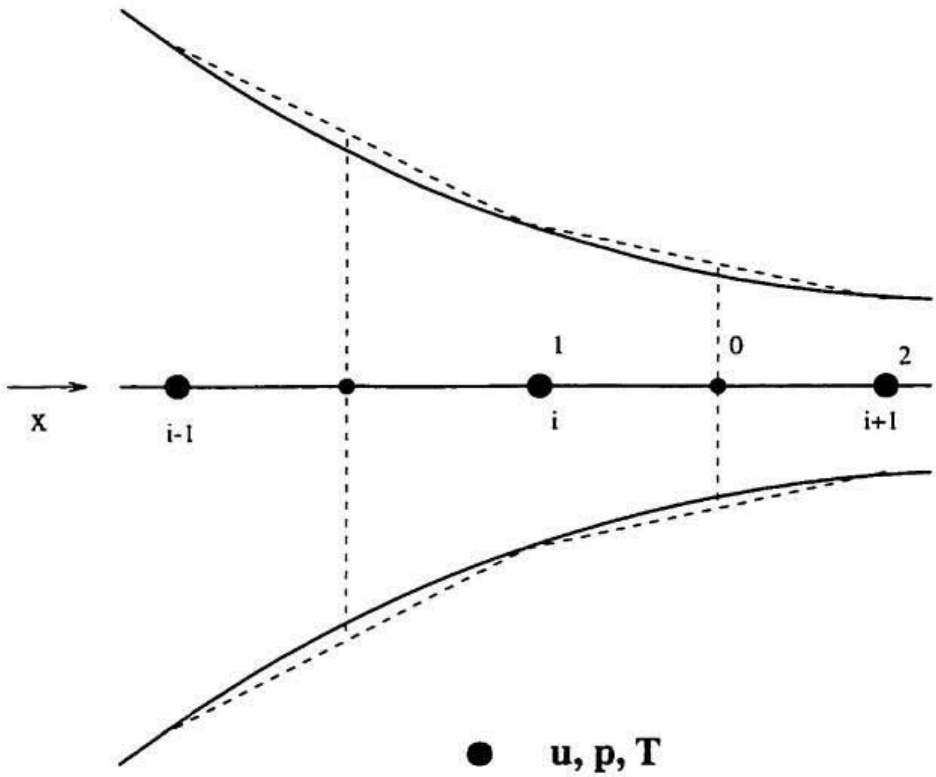

Figure 2.1: Discretization of a variable area duct by the proposed one-dimensional CVFEM.

Chapter 3

Formulation of the Proposed Two-Dimensional CVFEM

3.1 Introduction

The formulation of a CVFEM for steady, viscous, two-dimensional compressible fluid flows is presented in this chapter. The presentation is divided into sections devoted to the following topics: (1) definition of the governing equations; (2) domain discretization details; (3) derivation of control volume integral conservation equations; (4) specification of element-based interpolation functions for the dependent variables; (5) derivation of the discretized forms of the conservation equations and boundary conditions; and (6) the algorithm used to solve the discretized equations.

3.2 Governing Equations

The partial differential equations governing steady, two-dimensional, viscous compressible flow of a perfect gas are the following [25]:

Continuity:

$$\frac{\partial}{\partial x}(\rho u) + \frac{\partial}{\partial y}(\rho v) = 0 \tag{3.1}$$

x-momentum:

$$\begin{aligned}\frac{\partial}{\partial x}(\rho uu) + \frac{\partial}{\partial y}(\rho vu) &= -\frac{\partial p}{\partial x} + \frac{\partial}{\partial x}\left(\mu\frac{\partial u}{\partial x}\right) + \frac{\partial}{\partial y}\left(\mu\frac{\partial u}{\partial y}\right) + S^u \\ &+ \frac{1}{3}\frac{\partial}{\partial x}\left(\mu\frac{\partial u}{\partial x}\right) + \frac{\partial}{\partial y}\left(\mu\frac{\partial v}{\partial x}\right) - \frac{2}{3}\frac{\partial}{\partial x}\left(\mu\frac{\partial v}{\partial y}\right)\end{aligned} \tag{3.2}$$

y-momentum:

$$\begin{aligned}\frac{\partial}{\partial x}(\rho uv) + \frac{\partial}{\partial y}(\rho vv) &= -\frac{\partial p}{\partial y} + \frac{\partial}{\partial x}\left(\mu\frac{\partial v}{\partial x}\right) + \frac{\partial}{\partial y}\left(\mu\frac{\partial v}{\partial y}\right) + S^v \\ &+ \frac{1}{3}\frac{\partial}{\partial y}\left(\mu\frac{\partial v}{\partial y}\right) + \frac{\partial}{\partial x}\left(\mu\frac{\partial u}{\partial y}\right) - \frac{2}{3}\frac{\partial}{\partial y}\left(\mu\frac{\partial u}{\partial x}\right)\end{aligned} \tag{3.3}$$

Energy:

$$\begin{aligned}\frac{\partial}{\partial x}(\rho uT) + \frac{\partial}{\partial y}(\rho vT) &= \frac{\partial}{\partial x}\left(\frac{k}{c_p}\frac{\partial T}{\partial x}\right) + \frac{\partial}{\partial y}\left(\frac{k}{c_p}\frac{\partial T}{\partial y}\right) + S^T \\ &+ \frac{1}{c_p}\left(u\frac{\partial p}{\partial x} + v\frac{\partial p}{\partial y}\right) + \frac{1}{c_p}\Phi\end{aligned} \tag{3.4}$$

State:

$$\rho = \frac{p}{RT} \tag{3.5}$$

where u and v are the velocity components in the x and y directions, respectively, p is the pressure, ρ is the density, μ is the dynamic viscosity, T is the absolute temperature, k is the thermal conductivity, c_p is the specific heat at constant pressure, Φ is the viscous dissipation term, and S^u, S^v, and S^T are the volumetric source, or generation, terms for the appropriate equation. The proposed CVFEM is formulated to account for variable fluid properties, but c_p was assumed constant to keep the energy equation relatively uncomplicated.

These partial differential equations may be cast in the following conservative forms [9]:

$$\vec{\nabla}\cdot\vec{J} = S \tag{3.6}$$

$$\vec{\nabla}\cdot\vec{g} = 0 \tag{3.7}$$

where, $\vec{J}$ is the combined convection-diffusion flux vector, S is a source term, and $\vec{g}$ is the mass flux vector $\rho\vec{v}$. Equation (3.6) represents the x-momentum equation when:

$$\vec{J} = \rho\vec{v}u - \mu\vec{\nabla}u \tag{3.8}$$

$$S = S^u - \frac{\partial p}{\partial x} + \frac{1}{3}\frac{\partial}{\partial x}\left(\mu\frac{\partial u}{\partial x}\right) + \frac{\partial}{\partial y}\left(\mu\frac{\partial v}{\partial x}\right) - \frac{2}{3}\frac{\partial}{\partial x}\left(\mu\frac{\partial v}{\partial y}\right) \tag{3.9}$$

the y-momentum equation when:

$$\vec{J} = \rho\vec{v}v - \mu\vec{\nabla}v \tag{3.10}$$

$$S = S^v - \frac{\partial p}{\partial y} + \frac{1}{3}\frac{\partial}{\partial y}\left(\mu\frac{\partial v}{\partial y}\right) + \frac{\partial}{\partial x}\left(\mu\frac{\partial u}{\partial y}\right) - \frac{2}{3}\frac{\partial}{\partial y}\left(\mu\frac{\partial u}{\partial x}\right) \tag{3.11}$$

and the energy equation when:

$$\vec{J} = \rho\vec{v}T - \frac{k}{c_p}\vec{\nabla}T \tag{3.12}$$

$$S = \frac{S^T}{c_p} + \frac{1}{c_p}\left(u\frac{\partial p}{\partial x} + v\frac{\partial p}{\partial y}\right) + \frac{1}{c_p}\Phi \tag{3.13}$$

where

$$\Phi = \mu\left[2\left(\frac{\partial u}{\partial x}\right)^2 + 2\left(\frac{\partial v}{\partial y}\right)^2 + \left(\frac{\partial v}{\partial x} + \frac{\partial u}{\partial y}\right)^2 - \frac{2}{3}\left(\frac{\partial u}{\partial x} + \frac{\partial v}{\partial y}\right)^2\right] \tag{3.14}$$

Applying the appropriate conservation principle to a control volume V, which is fixed in space, integral forms of Eqs. (3.6) and (3.7) can be obtained:

$$\int_{\partial V} \vec{J}\cdot\vec{n}\,ds = \int_V S\,dV \tag{3.15}$$

$$\int_{\partial V} \vec{g}\cdot\vec{n}\,ds = 0 \tag{3.16}$$

where ∂V is the surface of the control volume, and $\vec{n}$ is the unit outward vector normal to the differential area ds.

3.3 Domain Discretization

The proposed equal-order CVFEM uses three-node triangular elements, and all dependent variables are stored at all of the nodes in the domain. The domain is discretized with a line-by-line structured mesh, and triangles are constructed by drawing a diagonal in each of the quadrilaterals formed by the intersection of the grid lines resulting from this domain discretization. The discretization of a representative irregularly shaped calculation domain is illustrated in Fig. 3.1. An advantage of using triangular elements is that they do not require isoparametric transformations, which are needed by general quadrilateral elements.

Once the calculation domain is discretized with the triangular elements, polygonal control volumes are constructed around each node in the calculation domain, by joining the centroid of each element with the midpoints on the corresponding sides. An irregularly shaped calculation domain discretized by triangular elements is shown in Fig. 3.1a; and the polygonal control volumes are shown by dashed lines in Fig. 3.1b. These polygonal control volumes have the following characteristics: (1) they do not overlap; (2) collectively they fill the entire calculation domain; (3) their boundaries do not involve interelement edges; and (4) they can be used with any triangulation. These characteristics facilitate the formulation of a CVFEM that possesses the conservative property [14].

As stated previously, the discretization scheme employed arranges the nodes in a line-by-line pattern. Such an arrangement of the nodes greatly facilitates the assembly of the coefficients in the discretized equations, and permits solution of these equations with iterative line-by-line solvers.

3.4 Integral Conservation Equations for a Control Volume

Using the control volumes defined in the previous section, the integral conservation equations, Eqs. (3.15) and (3.16), can be specified for a control volume as follows. With reference to the polygonal control volume associated with a typical node 1 within the calculation domain, either an internal node as in Fig. 3.2a, or a boundary node as in Fig. 3.2b, Eqs. (3.15) and (3.16) can be cast in the following forms:

$$\left[\int_o^{M_2} \vec{J}\cdot\vec{n}_2\,ds - \int_o^{M_3} \vec{J}\cdot\vec{n}_3\,ds - \int_V S\,dV\right] \tag{3.17}$$

$+$ [similar contributions from other elements associated with node 1]

$+$ [boundary contributions, if applicable] $= 0$

$$\left[\int_o^{M_2} \vec{g}\cdot\vec{n}_2\,ds - \int_o^{M_3} \vec{g}\cdot\vec{n}_3\,ds\right] \tag{3.18}$$

$+$ [similar contributions from other elements associated with node 1]

$+$ [boundary contributions, if applicable] $= 0$

where M_2 and M_3 are midpoints on the sides of the element, and O is the centroid of the element. The control volumes in this two-dimensional formulation are assumed to be of unit depth, therefore, the surface and volume integrals in Eqs. (3.17) and (3.18) reduce to line and area integrals, respectively. The forms of the conservation equations expressed by Eqs. (3.17) and (3.18) emphasize that they may be assembled in an element-by-element manner.

3.5 Interpolation Functions

The interpolation functions for the dependent variables and fluid properties that appear in the integral conservation equations, Eqs. (3.17) and (3.18), are described

in this section.

3.5.1 Interpolation of μ, k, c_p, and S

Values of μ, k and c_p, are supplied at the centroid of each element and these centroidal values are assumed to prevail over the corresponding element. The source terms, S^u, S^v and S^T in the x-, y-momentum and energy equations, respectively, are linearized using Taylor's expansion [14], if required, and expressed as follows:

$$S^u = S_c^u + S_p^u u \tag{3.19}$$

$$S^v = S_c^v + S_p^v v \tag{3.20}$$

$$S^T = S_c^T + S_p^T T \tag{3.21}$$

where S_c represents terms independent of the superscripted variable, and S_p provides for a linear dependence of S on the corresponding variable. The values of S_c and S_p are evaluated at the centroid of each element, and these values are assumed to prevail within the element.

3.5.2 Interpolation of Pressure

Within an element, the pressure is interpolated linearly:

$$p = a_p x + b_p y + c_p \tag{3.22}$$

where the coefficients a_p, b_p, and c_p in Eq. (3.22) are defined by the nodal values of pressure, and the corresponding nodal x,y co-ordinates. The derivation of these coefficients is presented in Appendix D. Using the coefficient definitions in Appendix D, the pressure gradients can be expressed as follows:

$$\frac{\partial p}{\partial x} = a_p = \sum_{i=1}^{3} D_i^x p_i \tag{3.23}$$

$$\frac{\partial p}{\partial y} = b_p = \sum_{i=1}^{3} D_i^y p_i \tag{3.24}$$

3.5.3 Interpolation of Velocities

Interpolation of a Convected Velocity

When velocity is treated as a convected scalar, for example in the convection terms in the momentum equation, it is interpolated using the MAss Weighted (MAW) scheme.

On each of the three control volume faces (denoted by the index k) of Fig. 3.3, a value of the convected scalar that is assumed to prevail over that face can be defined. This is the integration point value, and it is given the symbol ϕ_k^c for the general scalar dependent variable, ϕ. The MAW scheme uses the mass flow rates ($\dot{m}_k$) across each control volume surface to define integration point values, where,

$$\dot{m}_k = \int_k \rho \vec{u} \cdot \vec{n}_k \, ds \tag{3.25}$$

Thus the mass flow rate across a particular control volume surface within an element is taken as positive when the velocity vector at the integration point is in the same direction as the assumed normal to the surface.

The following rules can be used to determine ϕ_k^c for the element shown in Fig. 3.3.

Control volume surface 1

$$\begin{aligned} &\text{If } \dot{m}_1 > 0 \quad \phi_1^c = f\phi_2^c + (1-f)\Phi_3 \\ &\text{where} \quad f = min\left[max\left(\frac{\dot{m}_2}{\dot{m}_1}, 0\right), 1\right] \end{aligned} \tag{3.26}$$

$$\begin{aligned} &\text{If } \dot{m}_1 < 0 \quad \phi_1^c = f\phi_3^c + (1-f)\Phi_2 \\ &\text{where} \quad f = min\left[max\left(\frac{\dot{m}_3}{\dot{m}_1}, 0\right), 1\right] \end{aligned} \tag{3.27}$$

Control volume surface 2

$$\text{If } \dot{m}_2 > 0 \quad \phi_2^c = f\phi_3^c + (1-f)\Phi_1$$
$$\text{where} \quad f = min\left[max\left(\frac{\dot{m}_3}{\dot{m}_2}, 0\right), 1\right] \tag{3.28}$$

$$\text{If } \dot{m}_2 < 0 \quad \phi_2^c = f\phi_1^c + (1-f)\Phi_3$$
$$\text{where} \quad f = min\left[max\left(\frac{\dot{m}_1}{\dot{m}_2}, 0\right), 1\right] \tag{3.29}$$

Control volume surface 3

$$\text{If } \dot{m}_3 > 0 \quad \phi_3^c = f\phi_1^c + (1-f)\Phi_2$$
$$\text{where} \quad f = min\left[max\left(\frac{\dot{m}_1}{\dot{m}_3}, 0\right), 1\right] \tag{3.30}$$

$$\text{If } \dot{m}_3 < 0 \quad \phi_3^c = f\phi_2^c + (1-f)\Phi_1$$
$$\text{where} \quad f = min\left[max\left(\frac{\dot{m}_2}{\dot{m}_3}, 0\right), 1\right] \tag{3.31}$$

In these equations, Φ is a nodal value, and ϕ is an integration point value.

As shown in Appendix D, Eqs. (3.26) to (3.31) result in a matrix equation for ϕ_k^c, which can be simplified to the following equation:

$$\phi_k^c = \sum_{j=1}^{3} CC_j^k \Phi_j \tag{3.32}$$

where, the CC_j^k are coefficients calculated from the nodal values of ϕ, and mass ratio, f.

The interpolation of a convected velocity on a control volume face k can therefore be written as follows.

$$u_k = \sum_{j=1}^{3} CC_j^k u_j \tag{3.33}$$

Interpolation of a Mass Conserving Velocity

The mass conserving velocities, u^m and v^m, are interpolated by assuming a linear variation of the corresponding pseudo-velocity, $\hat{u}$ or $\hat{v}$, and pressure coefficient, d^u or d^v, used in conjunction with the local elemental pressure gradient. Consequently, the expression of mass conserving velocity can be written at each node within an element:

$$u_i^m = \hat{u}_i - d_i^u \left(\frac{\partial p}{\partial x}\right)_e \tag{3.34}$$

$$v_i^m = \hat{v}_i - d_i^v \left(\frac{\partial p}{\partial y}\right)_e \tag{3.35}$$

The subscript, e, on the pressure gradient indicates that the elemental pressure gradient, and not the average pressure gradient over the control volume surrounding the node in question, is being used. The evaluation of $\hat{u}_i$, $\hat{v}_i$, d_i^u and d_i^v will be described in Section 3.6.3.

The pseudo-velocities, $\hat{u}_i$ and $\hat{v}_i$, and the pressure coefficients, d_i^u and d_i^v, are known at the nodes. In order to determine the values of these quantities at the integration points on the control volume faces within the elements, a linear interpolation of the nodal values, is used:

$$\hat{u} = a_{\hat{u}}\, x + b_{\hat{u}}\, y + c_{\hat{u}} \tag{3.36}$$

$$d^u = a_d^u\, x + b_d^u\, y + c_d^u \tag{3.37}$$

$$\hat{v} = a_{\hat{v}}\, x + b_{\hat{v}}\, y + c_{\hat{v}} \tag{3.38}$$

$$d^v = a_d^v\, x + b_d^v\, y + c_d^v \tag{3.39}$$

Interpolation of a Diffused Velocity

When velocity is treated as a diffused scalar, for example in the viscous terms of the momentum equation, it is interpolated linearly within an element.

$$u = a^u x + b^u y + c^u \tag{3.40}$$

$$v = a^v x + b^v y + c^v \tag{3.41}$$

where the interpolation coefficients are defined by the nodal velocities, and the geometry of the element, as discussed in Appendix D

3.5.4 Interpolation of Temperature

The temperature, T, is interpolated in a similar manner to the velocity. When temperature is a convected scalar, the MAW scheme is used. When temperature appears in a diffusion term or a source term, it is interpolated linearly within an element.

3.5.5 Interpolation of Density

In the proposed CVFEM, density is interpolated by the MAW scheme, therefore, the following expression can be written for density:

$$\rho_k = \sum_{j=1}^{3} CC_j^k \rho_j \tag{3.42}$$

where the nodal density is evaluated using the equation of state for an ideal gas, and the CC_j^k terms are calculated from available nodal values of ρ and mass ratio f.

3.6 Derivation of the Discretized Equations

To obtain algebraic approximations of the integral conservation equations for a control volume, Eqs. (3.15) and (3.16), approximations of the element contributions

to Eqs. (3.17) and (3.18) are derived and assembled in an appropriate manner. Algebraic approximations of the boundary contributions are then derived, if applicable, and added to the element contributions. These approximations and assembly procedures are discussed in this section.

3.6.1 x-Momentum Equation

Integration of the convection-diffusion flux across a control volume face

Within each element, the combined convection-diffusion transport of x-momentum, Eq. (3.8), is evaluated at the control volume face. With reference to Fig. 3.3, for the subcontrol volume around node 3, the combined convection-diffusion transport term should be evaluated on the control volume faces 1 and 2 (indicated in Fig. 3.3 by $\vec{n}_1$ and $\vec{n}_2$).

The integrated flux of x-momentum across a control volume face k is expressed in the following manner:

$$\int_o^{M_k} \vec{J} \cdot \vec{n}_k \, ds = \int_o^{M_k} \rho \vec{v} u \cdot \vec{n}_k \, ds - \int_o^{M_k} \mu \vec{\nabla} u \cdot \vec{n}_k \, ds \tag{3.43}$$

The MAW interpolation scheme is used to interpolate u in the convection term, and linear interpolation is used to evaluate the gradient of u in the diffusion term. Using Simpson's Rule, the integral in Eq. (3.43) can be rewritten in terms of the nodal velocities, as follows:

$$\int_o^{M_k} \vec{J} \cdot \vec{n}_k \, ds = \sum_{j=1}^{3} C_j^k \, u_j \tag{3.44}$$

where a complete derivation of C_j^k is presented in Appendix E.

The element contribution to the volume integration of the source term for the control volume around node 3 is given by:

$$\int_{V_e^3} S \, dV = S_c^u V_e^3 + S_p^u V_e^3 u_3 - V_e^3 \sum_{i=1}^{3} D_i^x p_i + S_{vis}^u \tag{3.45}$$

where V_e^3 is the volume of the subcontrol volume, and S_{vis}^u represents the integral of extra viscous terms over the subcontrol volume, V_e^3, in the x-momentum equation.

Final form of the discretized equation for x-momentum

Expressions similar to Eq. (3.44) can be derived for the integrated convection-diffusion flux across each of the control volume faces in an element. When these expressions are added appropriately with similar expressions from other elements which make a contribution to the control volume surrounding a node i, along with the applicable boundary contributions and integrated source terms, Eq. (3.45), the algebraic approximation of the integral conservation equation for a control volume, Eq. (3.17), is obtained. The resulting discretized x-momentum equation can be cast in the following form:

$$a_i^u u_i = \sum_n a_n^u u_n + b_i^u p_i + \sum_n b_n^u p_n + e_i^u \tag{3.46}$$

where the summation is taken over all the nodes neighbouring node i. The complete assembly of Eq. (3.46) is discussed in Appendix F, with reference to Figs. 3.4 and 3.5. The maximum number of neighbour nodes will be the eight nodes surrounding node i, j in Fig. 3.5.

Final form of the discretized equation for y-momentum

As described in Appendix F, the assembly of the discretized y-momentum equation is performed in the same manner as for the discretized x-momentum equation, Eq. (3.46). The final form of the discretized y-momentum equation can be written as follows:

$$a_i^v v_i = \sum_n a_n^v v_n + b_i^v p_i + \sum_n b_n^v p_n + e_i^v \tag{3.47}$$

The assembly of Eq. (3.47) is presented in Appendix F.

3.6.2 Energy Equation

The procedures used in the discretization of the x-momentum equations are also used to derive the algebraic approximation of the energy equation. The derivations are altered by replacing the viscosity, μ, with k/c_p, and the source term with the appropriate source term for the energy equation, Eq. (3.13).

The integral of the combined convection-diffusion flux across a control face can be written for the energy equation as follows:

$$\int_o^{M_k} \vec{J} \cdot \vec{n}_k \, ds = \sum_{j=1}^{3} C_j^k T_j \tag{3.48}$$

The integration of the source term in the energy equation gives:

$$\int_V S dV = \frac{V_e^1}{c_p} \left(S_c^T + S_p^T T_1 + u_{av} \sum_{i=1}^{3} D_i^x p_i + v_{av} \sum_{i=1}^{3} D_i^y p_i + \Phi_c \right) \tag{3.49}$$

A complete derivation of Eqs. (3.48) and (3.49) is given in Appendix E.

Expressions similar to Eq. (3.48) are derived for all flux integrals that contribute to the control volume conservation equation for a node i. These contributions are added, along with any boundary contributions and the volume integration of the appropriate source term, to obtain an algebraic approximation of the energy equation. This discretized energy equation may be written in the following form:

$$a_i^T T_i = \sum_n a_n^T T_n + e_i^T \tag{3.50}$$

The assembly procedure for Eq. (3.50) is described in Appendix F.

3.6.3 Continuity Equation

As discussed in Chapter 2, the mass flux, $\vec{g}$, is linearized with respect to density, ρ, and velocity, $\vec{v}$:

$$\vec{g} = \vec{\tilde{g}} + \vec{\dot{g}} - \vec{\bar{g}} \tag{3.51}$$

where $\tilde{\vec{g}}$ is linearized with respect to velocity, $\dot{\vec{g}}$ is linearized with respect to density and $\mathring{\vec{g}}$ is determined from available values of density and velocity. To provide an algebraic approximation of the integral form of the control volume continuity equation, Eq. (3.16), it is necessary to integrate the mass flux across each of the control volume faces in an element. These integrated mass fluxes are then added appropriately to obtain the element contribution to the control volume integral mass conservation equation. The integral of the mass flux across a control volume face k may be expressed as:

$$\left(\begin{array}{l} \text{Integrated mass flux across} \\ \text{control volume face k} \end{array} \right) = \int_o^{M_k} \vec{g} \cdot \vec{n}_k \, ds$$

$$= \int_o^{M_k} \tilde{\vec{g}} \cdot \vec{n}_k \, ds + \int_o^{M_k} \dot{\vec{g}} \cdot \vec{n}_k \, ds - \int_o^{M_k} \mathring{\vec{g}} \cdot \vec{n}_k \, ds \tag{3.52}$$

Similar to the method presented in Section 2.6.3, the approach taken here is to use particular forms of the discretized momentum equations, Eqs. (3.46) and (3.47), to define four new nodal fields, which will be used in the prescription of suitable interpolation functions for the mass conserving velocities. Equations (3.46) and (3.47) can be rearranged as follows:

$$u_i = \frac{\sum_n a_n^u u_n + e_i^u}{a_i^u} - \frac{\overline{(\partial p/\partial x_i)} \Delta V}{a_i^u} \tag{3.53}$$

$$v_i = \frac{\sum_n a_n^v v_n + e_i^v}{a_i^v} - \frac{\overline{(\partial p/\partial y_i)} \Delta V}{a_i^v} \tag{3.54}$$

In these two expressions, $\overline{(\partial p/\partial x_i)}$ and $\overline{(\partial p/\partial y_i)}$ are the average of the pressure gradient acting over the control volume, of volume ΔV, for node i. Defining the pseudo-velocities, $\hat{u}_i$ and $\hat{v}_i$, as:

$$\hat{u}_i = \frac{\sum a_n^u u_n + e_i^u}{a_i^u} \tag{3.55}$$

$$\hat{v}_i = \frac{\sum a_n^v v_n + e_i^v}{a_i^v} \tag{3.56}$$

and the pressure coefficients d_i^u and d_i^v:

$$d_i^u = \frac{\Delta V}{a_i^u} \tag{3.57}$$

$$d_i^v = \frac{\Delta V}{a_i^v} \tag{3.58}$$

Eqs. (3.53) and (3.54) can be rewritten as:

$$u_i = \hat{u}_i - d_i^u \overline{\frac{\partial p}{\partial x_i}} \tag{3.59}$$

$$v_i = \hat{v}_i - d_i^v \overline{\frac{\partial p}{\partial y_i}} \tag{3.60}$$

Similar expressions can be written for each node in the computational domain. It should be noted that the formulae used in the following subsections for the mass conserving velocities are Eqs. (3.34) and (3.35), where the elemental pressure gradients are used instead of average control volume pressure gradients. This is to facilitate the inclusion of the nodal pressures in the discretized form of the mass flux. If the control volume averaged pressure gradient was employed, the number of pressure nodes included in the mass flux would become unwieldy.

A complete derivation of the three integrals in Eq. (3.52) is presented in Appendix E. The final result of this integration is the following expression for the integration of the mass flux across a control volume face k:

$$\int_o^{M_k} \bar{g} \cdot \vec{n}_k ds = \sum_{j=1}^{3} E_j^k p_j + F^k \tag{3.61}$$

where the coefficients E_j^k and F^k are defined in Appendix E.

Expressions similar to Eq. (3.61) can be derived for the mass flow rate across all three control volume faces in an element. When these expressions are added appropriately with similar expressions from other elements which make a contribution to

the control volume surrounding a node i, along with the applicable boundary contributions, the algebraic approximation of the integral mass conservation equation for a control volume is formed. The resulting equation can be cast in the following form:

$$a_i^p p_i = \sum_n a_n^p p_n + e_i^p \tag{3.62}$$

where the summation is taken over all the nodes neighbouring node i. The complete assembly of Eq. (3.62), and the neighbouring nodes that are involved in the equation are discussed in Appendix F.

3.6.4 Boundary Conditions

Introduction

Thus far in this section, mention has been made of applicable boundary contributions to be added to the discretized equations. If the node under consideration is located within the calculation domain, no boundary contributions are present, and the specification of the discretized equations is complete. For nodes located on boundaries, however, the discretized equations are incomplete unless the flux across the boundary is included. For example, in Fig. 3.2b, the flux across the side of element 123, from 1 to M_3, must be specified to complete the contribution of element 123 to the control volume surrounding node 1. The transport of a scalar dependent variable, ϕ, out of the control volume from 1 to M_3 can be specified as:

$$\left(\begin{array}{l} \text{Integrated flux of } \phi \text{ out of} \\ \text{control volume side 1 to } M_3 \end{array} \right) = \int_1^{M_3} \vec{J} \cdot \vec{n}\, ds \tag{3.63}$$

where $\vec{n}$ is the outward unit normal vector to the element side ds. The equations in this subsection are written for a general scalar dependent variable, ϕ, however, they may be interpreted as equations for the other dependent variables, u, v, T, and p, where indicated. The derivation of algebraic approximations of the appropriate

boundary conditions and the incorporation of these boundary contributions into the discretized equations are described in the following subsections.

Specified value boundary

The specified value boundary condition is the simplest to apply; when the value of ϕ_i is to be given a specific value, ϕ_{spec}, the discretized equation for node i is written in the following trivial form:

$$\phi_i = \phi_{spec} \tag{3.64}$$

This equation can be obtained by suitably overwriting the x-,y-momentum, energy, or continuity equations, to specify u, v, T, or p, respectively. It is implemented by setting all calculated coefficients in the applicable discretized equation equal to zero, and defining:

$$a_i^{\phi} = 1 \quad ; \quad e_i^{\phi} = \phi_{spec} \tag{3.65}$$

where ϕ can be replaced by u, v, T, or p as required.

Specified flux boundary

This boundary condition is used when the flux, of the quantity of interest, across a boundary is specified. If the specified flux out of the control volume is denoted by q, then Eq. (3.63) can be written as:

$$\int_1^{M_3} \vec{J} \cdot \vec{n}\, ds = \int_1^{M_3} q\, ds \tag{3.66}$$

where, q may be a constant or a function that can be integrated in closed form. When q is available only at the nodes, then linear interpolation is used between the nodes, and the integral of Eq. (3.66) is written as:

$$\int_1^{M_3} \vec{J} \cdot \vec{n}\, ds = \int_1^{M_3} q\, ds = \Delta s_{1-M_3} (3q_1 + q_2)/4 \tag{3.67}$$

where Δs_{1-M_3} is the length of the side of the element from node 1 to position M_3, in Fig. 3.2b.

Outflow boundaries

If the dependent variable is not specified, the diffusion transport is made equal to zero at outflow boundaries by setting the dot product of the gradient of ϕ and the outward unit normal vector to the boundary, $\vec{n}$, equal to zero:

$$\vec{\nabla}\phi \cdot \vec{n} = 0 \tag{3.68}$$

This boundary condition is used to disconnect the calculation domain from external influences across outflow boundaries. There will, however, be a convective flux across outflow boundaries. This flux is integrated as follows:

$$\left(\begin{array}{l} \text{Integral of convective flux of } \phi \\ \text{across control volume side 1 to } M_3 \end{array} \right) = \int_1^{M_3} \rho \vec{u} \phi \cdot \vec{n}\, ds \tag{3.69}$$

In the proposed CVFEM, an algebraic approximation of this integral is obtained by assuming that ϕ_i prevails over the control volume for node i. The mass flow rate out of the control volume:

$$\left(\begin{array}{l} \text{Integral mass flux out of} \\ \text{control volume side 1 to } M_3 \end{array} \right) = \int_1^{M_3} \rho \vec{u} \cdot \vec{n}\, ds \tag{3.70}$$

is approximated by assuming linear interpolation for ρ, u, and v between two nodes on the boundary, such as nodes 1 and 2 in Fig. 3.2b.

To complete the specification of the momentum, energy, and general convection-diffusion equations at outflow boundaries, the integrated convection flux across the boundary has to be incorporated into the forms of the discretized equations that have been obtained from element contributions alone. This is done by adding the integrated mass flux, Eq. (3.70), to the appropriate coefficient for ϕ_i, where ϕ is replaced by u, v, or T for the appropriate equation.

The completion of the discretized continuity equation at outflow boundaries requires special treatment due to the linearization imposed on the mass flux, Eq.

(3.51). The integral of the $\overset{\circ}{\vec{g}}$ term at the boundary is evaluated using linear interpolation of available densities and velocities in Eq. (3.70). This integrated mass flux is then added to the constant term in the discretized form of the continuity equation obtained form element contributions alone. The $\overset{\bullet}{\vec{g}}$ term is integrated over the boundary, by assuming that the pressure, velocity, and temperature at node i prevail over the control volume side:

$$\int_1^{M_3} \overset{\bullet}{\vec{g}} \cdot \vec{n}\, ds = p_i \left(\frac{\vec{u}_i \cdot \vec{n}}{RT_i} \Delta s_{1-M_3} \right) \tag{3.71}$$

The term in brackets is then added to the coefficient multiplying p_i. The $\tilde{\vec{g}}$ term is integrated by assuming density and velocity at node i prevail over the control volume edge:

$$\int_1^{M_3} \tilde{\vec{g}} \cdot \vec{n}\, ds = u_i \left(\rho_i n_x \Delta s_{1-M_3} \right) + v_i \left(\rho_i n_y \Delta s_{1-M_3} \right) \tag{3.72}$$

where n_x and n_y are the x,y components of $\vec{n}$. Substituting the mass conserving velocity formulae Eqs. (3.34) and (3.35) for u_i and v_i, and writing the above equation in terms of nodal pressures:

$$\begin{aligned} \int_1^{M_3} \tilde{\vec{g}} \cdot \vec{n}\, ds &= \left(\hat{u}_i \rho_i n_x \Delta s_{1-M_3} + \hat{v}_i \rho_i n_y \Delta s_{1-M_3} \right) \\ &- \sum_{j=1}^{3} \left(d_i^u D_j^x n_x \Delta s_{1-M_3} + d_i^u D_j^x n_x \Delta s_{1-M_3} \right) p_j \end{aligned} \tag{3.73}$$

The first bracketed term is subtracted from the constant term in the discretized form of the continuity equation, and the second bracketed term is added to the appropriate coefficients multiplying p_j.

Tangency condition

Flow tangency conditions are applied to inviscid flows over a surface using the following equation:

$$\vec{u} \cdot \vec{n} = 0 \tag{3.74}$$

where $\vec{n}$ is a normal to the surface. In the proposed CVFEM, this boundary condition is imposed by specifying that one velocity component is equal to the product of the surface slope and the other velocity component: the specified value boundary condition, Eq. (3.64), is used to overwrite the coefficients in the appropriate discretized momentum equation, such that the constant term in this equation is equal to the product. The other velocity component is solved with no-flow, zero diffusion boundary conditions, thus no boundary contributions or modifications are necessary to complete the discretized equation obtained from internal element contributions. Since one velocity component is held fixed during the solution of the discretized momentum and continuity equations, the update of the fixed velocity component lags that of the calculated velocity. After solution of the discretized momentum and continuity equations, however, tangency is reimposed by reevaluating the product of the surface slope and the newly calculated velocity component.

3.6.5 Summary

The derivation of the discretized forms of the integral conservation equations for mass, momentum, and energy were presented in this section. The result is a set of nonlinear algebraic equations which are solved using the procedures discussed in the next section.

3.7 Solution of the Discretized Equations

In the proposed method, a set of nonlinear algebraic equations for velocity, pressure, and temperature are obtained as approximations of the integral conservation of momentum, mass, and energy, respectively. The nonlinearities in the equations are handled by an iterative successive substitution procedure, in which coefficients are evaluated in each iteration with best available values. The overall solution

procedure employs the following series of steps:

1. Guess the pressure field, p, velocity field, u and v, and temperature field, T.

2. Evaluate the nodal values of density using available field values of pressure and temperature in the equation of state, Eq. (3.5)

3. Determine the coefficients in the discretized momentum equations, Eqs. (3.46) and (3.47).

4. Calculate the pseudo-velocity fields for the x- and y-momentum equations using Eqs. (3.55) to (3.58). Apply the appropriate boundary conditions to $\hat{u}_i$, $\hat{v}_i$, d_i^u and d_i^v.

5. Calculate the coefficients in the discretized continuity equation, Eq. (3.61). Apply the appropriate boundary conditions, and solve the discretized continuity equation set using a tridiagonal matrix algorithm (TDMA).

6. Use the pressures calculated in step (5) to complete the discretized momentum equations, Eqs. (3.46) and (3.47).

7. Apply the required boundary conditions, if needed, under-relax the momentum equations (see Section 3.7.1), and solve the discretized forms of the x-,y-momentum equations separately using a TDMA.

8. Return to step (2) and repeat the algorithm to convergence.

3.7.1 Relaxation of the Discretized Equations

The discretized equations that are solved in the above solution algorithm are nonlinear and strongly coupled. The nonlinearities are handled by the iterative nature of the algorithm, wherein the coefficients are evaluated in each iteration with

best available estimates of the required variables. The solution algorithm does not guarantee convergence, as nonlinearities may be so strong that they may cause coefficients and the solution to oscillate or diverge. This problem is controlled in the proposed CVFEM by using the implicit under-relaxation techniques of Patankar [14].

To under-relax the x-momentum equation, Eq. (3.46), it is first written as follows:

$$u_i = \left(\sum_n a_n^u u_n + b_i^u p_i + \sum_n b_n^u p_n + e_i^u \right) / a_i^u \tag{3.75}$$

The value of u_i from a previous iteration, u_i^*, can then be added to both sides of Eq. (3.75), and the resulting equation may be rewritten as follows:

$$u_i = u_i^* + \left[\left(\sum_n a_n^u u_n + b_i^u p_i + \sum_n b_n^u p_n + e_i^u \right) / a_i^u - u_i^* \right] \tag{3.76}$$

where the new bracketed term represents the change in u_i between two successive iterations. The magnitude of this change may become so large that it could cause divergence. To control the rate of change in the solution between iterations, a relaxation term, α_u, is included in Eq. (3.76) as follows:

$$u_i = u_i^* + \alpha_u \left[\left(\sum_n a_n^u u_n + b_i^u p_i + \sum_n b_n^u p_n + e_i^u \right) / a_i^u - u_i^* \right] \tag{3.77}$$

When α_u is greater than zero, but less than one, the equation is under-relaxed, and changes in u_i between iterations are reduced, thus promoting convergence. The smaller the magnitude of α_u the smaller the corresponding changes in u_i. Equation (3.77) can be rewritten in a form similar to Eq. (3.46):

$$\frac{a_i^u}{\alpha_u} u_i = \sum_n a_n^u u_n + b_i^u p_i + \sum_n b_n^u p_n + e_i^u + (1 - \alpha_u) \frac{a_i^u}{\alpha_u} u_i^* \tag{3.78}$$

A comparison of Eq. (3.78) with Eq. (3.46), shows that the coefficient multiplying u_i has been modified, and a new explicitly evaluated term has been added to the

right hand side. When convergence is reached, $u_i = u_i^*$, and Eq. (3.78) reduces to Eq. (3.46).

A similar method is used in the proposed CVFEM to under-relax the y-momentum and energy equations, using the parameters α_v and α_T, respectively. The continuity equation is not relaxed, as this would imply mass source or sink terms in the discretized equation. The optimum values of α_u, α_v, and α_T which ensure the fastest convergence of the solution algorithm may be problem dependent, therefore, they have to be determined by testing several values in the context of the particular problem of interest.

3.8 Conclusion

This chapter has presented the formulation of a CVFEM developed for the solution of steady, two-dimensional, viscous compressible fluid flow problems. Results generated by this method in the solution of several example flow problems are presented in the next chapter, and conclusions from this work are discussed in Chapter 5

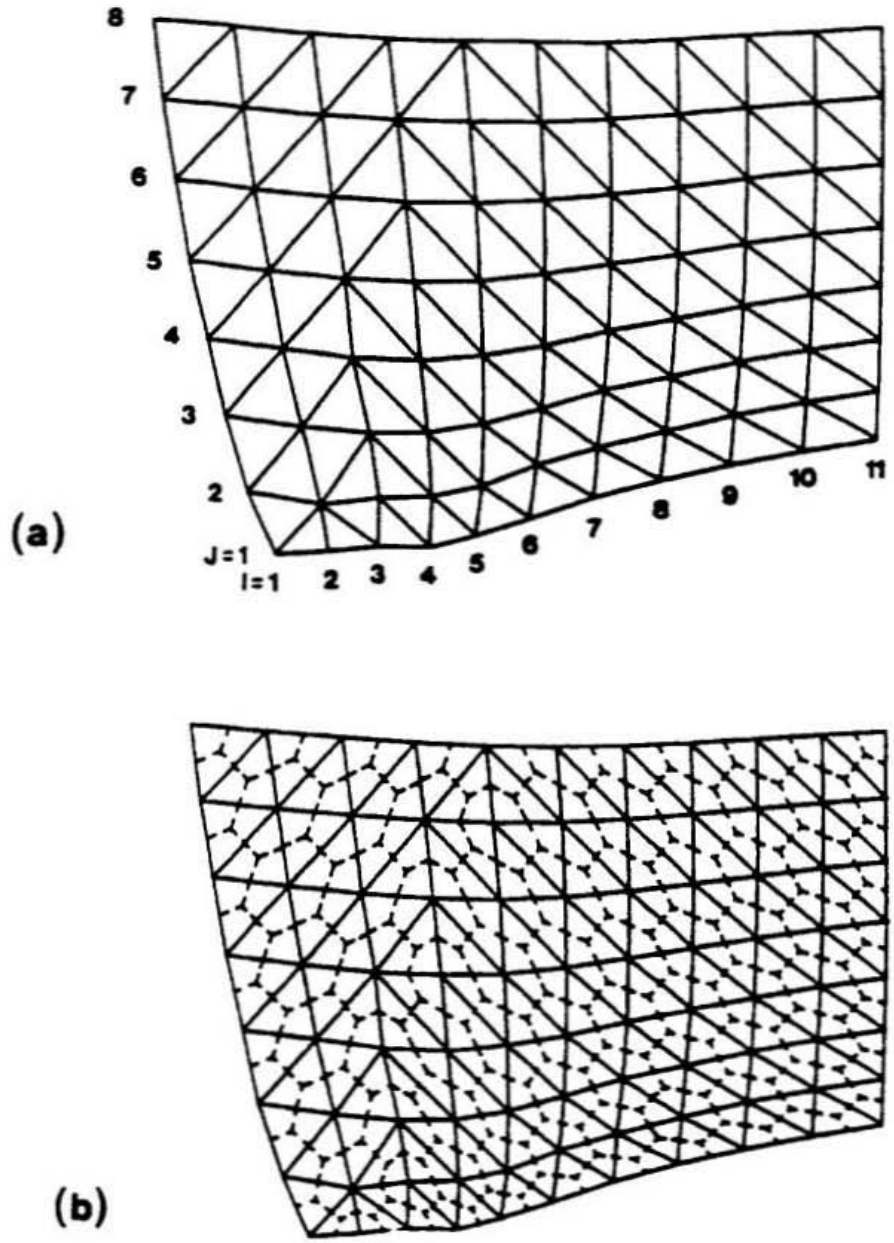

Figure 3.1: Discretization of an irregular-shaped calculation domain by the proposed two-dimensional CVFEM: (a) three-node triangular elements; and (b) polygonal control volumes.

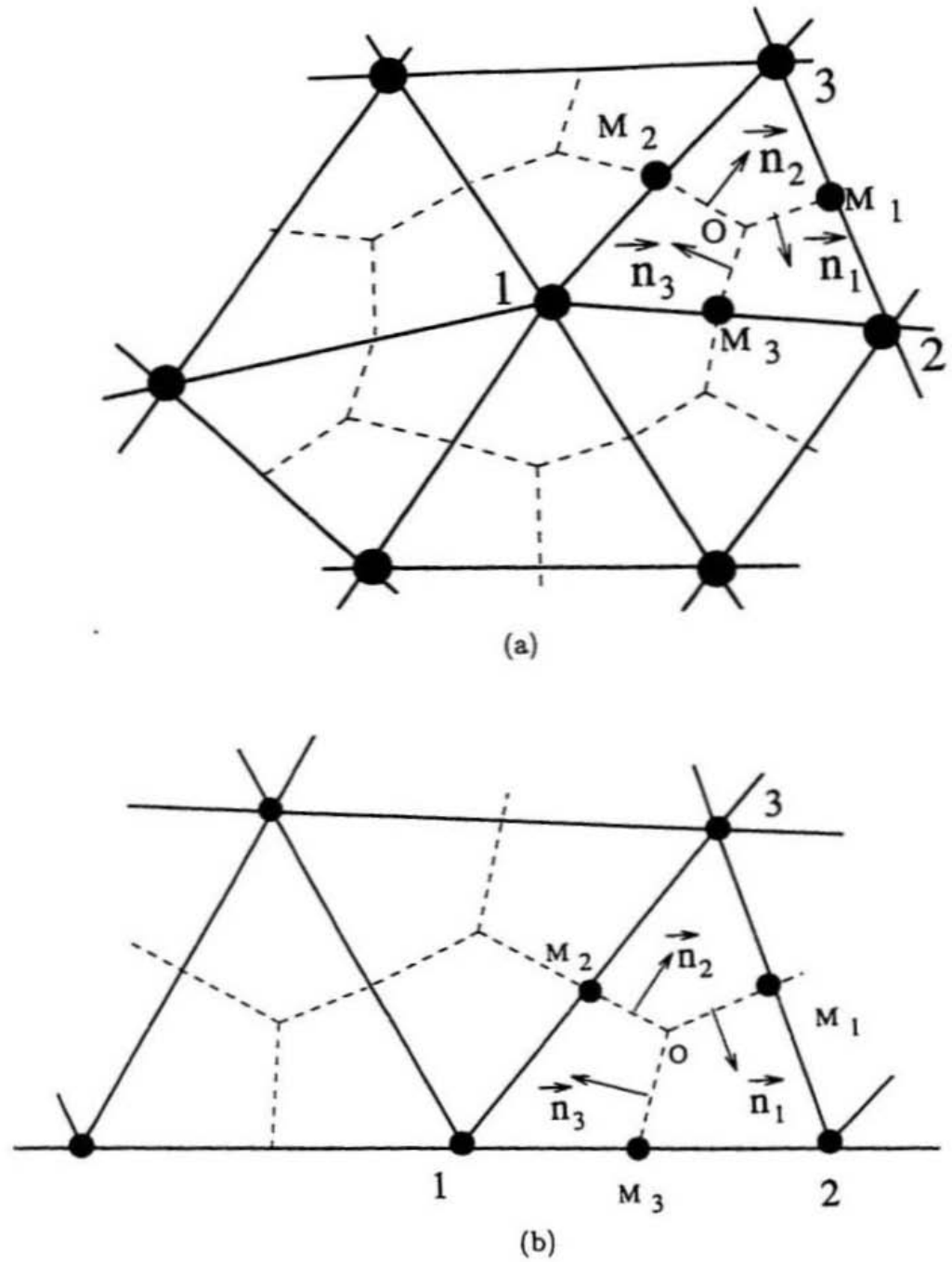

Figure 3.2: Details of the domain discretization, and related nomenclature: (a) an internal node; and (b) a boundary node.

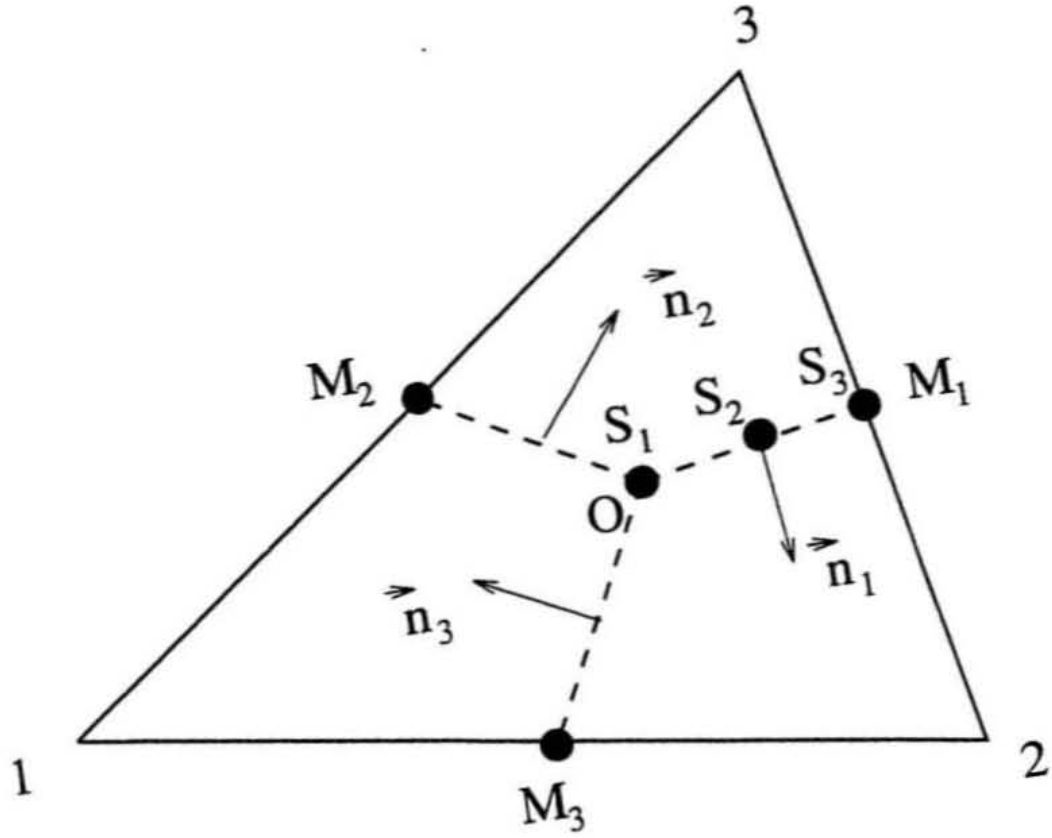

Figure 3.3: A typical three-node triangular element.

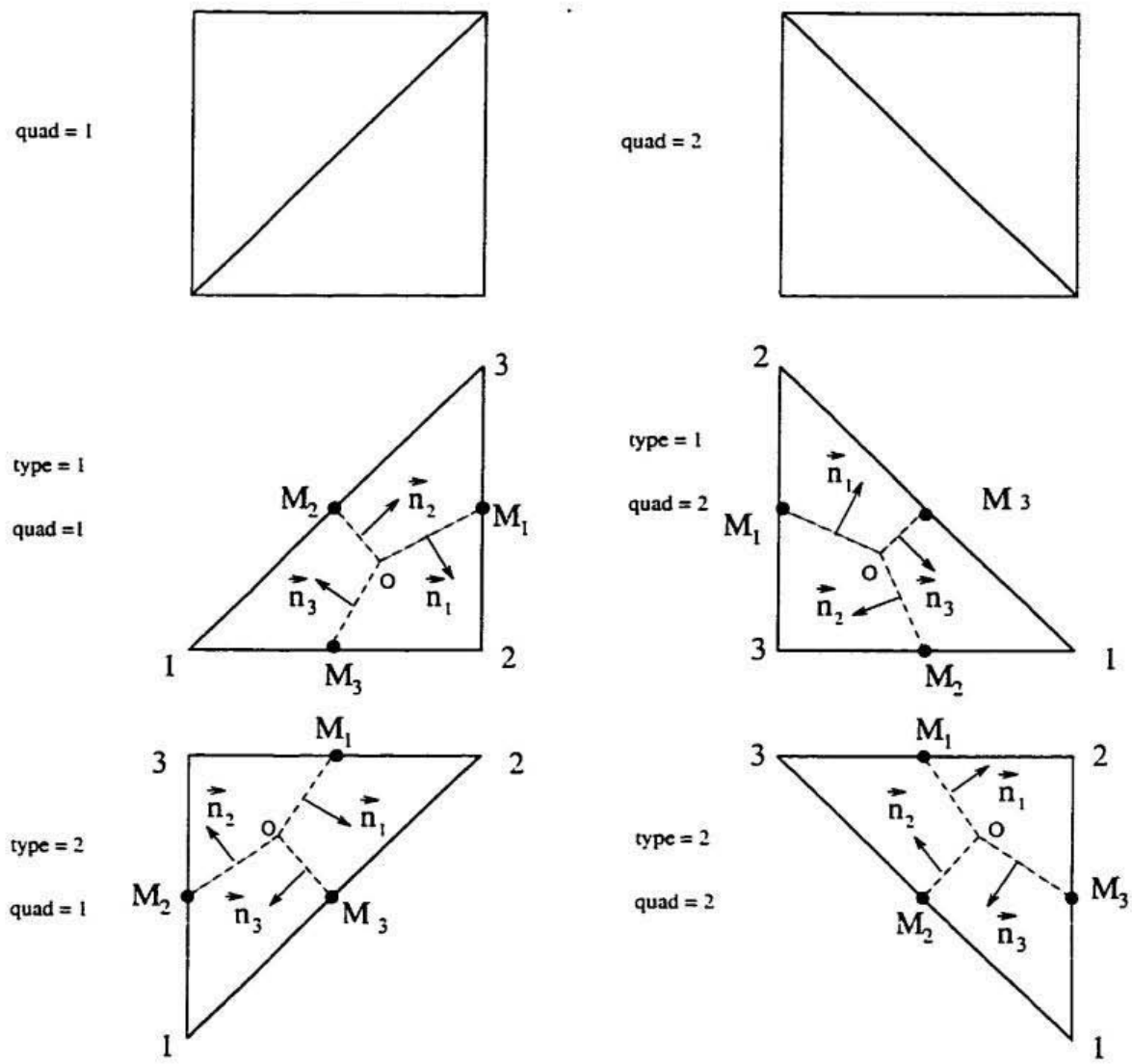

Figure 3.4: Types of elements used in the discretization equation.

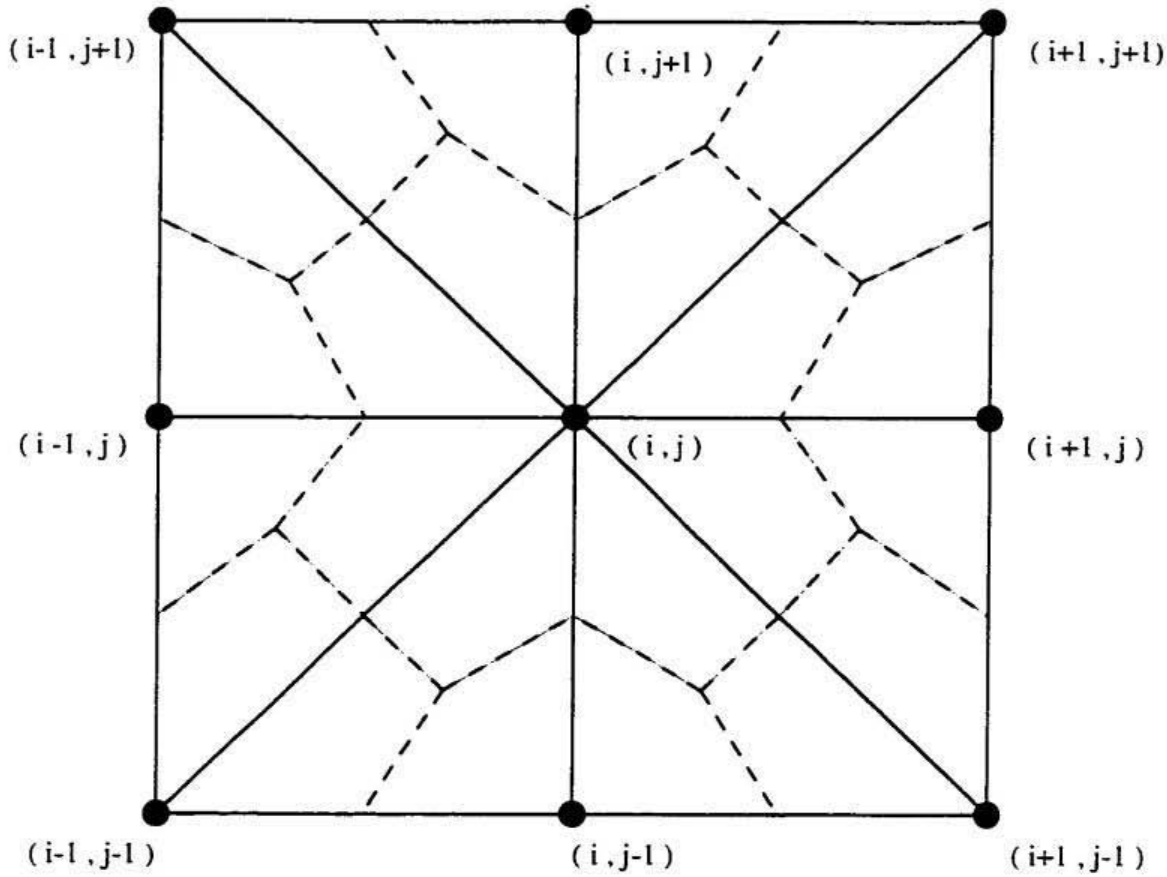

Figure 3.5: The node cluster involved in the discretization equation for a node (i,j).

Chapter 4

Results

4.1 Introduction

The main goal of this thesis is the formulation and implementation of a MAW-based CVFEM for steady, two-dimensional, viscous compressible fluid flows. During the course of this work, CVFEM's for quasi-one-dimensional and two-dimensional fluid flow problems were developed. The formulation of the one-dimensional CVFEM was presented in Chapter 2, and the two-dimensional CVFEM was described in Chapter 3. To evaluate the capabilities and limitations of these methods, they were applied to several test problems, and the results generated are presented in this chapter. The one-dimensional CVFEM was tested in the context of several steady, quasi-one-dimensional, inviscid fluid flow problems. The performance of the two-dimensional CVFEM was evaluated in the context of four inviscid and one viscous flow problems.

The remainder of this chapter is divided into two sections. In Section 4.2, the one-dimensional test problems are presented, and the CVFEM results are compared with theoretical solutions. In Section 4.3, the two-dimensional test problems are described, and the CVFEM results are compared with experimental or numerical data available in the literature.

4.2 Quasi-One-Dimensional Test Problems

4.2.1 Introduction

The one-dimensional CVFEM was tested in the context of several steady quasi-one-dimensional inviscid fluid flow problems. The two most interesting problems are presented here. The first problem simulates shock-free continuous acceleration through a converging-diverging nozzle, and the second problem simulates a converging-diverging nozzle flow with a shock.

The duct geometry used in these problems is shown in Fig. 4.1. For both problems, the results generated by the CVFEM are compared with theoretical results obtained from isentropic flow and normal shock relations [16].

The proposed CVFEM has been formulated to solve the following set of governing equations:

Continuity:

$$\frac{d}{dx}(\rho w u) = 0 \tag{4.1}$$

Momentum:

$$\frac{d}{dx}(\rho w u u) = -w\frac{dp}{dx} + \frac{d}{dx}\left(\mu w \frac{du}{dx}\right) + S^u w + \frac{1}{3}\frac{d}{dx}\left(\mu \frac{d}{dx}(uw)\right) \tag{4.2}$$

Energy:

$$\frac{d}{dx}(\rho w u T) = \frac{d}{dx}\left(\frac{k}{c_p} w \frac{dT}{dx}\right) + w\frac{S^T}{c_p} + \frac{1}{c_p}\left(uw\frac{dp}{dx}\right) \tag{4.3}$$

State:

$$\rho = \frac{p}{RT} \tag{4.4}$$

These equations govern the steady flow of a viscous fluid through a variable area duct. The proposed CVFEM may be used to solve for inviscid, non-conducting, fluid flows when the viscosity and thermal conductivity in Eqs. (4.2) and (4.3) are

set equal to zero. The governing equations then become the Euler and energy equations for an inviscid, non-conducting flow.

The initial distributions of the dependent variables throughout the calculation domains were determined from the theoretical solution to each problem. In these problems, the duct geometry and the flow conditions at the duct inlet were specified. This information was used in the isentropic flow and normal shock relations [16] to determine the theoretical solution to the problem. To determine the initial distributions for the CVFEM solutions, a linear variation in pressure was assumed between the specified inflow and theoretical outflow pressures, and the temperature within the duct was set to the inflow boundary temperature. These pressure and temperature distributions were then used to calculate the density field, which, along with the specified inflow Mach number and the available duct geometry, allowed the specification of a velocity field which maintained mass conservation. This method was used to specify the initial conditions for both problems.

The convergence of the solution generated by the CVFEM was monitored by checking the relative change in the values of the dependent variables between iterations:

$$\epsilon_i^{\phi} = \left| \frac{\phi_i - \phi_i^*}{\bar{\phi}} \right| \tag{4.5}$$

where ϕ could represent the dependent variables u, p, or T. The asterisk in Eq. (4.5) indicates a value available from a previous iteration, and the overbar indicates a normalizing value, taken as the inlet velocity, pressure, and temperature for ϵ_i^u, ϵ_i^p, and ϵ_i^T, respectively. Iterations in the solution algorithm were terminated when the maximum of ϵ_i^u, ϵ_i^p, and ϵ_i^T was less then 10^{-6}. The relaxation parameters used in the problems presented in this section were $\alpha_u = \alpha_T = 0.5$.

4.2.2 Shock-Free Flow through a Converging-Diverging Nozzle

The isentropic continuously accelerating flow of an inviscid fluid through a converging-diverging nozzle is considered in this subsection. The problem is illustrated schematically in Fig. 4.1. A subsonic flow at Mach number M_1, static pressure p_1, and temperature T_1 enters the converging part of the nozzle and accelerates to sonic conditions at the nozzle throat. After passing through the throat, the flow continues to accelerate supersonically in the diverging portion of the nozzle, to a maximum outlet Mach number M_2, at pressure p_2 and temperature T_2. The cross-sectional area of the nozzle varies smoothly from inlet to outlet, and is given by the following relations:

$$h = h_{th} + (h_1 - h_{th})\left(1 - \frac{x}{L}\right)^2 \qquad x < L \tag{4.6}$$

$$h = h_{th} + (h_2 - h_{th})\left(\frac{x - L}{L_e}\right)^2 \qquad x \geq L \tag{4.7}$$

where, h_{th} is the height of the nozzle throat, or minimum cross-sectional area of the nozzle, h_1 and h_2 are the duct heights at the inlet and outlet, respectively, and L and L_e are the lengths of the converging and diverging portions of the nozzle, respectively.

For continuously accelerating flow to exist in the nozzle, the inflow boundary conditions, and the ratio of inlet and throat areas, have to be defined such that a subsonic flow enters the converging part of the nozzle and accelerates to sonic conditions at the nozzle throat. In the diverging portion of the nozzle, the flow will continue to accelerate supersonically when the pressure at the outflow boundary is equal to, or less than, that required to permit a continuous supersonic expansion from the nozzle throat. When this condition on outlet pressure is met, the exit Mach number, M_2, is determined by the ratio of throat and exit flow areas.

The problem considered here is that of shock-free nozzle flow, therefore, the flow at the outflow boundary is supersonic, and no outflow boundary conditions are required. At the inflow boundary, p_1, T_1, and M_1, are held fixed using specified value boundary conditions. The geometry of the nozzle used in this problem was designed to accelerate a Mach 0.3 flow to Mach 2, through a throat height of $3 \times 10^{-2} m$. The geometry and flow conditions were determined from the isentropic flow relations [16] to give:

$$\begin{array}{lll} L = 0.1m & p_1 = 100kPa & p_2 = 13.6039kPa \\ L_e = 0.1m & M_1 = 0.3 & M_2 = 2.0 \\ h_1 = 6.105 \times 10^{-2} m & T_1 = 300K & \\ h_{th} = 3 \times 10^{-2} m & & \\ h_2 = 5.0625 \times 10^{-2} m & & \end{array} \tag{4.8}$$

Results were generated on six grids with uniform distributions of 25, 51, 101, 201, 301, and 401 nodes. In each of these grids, a node was always placed at the nozzle throat. The distributions of M, p/p_0, and T/T_0 from both numerical and theoretical solutions are shown in Figs. 4.2 and 4.3. The pressure and temperature are normalized with respect to the stagnation pressure and temperature, respectively.

The solutions generated on all of the grids are in good agreement with the theoretical solution in the subsonic portion of the flow. The increased accuracy obtained with higher grid resolution becomes quite apparent in the supersonic portion of the flow. The largest error in the flow variables occurs in the outflow Mach number, M_2. The calculated values of M_2, M_{2calc}, generated on each of the grids, and the percentage error in this value when compared with the theoretical value of 2.0, are reported in Table 4.1.

The percentage error reduces by a factor of approximately one half when the grid spacing is halved. The values of M_{2calc} generated on the 101, 201, and 401 node grids were used in the following equation:

$$M_{2num} = M_{2calc} + C(\Delta x)^n \tag{4.9}$$

to determine the order of accuracy of the proposed CVFEM. In Eq. (4.9), M_{2num} is the calculated value of M_2 that would be expected in a grid independent solution, and n is the order of accuracy of the method based on the grid size, Δx. Solving for n and M_{2num}, gives values of 0.9848 and 1.9999, respectively. This means that the proposed one-dimensional CVFEM is first-order accurate. This is an expected result, because MAss Weighted (MAW) interpolation reduces to an upwinding scheme in one-dimensional flows, and upwinding is recognized as being first-order accurate when viewed as a truncation of a Taylor's series expansion.

Calculated values for the throat Mach number, M_{th}, and the percentage error when it is compared with the theoretical value of 1.0, are also included in Table 4.1. As can be seen from this table, the numerical M_{th} is never 1.0, however, it increases from a value of 0.9778 on the 25 node grid, for an error of -2.22%, to a value of 0.9936 on the 401 node grid, for an error of -0.64%. It should be noted that for all grids, the Mach number at the first node past the throat is always slightly larger than 1.0.

4.2.3 Converging-Diverging Nozzle Flow with a Normal Shock

Inviscid flow through a converging-diverging nozzle, with a normal shock in the divergent part of the nozzle, is considered in this subsection. The problem is illustrated schematically in Fig. 4.1. The subsonic flow at Mach number M_1, static pressure p_1, and temperature T_1, enters the duct and accelerates to sonic conditions at the nozzle throat. In the divergent portion of the duct, the flow begins to accelerate supersonically, however, the outlet static pressure, p_2, is specified such that it will not permit continuous supersonic acceleration. Due to this imposed

outlet pressure, a normal shock is generated in the nozzle. After the shock, the flow decelerates subsonically to M_2, p_2, and T_2 at the nozzle exit.

The flow through a converging-diverging nozzle is shock-free when the back pressure at the nozzle outlet is equal to, or less than, that required for continuous supersonic acceleration in the divergent part of the nozzle. If the back pressure is higher than this value, a shock will be generated in the divergent portion of the nozzle, and the flow decelerates subsonically after the shock. The position and strength of this shock are determined from the nozzle geometry and the value of the outlet pressure. If the back pressure is high enough, the shock propagates upstream until the throat, and beyond this condition the nozzle acts as a conventional venturi tube [16]. In this problem, the geometry and inflow conditions of the nozzle are the same as those given in Section 4.2.2, for a nozzle designed for shock-free acceleration from Mach 0.3 to Mach 2.0. A shock was specified to occur at Mach 1.5, and the duct geometry, inlet conditions, and pre-shock Mach number ($M_{shk} = 1.5$) were used in the isentropic flow and normal shock relations [16] to generate a theoretical solution for the flow through the nozzle:

$$
\begin{array}{lll}
L = 0.1m & p_1 = 100kPa & M_{shk} = 1.5 \\
L_e = 0.1m & T_1 = 300K & x_{shk} = 0.15062m \\
h_1 = 6.105 \times 10^{-2}m & M_1 = 0.3 & M_{aft} = 0.70109 \\
h_{th} = 3 \times 10^{-2}m & p_2 = 88.3127kPa & \\
h_2 = 5.0625 \times 10^{-2}m & M_2 = 0.40672 &
\end{array}
\tag{4.10}
$$

where M_{shk} and M_{aft} are the pre- and post-shock Mach numbers, respectively, and x_{shk} is the position at which the shock occurs. To simulate this problem numerically, the inlet conditions M_1, p_1, and T_1 were held fixed using specified value boundary conditions. The flow aft of the shock is subsonic, so a pressure must be specified at the outflow boundary. This pressure was fixed at the theoretical value required to generate a shock at Mach 1.5. This problem was simulated on three uniform grids consisting of 51, 101, and 401 nodes.

The variation of M, p/p_0, and T/T_0 along the nozzle for the numerical and theoretical [16] solutions are illustrated in Fig. 4.4. The stagnation pressure and temperature used to normalize the static pressure and temperature in these figures are the values of p_0 and T_0 at the inflow boundary. As shown in Fig. 4.4, all CVFEM solutions capture the shock in the divergent portion of the nozzle and the subsonic deceleration aft of the shock. The shock is smeared over several grid points, however, as illustrated by the finite gradients of M, p/p_0, and T/T_0 across the shock. The degree of smearing is reduced, and the resolution of the shock is improved, with an increase in the number of nodes.

Results from the CVFEM solutions are reported in Table 4.2. The values of M_{shk}, the maximum Mach number prior to the shock, and the percentage error in this value compared with the theoretical M_{shk} of 1.5, are recorded in this table. The position of M_{shk}, x_{shk}, compared with the theoretical location of the shock, $x_{shk} = 0.15062m$, is also included. As shown in Table 4.2, the maximum value of M_{shk} was underestimated by all three CVFEM solutions, with the maximum value of 1.4446 obtained on the 401 node mesh, for an error of -3.69%. The position of M_{shk} is also underestimated by the CVFEM solution, with the best estimate from the 401 node mesh in error by -2.74%. This underestimation of M_{shk} and x_{shk} is due to the smearing of steep gradients inherent in the CVFEM due to the use of upwind interpolation. In Table 4.2, the smearing of the shock is measured by the distance Δx_{shk}, which is defined as the distance from the position of M_{shk} to the position at which the Mach number is equal to, or less than, the theoretical post-shock Mach number, $M_{aft} = 0.70109$, while N_{shk} is defined as the number of nodes included in this distance. As should be expected, the degree of smearing is reduced on the finer mesh, to a minimum of 0.0065m, even though the number of nodes within the shock increases to a maximum of 13. Smearing of the shock can

be significantly reduced with the use of adaptive grids [9], but the application of such grids was outside the scope of this thesis.

4.2.4 Summary

The problems presented in this section have demonstrated that the proposed one-dimensional CVFEM can generate solutions to isentropic and non-isentropic, inviscid, non-conducting compressible fluid flow problems that are in good agreement with theoretical solutions. The method has been found to be first-order accurate in the problems solved.

4.3 Two-Dimensional Test Problems

4.3.1 Introduction

The results generated by the proposed two-dimensional CVFEM in the solution of five compressible flow problems are presented in this section. The problems presented here include: (1) inviscid subsonic, transonic, and supersonic flow through a channel with a circular arc bump on one wall; (2) inviscid flow through a two-dimensional planar converging-diverging nozzle; and (3) the interaction of a shock with a laminar boundary layer on a flat plate. The solutions generated by the proposed CVFEM are compared with numerical and experimental data available in the literature.

The proposed CVFEM has been formulated to solve the following set of equations:

Continuity:

$$\frac{\partial}{\partial x}(\rho u) + \frac{\partial}{\partial y}(\rho v) = 0 \tag{4.11}$$

x-momentum:

$$\begin{aligned}\frac{\partial}{\partial x}(\rho uu) + \frac{\partial}{\partial y}(\rho vu) &= -\frac{\partial p}{\partial x} + \frac{\partial}{\partial x}\left(\mu\frac{\partial u}{\partial x}\right) + \frac{\partial}{\partial y}\left(\mu\frac{\partial u}{\partial y}\right) + S^u \\ &+ \frac{1}{3}\frac{\partial}{\partial x}\left(\mu\frac{\partial u}{\partial x}\right) + \frac{\partial}{\partial y}\left(\mu\frac{\partial v}{\partial x}\right) - \frac{2}{3}\frac{\partial}{\partial x}\left(\mu\frac{\partial v}{\partial y}\right)\end{aligned} \tag{4.12}$$

y-momentum:

$$\begin{aligned}\frac{\partial}{\partial x}(\rho uv) + \frac{\partial}{\partial y}(\rho vv) &= -\frac{\partial p}{\partial y} + \frac{\partial}{\partial x}\left(\mu\frac{\partial v}{\partial x}\right) + \frac{\partial}{\partial y}\left(\mu\frac{\partial v}{\partial y}\right) + S^v \\ &+ \frac{1}{3}\frac{\partial}{\partial y}\left(\mu\frac{\partial v}{\partial y}\right) + \frac{\partial}{\partial x}\left(\mu\frac{\partial u}{\partial y}\right) - \frac{2}{3}\frac{\partial}{\partial y}\left(\mu\frac{\partial u}{\partial x}\right)\end{aligned} \tag{4.13}$$

Energy:

$$\begin{aligned}\frac{\partial}{\partial x}(\rho uT) + \frac{\partial}{\partial y}(\rho vT) &= \frac{\partial}{\partial x}\left(\frac{k}{c_p}\frac{\partial T}{\partial x}\right) + \frac{\partial}{\partial y}\left(\frac{k}{c_p}\frac{\partial T}{\partial y}\right) + S^T \\ &\frac{1}{c_p}\left(u\frac{\partial p}{\partial x} + v\frac{\partial p}{\partial y}\right) + \frac{1}{c_p}\Phi\end{aligned} \tag{4.14}$$

State:

$$\rho = \frac{p}{RT} \tag{4.15}$$

Although the proposed method has been developed to solve viscous flow problems, it was also tested in the context of some inviscid flow problems. There are very few laminar viscous compressible flow problems, that have been used for testing numerical methods, reported in the literature. The inviscid flow problems used here have been implemented by other researchers, and they demonstrate the effectiveness of the proposed CVFEM in the simulation of some important features of compressible flows.

The equations governing steady, two-dimensional, inviscid, non-conducting, compressible fluid flow are obtained from Eqs. (4.11) to (4.15) by setting the dynamic

viscosity, μ, and the thermal conductivity, k, equal to zero.

x-momentum:

$$\frac{\partial}{\partial x}(\rho uu) + \frac{\partial}{\partial y}(\rho vu) = -\frac{\partial p}{\partial x} + S^u \tag{4.16}$$

y-momentum:

$$\frac{\partial}{\partial x}(\rho uv) + \frac{\partial}{\partial y}(\rho vv) = -\frac{\partial p}{\partial y} + S^v \tag{4.17}$$

Energy:

$$\frac{\partial}{\partial x}(\rho uT) + \frac{\partial}{\partial y}(\rho vT) = \frac{S^T}{c_p} + \frac{1}{c_p}\left(u\frac{\partial p}{\partial x} + v\frac{\partial p}{\partial y}\right) \tag{4.18}$$

Equations (4.16) and (4.17) are referred to as the Euler equations. The continuity and state equations are unmodified.

In all problems presented in this section, the convergence of the iterative solution algorithm was monitored using Eq. (4.5). In this equation, the changes in the values of u, v, and p at each node in the calculation domain, between successive iterations of the solution algorithm, were normalized with respect to inlet u velocity for ϵ_i^u and ϵ_i^v, and inlet static pressure for ϵ_i^p. The iterations in the solution algorithm were terminated when the maximum of all ϵ_i values was less than 10^{-5}. In the problems considered here, the ϵ_i^u component was the slowest to reach the convergence criteria.

The following subsections describe the problems solved, and the solutions generated by the proposed CVFEM are compared with available numerical or experimental data.

4.3.2 Inviscid Flow through a Channel with a Circular Arc Bump

Introduction

The simulation of inviscid flow through a channel with a circular arc bump on one wall has become a standard test problem to validate numerical methods for compressible flow. The problem is illustrated schematically in Fig. 4.5. A flow

at Mach number M_1, static pressure p_1, and temperature T_1, enters a channel of length 3L and height L. A circular arc bump of height h_B and chord L is centered on the bottom wall of the channel. The height of the bump is defined in terms of a percentage of the chord length. The flow exits the duct at Mach number M_2, static pressure p_2, and temperature T_2. Problems involving subsonic, transonic, and supersonic flows through the channel have been solved.

The equations used to simulate this problem were the Euler equations, Eqs. (4.16) and (4.17), the energy equation, Eq. (4.18), the continuity equation, Eq. (4.11), and the equation of state, Eq. (4.15). The boundary conditions used were specified value at inlet and tangency at the walls. In the application of the tangency boundary condition, the singularities at the leading and trailing edges of the bump had to be taken into account. To correctly simulate the shape of the bump at the leading edge, the v velocity was set such that the flow vector was parallel with the slope of the bump. At the trailing edge, however, the v velocity was set equal to zero in order to provide tangency with the channel wall. It is not possible to ensure tangency with both the channel wall and the surface of the bump, so the proposed treatment is a compromise. This treatment is not symmetric, and it leads to some asymmetry of the solutions in one of the problems discussed below. At the inflow of all test problems with this geometry, the inlet static pressure, temperature, and Mach number were fixed. At the outflow of the subsonic and transonic flow test problems, the flow was subsonic, therefore, the outflow static pressure was set to a fixed value. In the problems solved here, the inlet and outlet static pressures were defined to be equivalent. For the supersonic flow problems no outflow boundary conditions were required.

In the definition of the initial flow conditions for each problem, the pressure, temperature, and velocity specified at inlet were assumed to prevail throughout the

duct. During the solution of the problems, the relaxation parameters α_u, α_v, and α_T were assigned values of 0.3.

Numerical results to these problems have been generated by several researchers, for example Ni [18] and Eidelman et al. [19]. The results obtained in [18] and [19] were used to evaluate the solutions from the proposed CVFEM. Ni [18] used an explicit second-order accurate FVM, incorporating multigrid solution techniques, on a 65×17 node grid having 33 nodes concentrated over the bump. Eidelman et al. [19] used first- and second-order accurate Godunov FDM's on grids of unspecified resolution. The results generated by the CVFEM of Hookey [9] on a 61 × 21 node uniform grid are also used for comparison.

The proposed CVFEM was used with two different grids, as shown in Fig. 4.6, to generate solutions to each of the three problems considered. Each grid consisted of 61×21 nodes or 2400 elements. An initial or 'uniform' grid was generated by specifying a uniform distribution of nodes around the boundary of the calculation domain, and using transfinite interpolation [23] to generate the internal mesh. The second grid concentrated nodes near the bottom surface of the duct and near the bump as shown in Fig. 4.6b.

In the discussion of the results generated by the proposed CVFEM, the distributions of M, p/p_0, and T/T_0 along the top and bottom walls of the channel are compared with the data of Ni [18], Eidelman et al. [19] and Hookey [9]. Plots of the isoMach lines are also included to validate the physical features of the calculated flow.

Subsonic Flow

In the simulation of inviscid subsonic flow through the channel, the inlet Mach number was set equal to 0.5, and the height of the bump was defined as 10% of the

chord. In this problem, the singularities at the leading and trailing edges of the bump generate pressure disturbances that propagate up and downstream to provide a smooth change in Mach number. The flow accelerates over the forward part of the bump, due to the decrease in flow area, to a maximum velocity over the center of the bump. The flow then decelerates on the aft portion of the bump. Since the flow remains subsonic and is inviscid, there should be no dissipative losses, therefore, the flow should return to the inlet Mach number at outlet. Dissipative losses would manifest themselves as a reduction in stagnation pressure of the flow, and since the static pressures at inlet and outlet are equivalent, this would lead to an outlet Mach number less than 0.5. The difference between M_1 and M_2 illustrates the degree of pressure recovery in the solution.

The following geometry and flow conditions were used in the simulation of this problem:

$$\begin{array}{lll} L = 0.1m & p_1 = 100kPa & p_2 = 100kPa \\ h_B = 0.01m & T_1 = 300K & \\ & M_1 = 0.5 & \end{array} \tag{4.19}$$

The Mach number distributions along the upper and lower walls of the channel are shown in Fig. 4.7, and the isoMach lines are plotted in Fig. 4.8

The results generated by the proposed CVFEM are compared with those of Ni [18] and Hookey [9] in Fig.4.7. As shown in this figure, the CVFEM solutions give a nonsymmetric solution, but this is due to the different boundary conditions applied at the leading and trailing edges of the bump. The proposed CVFEM underpredicts the maximum Mach number, with the best result of 0.668 being obtained on grid 2. The maximum Mach numbers predicted by Ni [18] and Hookey [9] are 0.694 and 0.680, respectively. The proposed CVFEM also indicates relatively poor pressure recovery aft of the bump. The isoMach lines in Fig. 4.8 indicate the asymmetry introduced due to the boundary conditions.

Transonic Flow

In the simulation of inviscid transonic flow through the channel, the inlet Mach number was set equal to 0.675, and the bump height was specified as 10% of the chord. For this inflow Mach number and duct geometry, the Mach number of the flow smoothly reduces to a minimum at the bump leading edge. The flow then accelerates over the bump to form a supersonic region that is terminated by a normal shock on the aft portion of the bump. After the shock, the flow recovers to near inlet conditions. Since a shock is present, the stagnation pressure near the bottom channel wall reduces, therefore, the outlet Mach number near the bottom surface is less than the inlet Mach number, because the inlet and outlet static pressures are equivalent. There is some pressure recovery aft of the shock, however, as the shock does not extend across the full height of the duct. The reduction in Mach number at the outlet reflects the loss in stagnation pressure.

The following geometry and flow conditions were specified for this problem:

$$\begin{array}{lll} L = 0.1m & p_1 = 100kPa & p_2 = 100kPa \\ h_B = 0.01m & T_1 = 300K & \\ & M_1 = 0.675 & \end{array} \tag{4.20}$$

The Mach number distributions along the upper and lower walls of the channel are plotted in Fig. 4.9 and the isoMach lines are shown in Fig. 4.10

In Fig.4.9, the results generated by the proposed CVFEM are compared with the FDM results of Eidelman et al. [19] and Hookey [9]. This comparison is not very favourable for the proposed CVFEM, as the maximum Mach number on the bump is underpredicted, and the shock is not apparent. The maximum Mach numbers predicted by the proposed CVFEM are 1.0048 and 1.04 on grids 1 and 2, respectively. The value predicted by Eidelman et al. is 1.187 and 1.142 is predicted by Hookey. The location of the maximum Mach number on the upper wall is also poorly predicted by the proposed CVFEM, as is the pressure recovery aft of the

shock. This poor performance is related to the first-order nature of the mass-weighted interpolation scheme used in the proposed methods. Both Eidelman et al. [19] and Hookey [9] use higher order schemes which do not smear variations in flow properties as much as the proposed method, and both give more accurate representations of physical flows.

The isoMach plots shown in Fig. 4.10, illustrate the expected asymmetry in the solution, but the shock is not present.

Supersonic Flow

Inviscid supersonic flow through the channel was simulated using an inlet Mach number of 1.65 and a bump height of 4% chord length. When the flow through the channel is subsonic, pressure disturbances generated by the singularities at the leading and trailing edges of the bump can propagate upstream to provide a smooth decrease in Mach number. When the flow is supersonic, however, as in this problem, these disturbances coalesce into oblique shocks. The leading edge shock reflects off the upper channel wall, and interacts with the trailing edge shock. The leading and trailing edge, and reflected shocks are weakened by expansion waves propagated into the flow from the convex surface of the bump. This problem is an interesting and challenging test of the proposed CVFEM as three shocks and the appropriate turning of the flow across the shocks, must be captured.

The following geometry and flow conditions were used in the simulation of this problem:

$$\begin{array}{ll} L = 0.1m & p_1 = 100kPa \\ h_B = 0.004m & T_1 = 300K \\ & M_1 = 1.65 \end{array} \tag{4.21}$$

The Mach number distributions along the upper and lower walls are shown in Fig. 4.11 and the isoMach lines are plotted in Fig. 4.12.

In Fig. 4.11, the results generated by the proposed CVFEM are compared with

the FDM results of Eidelman et al. [19], and the CVFEM results of Hookey [9]. This figure illustrates that the proposed CVFEM underestimates the maximum Mach number on the lower wall. Also the minimum Mach number, at the location where the shock is reflected from the upper wall, is overestimated. Further, the influence of the reflected shock on the lower wall Mach number at the end of the domain is overestimated. These difficulties are due to the low-order of the interpolation scheme used in the proposed CVFEM.

The isoMach lines shown in Fig. 4.12 indicate that the proposed CVFEM has captured the shocks at the leading and trailing edges of the bump, with better refinement of the shock on grid 2. The shock reflection is rather diffuse, however, as shown by the coarse spacing of the isoMach lines on the upper wall. The effect of the coarse mesh aft of the bump is apparent from Fig. 4.12b.

4.3.3 Inviscid Flow through a Planar Converging-Diverging Nozzle

In this problem, the continuous acceleration of an inviscid flow from subsonic to supersonic speeds in a planar converging-diverging nozzle is simulated. The problem is illustrated schematically in Fig. 4.13. Planar or rectangular cross-section nozzles have been used on the jet engines fitted to high performance aircraft [20]. These nozzles allow variable engine inlet geometry, and thrust vectoring or reversing, which permits the design of highly maneuverable planes possessing better performance characteristics than would be possible with axisymmetric nozzles [20]. A series of tests were performed by NASA to determine the performance of several nozzle designs, and the experimental data from one of these tests is used to check the results produced by the proposed CVFEM. The nozzle simulated is the B2 nozzle reported by Mason et al. [20]. With reference to Fig. 4.13, which shows the

bottom half of the nozzle, the B2 nozzle has the following dimensions:

$$\begin{array}{lll} h_{th} = 1.37 \times 10^{-2}m & \theta = 22.33^{o} & h_1 = 3.52 \times 10^{-2}m \\ L_t = 5.78 \times 10^{-2}m & \beta = 11.24^{o} & h_2 = 2.46 \times 10^{-2}m \\ L_e = 5.78 \times 10^{-2}m & r_c = 2.74 \times 10^{-2}m & \end{array} \tag{4.22}$$

A smooth transition from the contoured throat to the straight duct walls gives inlet and outlet duct half-heights, h_1 and h_2, of $3.52 \times 10^{-2}m$ and $2.46 \times 10^{-2}m$, respectively. The ratios of these duct heights gives a ratio of inlet stagnation pressure to outlet static pressure of 8.813 [16]. When the NASA test conditions of $300K$ for inlet stagnation temperature, and $101.3kPa$ for outlet static pressure are used with the duct geometry in the isentropic flow relations [16], the following flow conditions are obtained:

$$\begin{array}{lll} p_1 = 859.772kPa & p_{th} = 471.633kPa & p_2 = 101.3kPa \\ T_1 = 296.8K & T_{th} = 250K & T_2 = 161K \\ M_1 = 0.23257 & M_{th} = 1.0 & M_2 = 2.07635 \end{array} \tag{4.23}$$

The calculation domain used in this simulation was the half of the nozzle shown in Fig. 4.13. This domain was discretized with the two grids shown in Fig. 4.14. These grids consisted of 31×11, and 61×21 nodes, or 600, and 2400 elements, respectively. They were generated using a uniform distribution of nodes on the boundaries of the domain, and transfinite interpolation [23] to determine the internal mesh.

The initial flow conditions in the nozzle were determined by interpolation of the results of the isentropic analysis, Eq. (4.23). The static pressure and temperature were assumed to vary linearly from the inlet to the throat, and then from the throat to the outlet boundary. The density field was calculated from the specified distribution of pressure and temperature. Using the given inlet Mach number, duct geometry, and density field, a u velocity field that maintained mass conservation was calculated. The v velocity was then defined such that the velocity vector was everywhere tangent to the local grid lines. To maintain a constant Mach number across the inlet, it was necessary to determine u and v based on the angle the grid

lines made with the inlet plane of the duct, therefore, u and v were non-constant along the nozzle entrance.

The boundary conditions used in this problem were specified static pressure, temperature, and velocity at the inlet, and specified static pressure at the outlet. Tangency conditions were applied at the duct wall and the symmetry plane. The initial and boundary conditions imply that the fluid entering the duct is not parallel with the x axis. It was found that the inflow had to be oriented in this manner to provide tangency at the duct wall, otherwise the sharp turning of the flow just after entering the nozzle, and the ill-conditioned coefficients in the discretized equations in this vicinity, led to convergence difficulties. Furthermore, this provides a realistic simulation of the physical problem, as the subsonic inlet would allow pressure disturbances caused by the flow turning to propagate upstream, and generate a smooth turning of the flow as it enters the duct.

Figures 4.15 and 4.16 show the variation in the ratio of static pressure to inlet stagnation pressure along the lower duct wall, and the symmetry plane, respectively. In these figures, the two CVFEM solutions are compared with the experimental data of Mason et al. [19]. The experimental pressure data was recorded along the centerline of the lower duct wall, and the centerline of the duct endwall. The nozzle tested in [19] had a rectangular cross-section with a constant width of $10.12 \times 10^{-2} m$. The plots in Figs. 4.15 and 4.16 show that the results generated on the 31×11 and 61×21 node grids are in good agreement with the experimental data, with the finer grid providing the expected better accuracy.

The isoMach lines generated from the CVFEM solutions are shown in Fig. 4.17. This figure illustrates that for the two CVFEM solutions the Mach number at the wall reaches a value of one before the throat, and the flow at the centerline becomes sonic just after the throat, as in a physical nozzle flow [17]. The isoMach lines aft

of the throat also demonstrate the correct physical behaviour when compared with interferograms in [16]. A comparison of Figs. 4.17a and 4.17b illustrate that the 61 × 21 node grid provides the smoothest variation of Mach number across the nozzle cross-section.

4.3.4 Shock-Laminar Boundary Layer Interaction

The simulation of an incident shock interacting with a laminar boundary layer is a severe test of a numerical method. The physical behaviour of a boundary layer in the presence of a shock is shown schematically in Fig. 4.18. In the absence of a boundary layer, a shock is reflected from a flat plate as an oblique shock of equal turning angle [16]. The pressure increase across a shock, however, causes a boundary layer to thicken in the vicinity of the shock incidence. The resulting pressure disturbance propagates upstream in the subsonic portion of the boundary layer, which leads to smearing of the pressure increase across the shock, and upstream thickening of the boundary layer. This thickening can generate compression waves that coalesce to form a reflected shock originating upstream of the incident shock. The actual origin of the reflected shock depends on the degree of streamline curvature induced by the incident shock. The incident and reflected shocks are nearly coincident only for a weak incident shock. As the shock enters the boundary layer, the changing Mach number of the flow causes it to bend, and it terminates at the sonic line [16]. This bending generates compression waves which coalesce into another reflected shock. After passing through the incident and reflected shock system, the flow external to the boundary layer attains a higher pressure than that of the flow within the layer. This pressure differential causes the flow to turn towards the wall and generate expansion waves which propagate into the freestream and weaken the reflected shocks [16]. If the difference between the freestream and

boundary layer pressures is sufficient, the flow is turned so strongly towards the wall that the consequent realignment of the flow at the wall generates compression waves and another reflected shock. The degree of boundary layer thickening and the complexity of the reflected shock structure are strongly dependent upon the strength of the incident shock. If the shock is of sufficient strength the boundary layer will separate. The most complex shock structures occur with strong shock-boundary layer interactions.

Hakkinen et al. [21] reported experimental studies of the interaction of oblique shocks with laminar boundary layers on a flat plate. Several experiments were performed at different incident shock positions, oblique shock angles, and stagnation pressures. Data reported in [21] includes the distribution of skin friction coefficient, c_f, and static to stagnation pressure ratio on the surface of the plate. This data was recorded at various values of p_2/p_1, the ratio of outlet to inlet static pressures, where p_2 was measured aft of the incident and reflected shock system, and shock Reynolds numbers, Re_{shk}, based on freestream conditions before the shock and the point of incidence of the shock, x_{shk}.

The oblique shock angle, θ, is not reported in [21], however, it can be determined by an iterative method based on satisfying the required static pressure rise, p_2/p_1, assuming that the incident shock is reflected as an oblique shock having equal turning angle [9]. The case simulated here corresponds to a pressure ratio $p_2/p_1 = 1.2$, and a shock Reynolds number, Re_{shk}, of 2.84×10^5. The incident point of the shock, x_{shk}, is $4.8768 \times 10^{-2} m$ [21], and the inlet Mach number, $M_1 = 2.0$, allows complete specification of the variables defining this problem [9]:

$$\begin{array}{ll} x_{shk} = 4.8768 \times 10^{-2} m & p_1 = 12.9399 kPa \\ Re_{shk} = 2.84 \times 10^5 & \theta = 31.3471^o \\ p_2/p_1 = 1.20 & c_p = 1005.6 J/kg/K \\ M_1 = 2.0 & Pr = 0.72 \\ T_1 = 293 K & \end{array} \tag{4.24}$$

The value of c_p was evaluated at 293K. The dynamic viscosity, μ, was determined from the Sutherland-law approximation [25]:

$$\mu = 1.716 \times 10^{-5} kg/m/s \left(\frac{383K}{T + 110K}\right)\left(\frac{T}{273K}\right)^{3/2} \tag{4.25}$$

The grid used to simulate this problem has to be very fine near the plate, in order to properly resolve the behaviour of the boundary layer. The laminar boundary layer for a compressible adiabatic Mach 2 flow over a flat plate thickens with distance from the leading edge, x, as [9]:

$$\delta_x = \frac{7x}{(Re_x)^{1/2}} \tag{4.26}$$

which gives a boundary layer thickness at the incident shock location, δ_{shk}, of only $6.406 \times 10^{-4} m$. In [27], results were generated on a 32×32 node grid that extended 26% of x_{shk} in front of the plate, and 56% of x_{shk} aft of the incident point. In [26], results were generated using a domain extending of x_{shk} upstream of the plate, and 50% downstream of the incident point. A uniform distribution of nodes in the x direction was employed. In the y direction, the domain was split into two sections, one corresponding to a stretched fine mesh within the boundary layer, and the other to a uniform coarse mesh in the freestream; 16 nodes were placed in each section. The fine mesh had a thickness of approximately 2.5 times the boundary layer thickness δ_L. The height of the coarse mesh was specified such that the total height of the domain was approximately 14 times the height of the fine mesh. In the CVFEM of Hookey [9] this problem was simulated on a 61×41 mesh with a total of 24 nodes placed within the fine mesh region and 17 in the freestream section.

Meshes consisting of 121×81 and 61×41 nodes, as shown in Fig. 4.14, were used in the simulation of this problem. The calculation domain extended from $x/x_{shk} = -0.5$, to $x/x_{shk} = 1.5$ as shown in Fig. 4.20. The domain was divided into two sections, as in [9, 26, 27], with coarse and fine sections to accommodate

the freestream and boundary layer, respectively. As in [9] the thickness of the fine mesh was chosen to be approximately $3\delta_L$, or $2.34 \times 10^{-3}m$, while the height of the coarse mesh was chosen to give a total domain height of approximately $33\delta_L$, or $2.525 \times 10^{-2}m$. For the 121×81 grid, a total of 47 nodes were placed within the fine mesh region and 34 in the freestream section, while the 61×41 grid employed 24 nodes in the fine mesh region and 17 nodes in the freestream section. The grids within each section were stretched to concentrate points near the plate, and then to provide a smooth transition from fine to coarse meshes. These grids were stretched using the following power law equation [9]:

$$y_j = y_0 + y_{max}\left(\frac{j-1}{j_{max}-1}\right)^n \tag{4.27}$$

where y_0 is the height at which the section begins, y_{max} is the height of the appropriate section, j_{max} is the number of nodes in that section, and j varies from 1 to j_{max}. For the grids used here, n was assigned values of 1.3 in the fine and coarse meshes. A uniform distribution of nodes in the x direction was used in both meshes.

The equations solved in the simulation of this problem were the continuity, Navier-Stokes, energy, and state equations, Eqs. (4.11) to (4.15). Due to the large variation in element size, the coefficient matrices of the discretized equations were not diagonally dominant, and this required the use of heavy under-relaxation to promote convergence. The data reported in this thesis was obtained with α_u, α_v and α_T assigned the value of 0.3.

The boundary conditions applied to this problem were specified velocity, static pressure, and temperature on the inflow boundary, and the top boundary of the calculation domain. At the inlet plane the Mach number, pressure, and temperature were assigned the values of M_1, p_1, and T_1 in Eq. (4.24): the v velocity component

was set equal to zero and the u velocity component was determined from M_1 and T_1. The u and v velocity components were set equal to zero on the plate to provide a no slip boundary condition. Between the inlet plane and the leading edge of the plate, symmetry conditions were applied on the lower boundary, that is $v = 0$, and no-flow, no-diffusion for u. At the supersonic outflow boundary, no boundary conditions were specified.

A shock was imposed on the boundary layer by altering the boundary conditions on the upper domain boundary. These conditions were determined from the normal shock relations [16], assuming that the shock angle was 31.3471°. The post-shock conditions, indicated by subscript y, are [9]:

$$\begin{array}{llll} u_y = 674.43m/s & p_y = 14.1857kPa \\ v_y = -19.37m/s & T_y = 300.8K \end{array} \tag{4.28}$$

These values were specified along the top of the calculation domain, at and after the origin of the oblique incident shock, as shown in Fig. 4.20.

The results generated by the proposed CVFEM are compared with the experimental data of Hakkinen et al. [21] and the numerical results of Hookey [9]. The distribution of the static pressure ratio, p/p_1, and skin friction, c_f, along the surface of the plate are shown in Figs. 4.21 and 4.22, respectively.

The pressure ratio, p_2/p_1, calculated from the outlet and inlet static pressures in the calculation domain, was 1.1995 for the 121×81 grid which is in excellent agreement with the experimental value of 1.2 [21]. The computed gradient of pressure across the incident and reflected shock system is less steep than that occurring in the experimental data. The relative smearing of the pressure rise in the CVFEM solutions compared to the experimental data is quite evident. At the origin of the incident shock, the boundary conditions were specified to give a discontinuous change in conditions across the shock. As the shock propagated into the calculation

domain, it was smeared over several nodes, and approximated by finite gradients. The experimental data illustrates the upstream and downstream propagation of the pressure disturbance within the boundary layer [16]. This region is larger in the CVFEM solutions, because the shock is smeared by the numerical method, and it is no longer a discontinuity when it hits the boundary layer. In comparison with the results of Hookey, the proposed CVFEM appears to have shifted the pressure rise downstream from the physical location, i.e. the physical location of the shock interaction is better predicted by the CVFEM in [9].

The smearing of the shock is responsible for the poor agreement between the experimental and numerical values of c_f. Although both CVFEM solutions show a decrease in c_f near the shock system, which indicates a slowing of the flow near the plate, and consequent thickening of the boundary layer, the decrease is not as large as in the experimental data or that in the CVFEM simulation in [9]. The experimental data shows a large decrease in c_f, to a minimum of 3.48×10^{-4}, while the corresponding value from the 121×81 grid is 8.8263×10^{-4}, and 9.9812×10^{-4} is for the 61×41 grid. The minimum value of c_f predicted by the CVFEM in [9] is 6.6647×10^{-4} on a 61×41 grid. Before and after the shock system, the numerical values of c_f are in good agreement with the experimental data. It appears that the lower-order interpolation scheme used in this thesis is not capable of predicting the appropriate extent of the shock-boundary layer interaction. The previous method described in [9], which used a higher-order interpolation scheme appears to better predict this behaviour, and suggests that it should be revisited.

Summary

The results presented in this section have shown that the proposed method is capable of simulating compressible viscous flows, but its accuracy is severely limited by

the low-order mass-weighted interpolation scheme that was employed. This scheme offers ease of implementation and derivation when compared with the previous CVFEM of Hookey [9]. The higher-order interpolation used in [9] leads to a more complex implementation, but it gives better solutions. This research indicated that the method in [9] should be revisited, in an attempt to reduce the difficulties in convergence that have arisen with that method.

N	Iter	M_{th}	% error in M_{th}	M_{2calc}	% error in M_2
25	131	0.9778	-2.22	1.7819	-10.9
51	238	0.9842	-1.58	1.8904	-5.48
101	434	0.9882	-1.18	1.9439	-2.80
201	804	0.9912	-0.88	1.9716	-1.42
301	1158	0.9927	-0.73	1.9809	-0.96
401	1502	0.9936	-0.64	1.9856	-0.72

Table 4.1: Shock-free flow through a converging-diverging nozzle: Accuracy of the predicted throat and outlet Mach numbers.

N	Iter	M_{shk}	% error in M_{shk}	x_{shk}	% error in x_{shk}	Δx_{shk}	N_{shk}
51	980	1.1313	-24.58	0.1280	-15.02	0.0320	8
101	1137	1.2942	-13.72	0.1360	-9.71	0.02	10
401	4190	1.4446	-3.69	0.1465	-2.74	0.0065	13

Table 4.2: Converging-diverging nozzle flow with a shock: Predicted values of M_{shk}, the position, and the thickness of the shock.

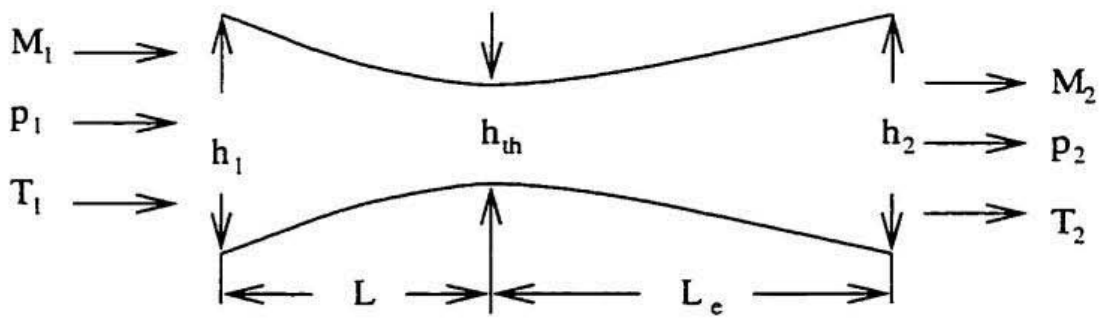

Figure 4.1: Problem schematic for quasi-one-dimensional inviscid flow through a converging-diverging nozzle.

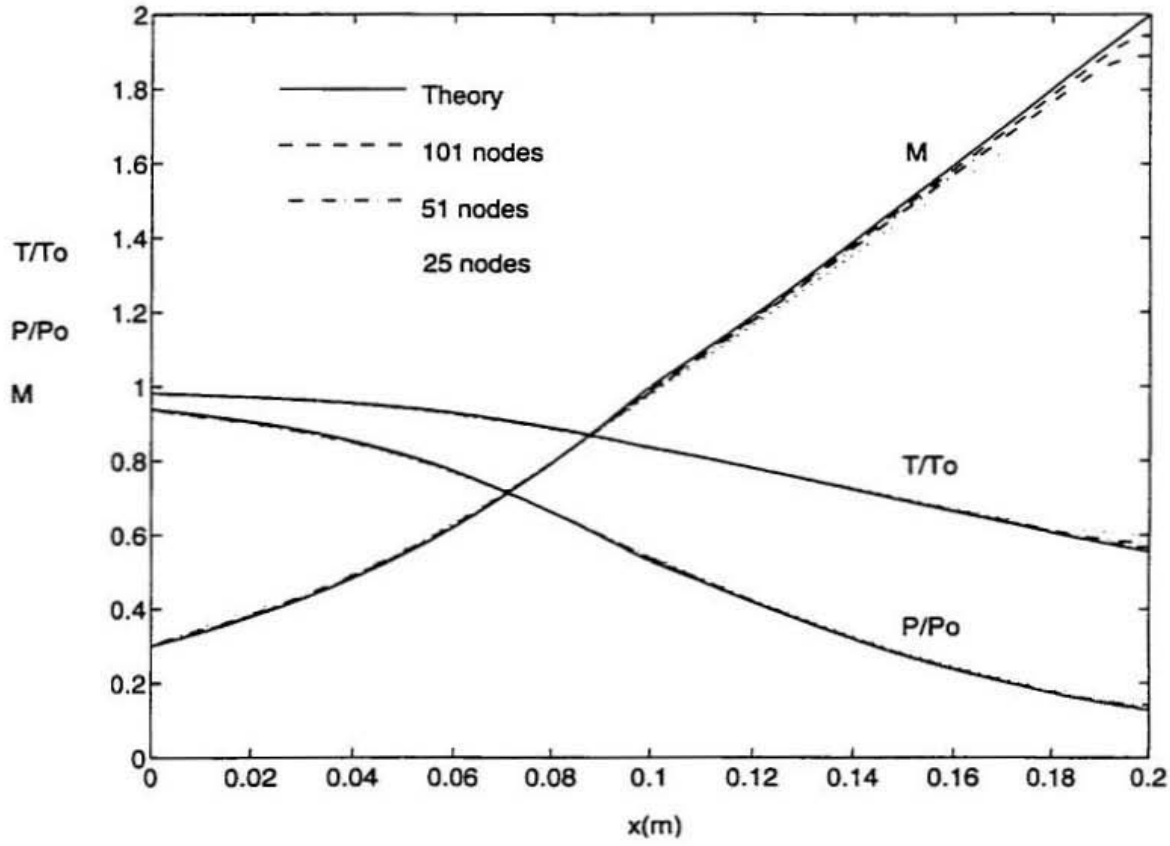

Figure 4.2: Shock-free flow through a converging-diverging nozzle (coarse mesh): distribution of M, p/p_0, and T/T_0.

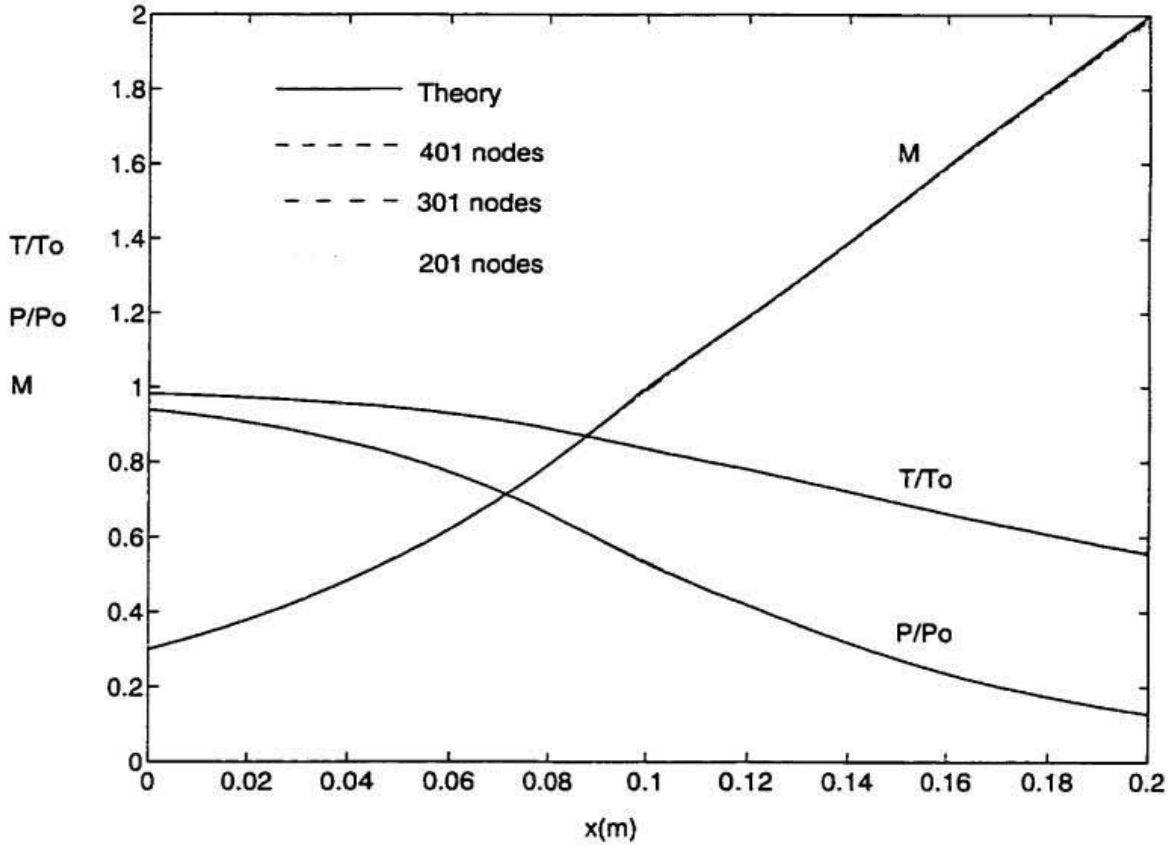

Figure 4.3: Shock-free flow through a converging-diverging nozzle (fine mesh): distribution of M, p/p_0, and T/T_0.

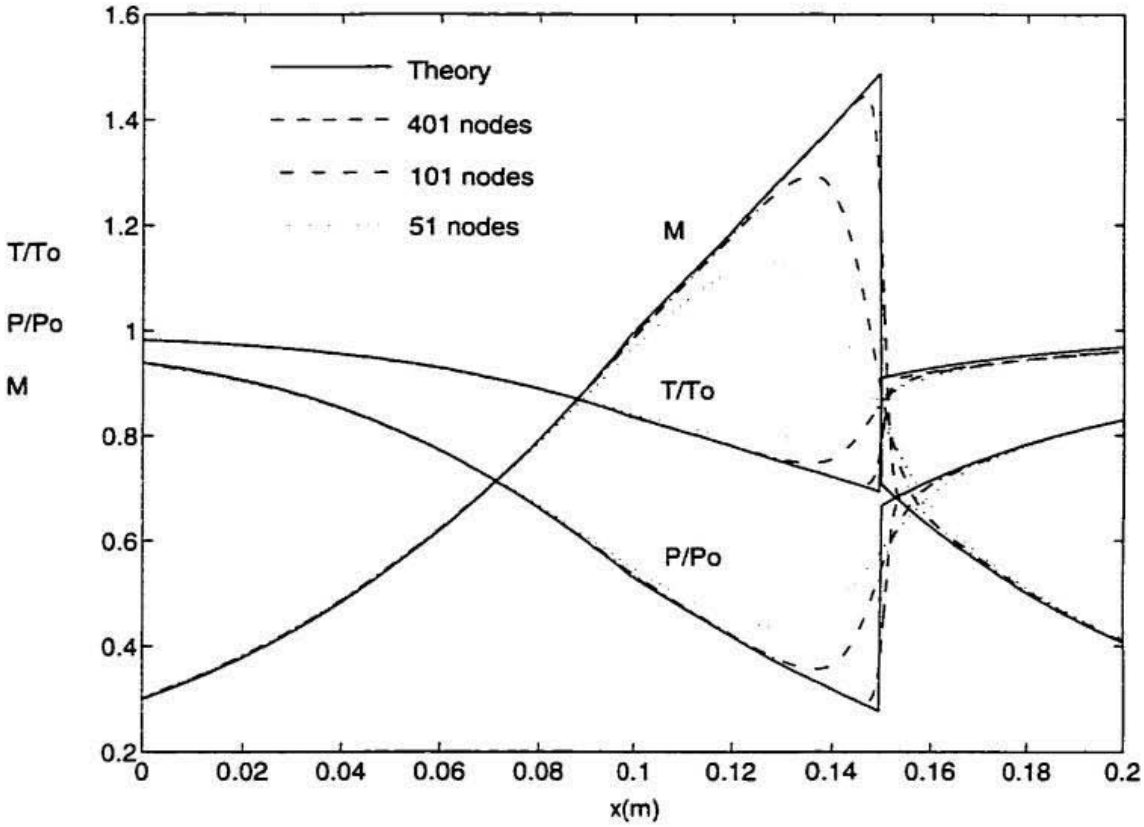

Figure 4.4: Converging-diverging nozzle flow with a shock: distribution of M, p/p_0, and T/T_0.

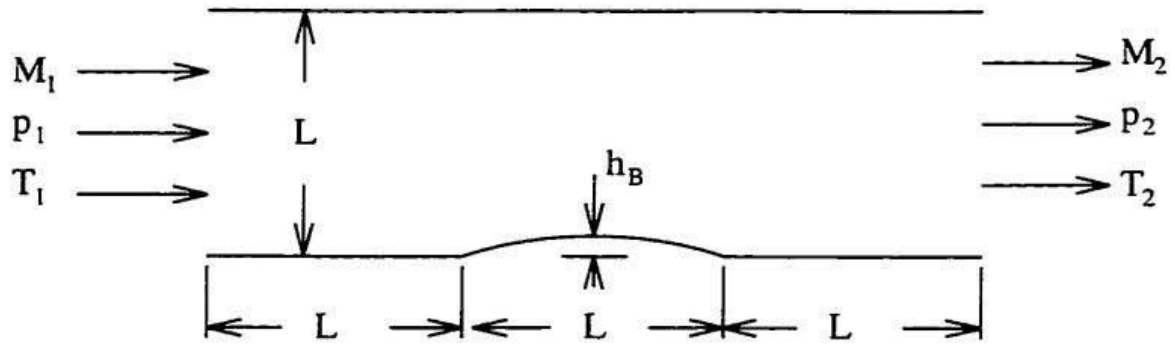

Figure 4.5: Two-dimensional inviscid flow through a channel with a circular arc bump: problem schematic.

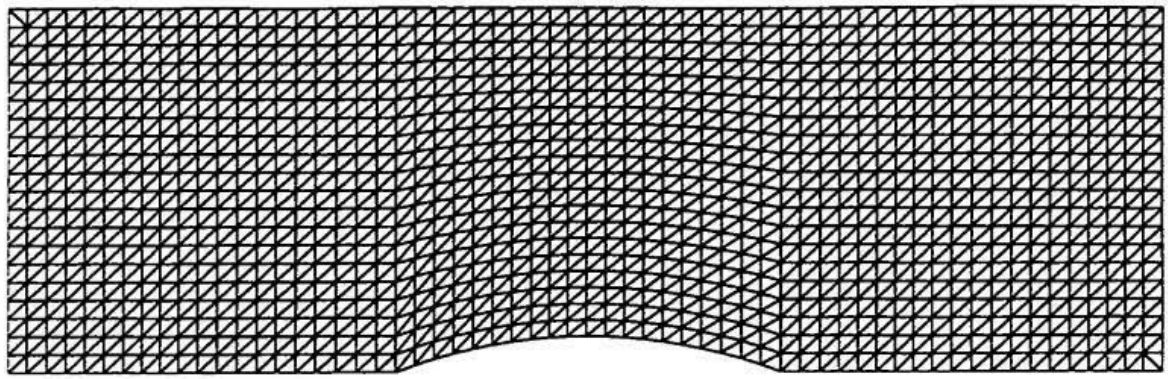

(a)

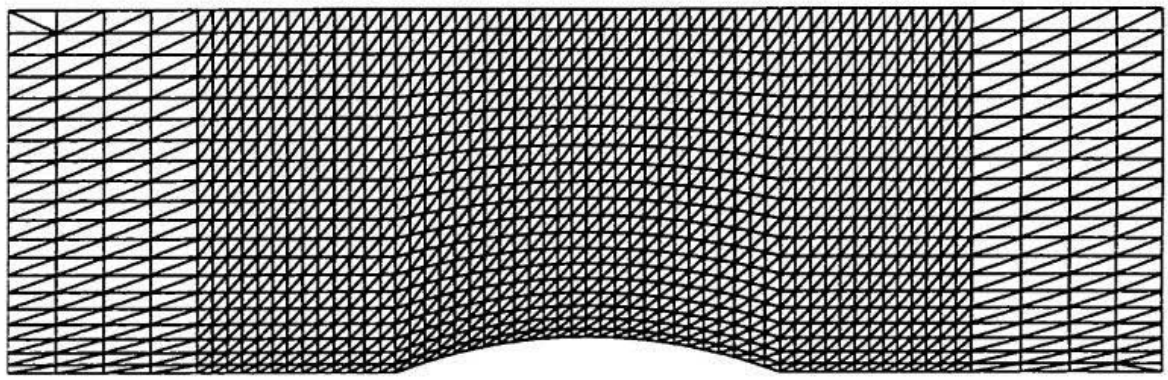

(b)

Figure 4.6: Two-dimensional inviscid flow through a channel with a circular arc bump: (a) grid 1 (uniform 61 × 21), and (b) grid 2 (nonuniform 61 × 21).

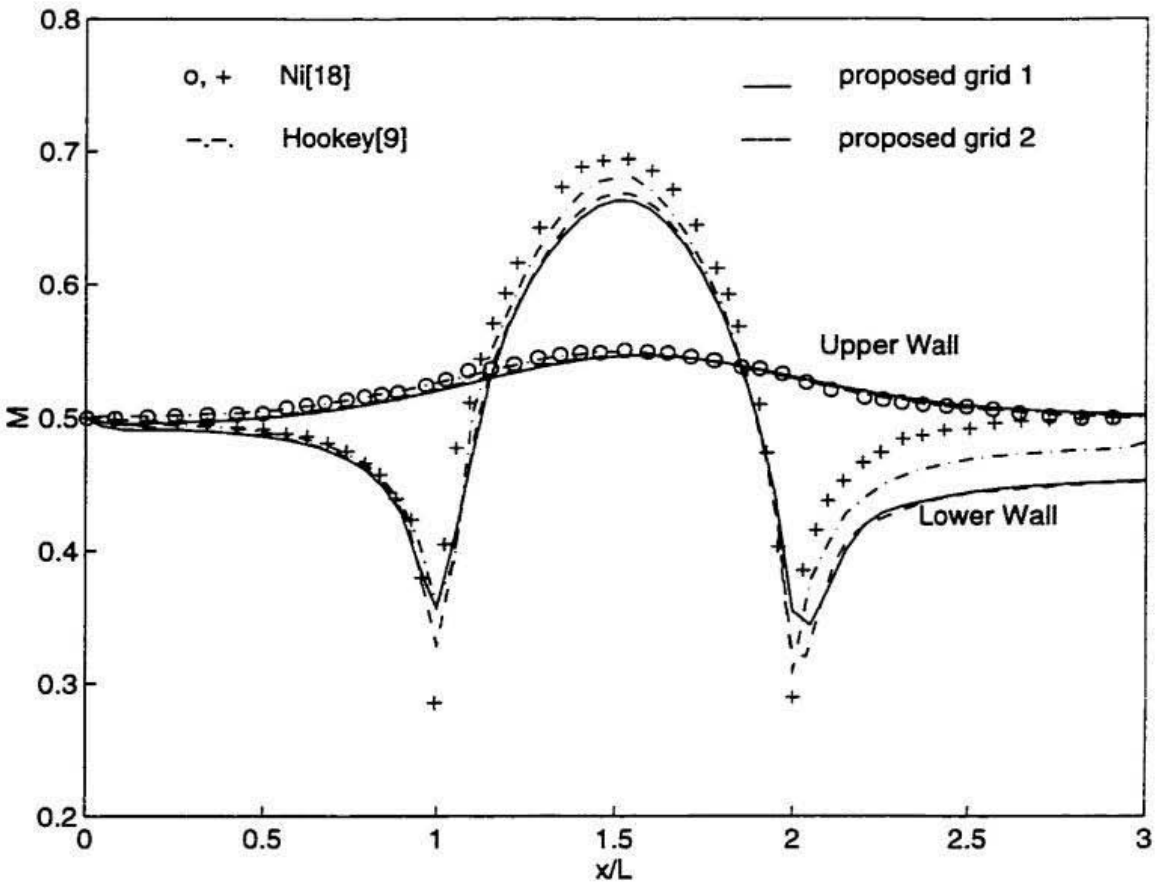

Figure 4.7: Subsonic inviscid flow through a channel with a circular arc bump: distribution of Mach number on the upper and lower walls of the channel.

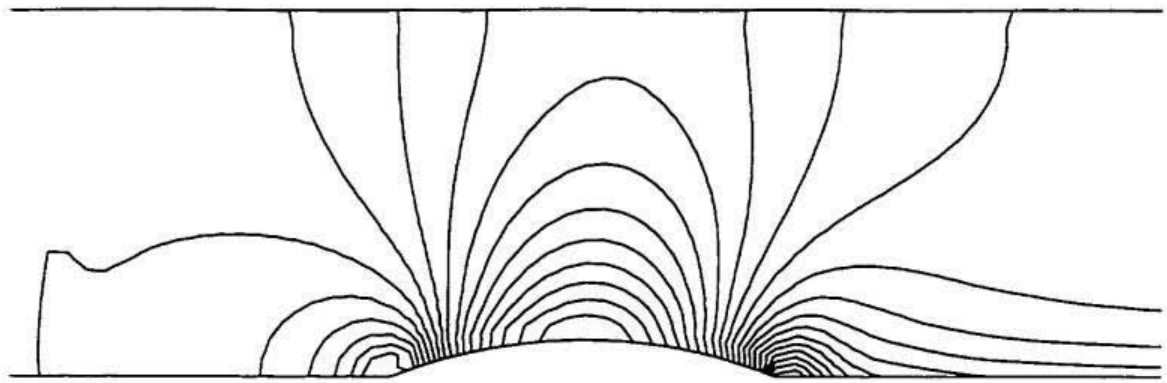

(a)

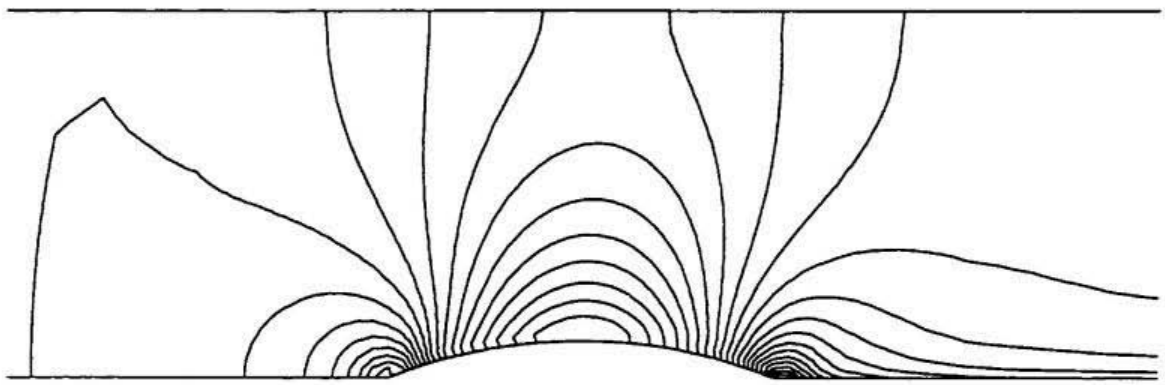

(b)

Figure 4.8: Subsonic inviscid flow through a channel with a circular arc bump: isoMach lines generated on (a) grid 1, and (b) grid 2.

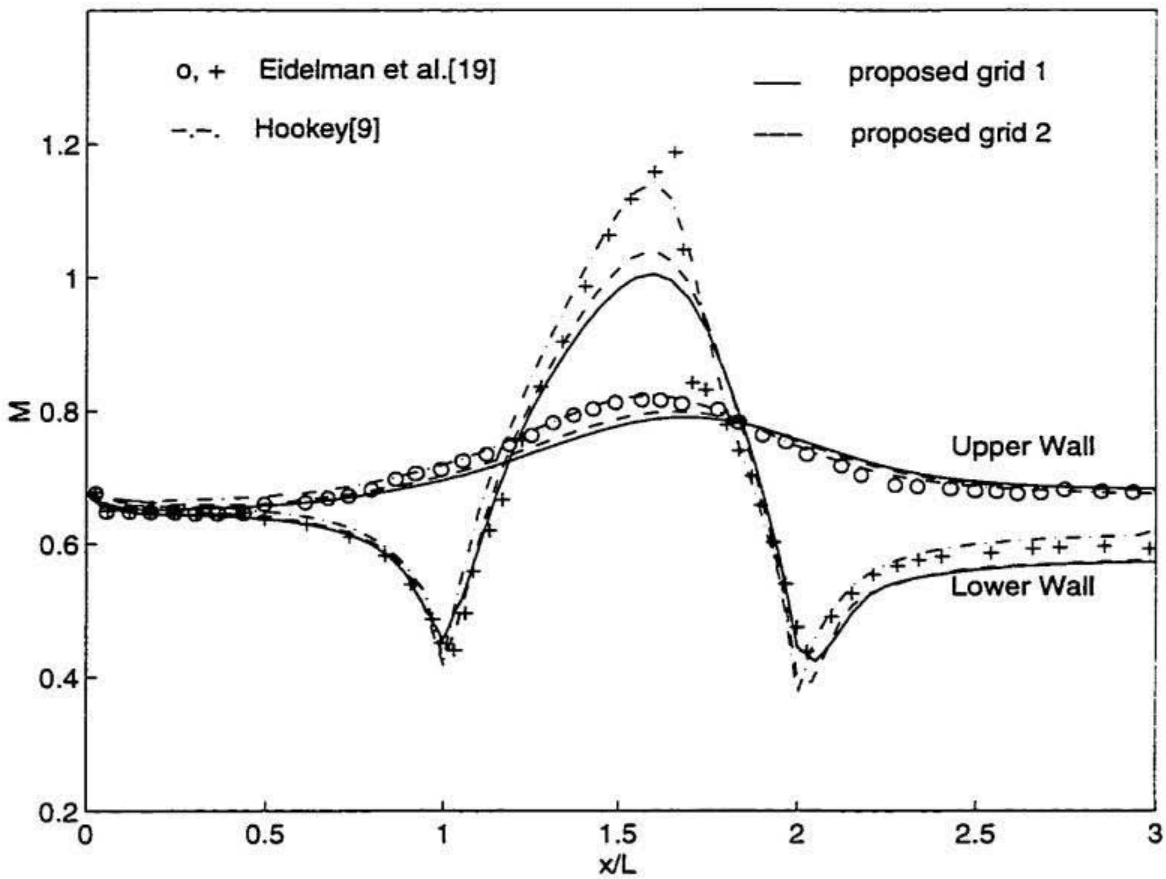

Figure 4.9: Transonic inviscid flow through a channel with a circular arc bump: distribution of Mach number on the upper and lower walls of the channel.

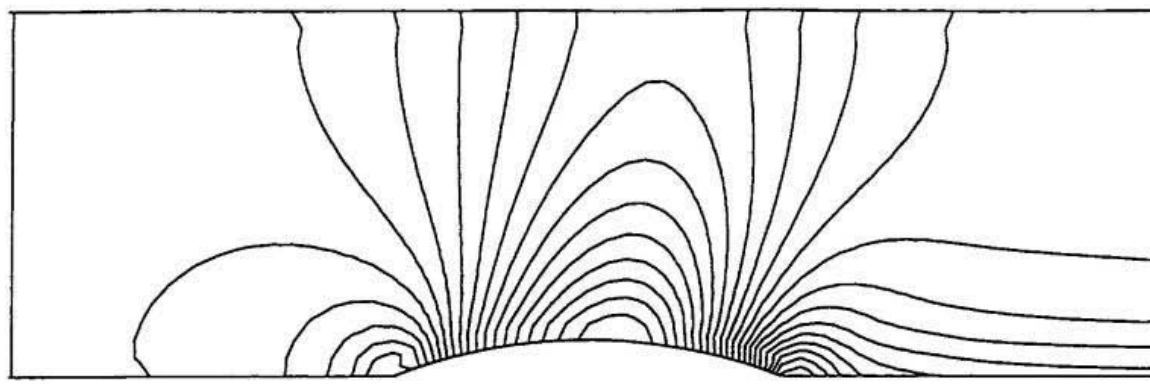

(a)

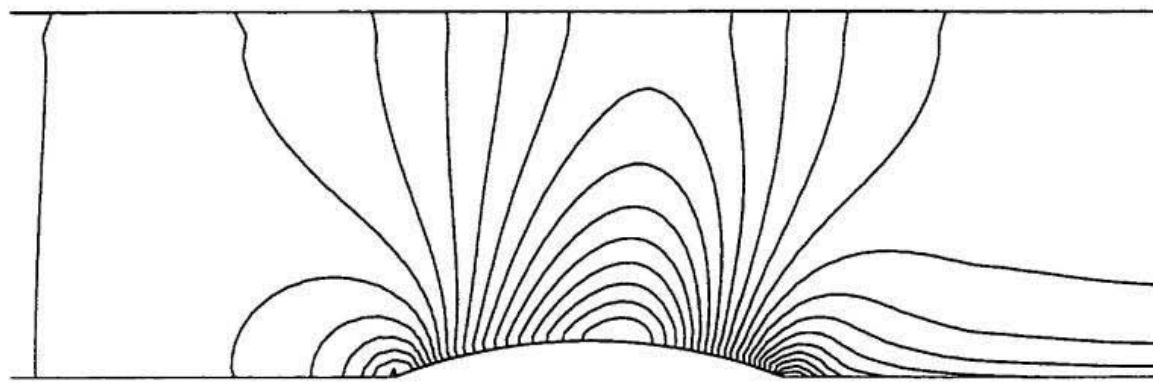

(b)

Figure 4.10: Transonic inviscid flow through a channel with a circular arc bump: isoMach lines generated on (a) grid 1, and (b) grid 2.

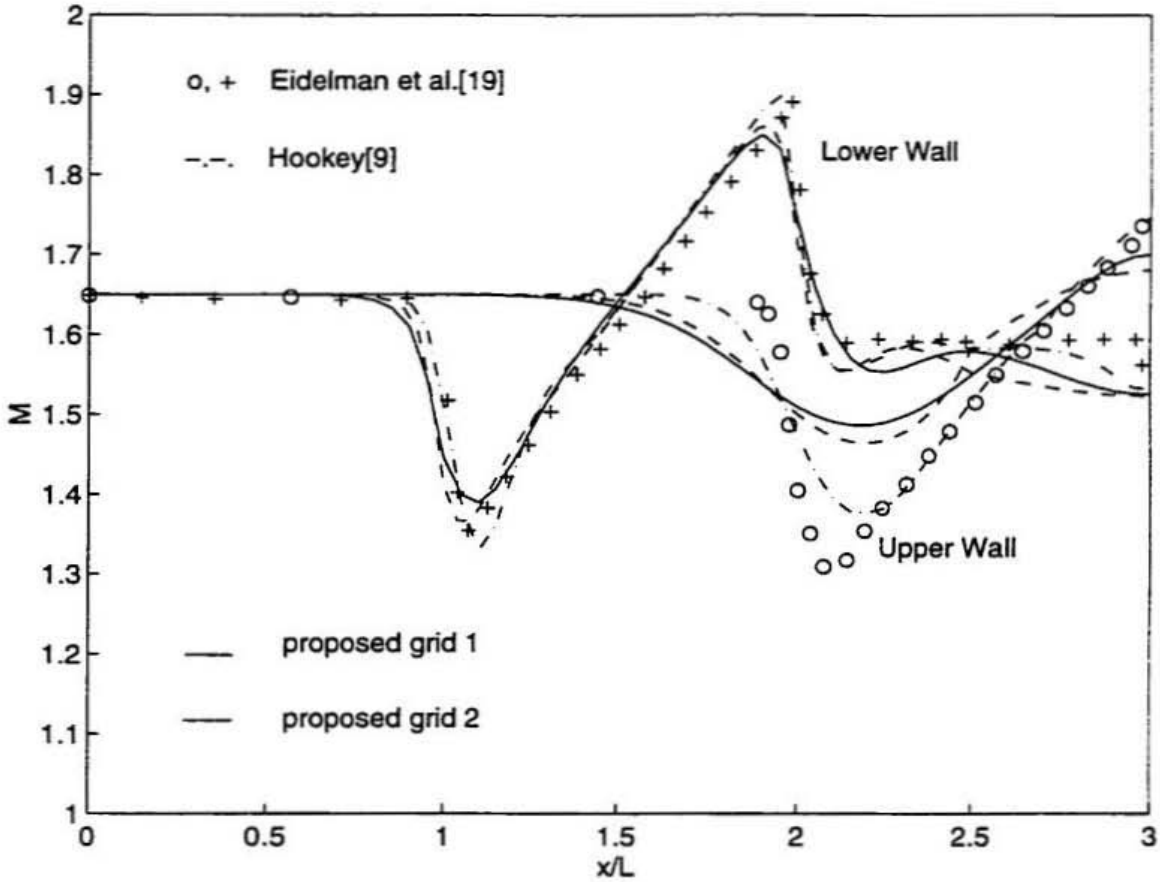

Figure 4.11: Supersonic inviscid flow through a channel with a circular arc bump: distribution of Mach number on the upper and lower walls of the channel.

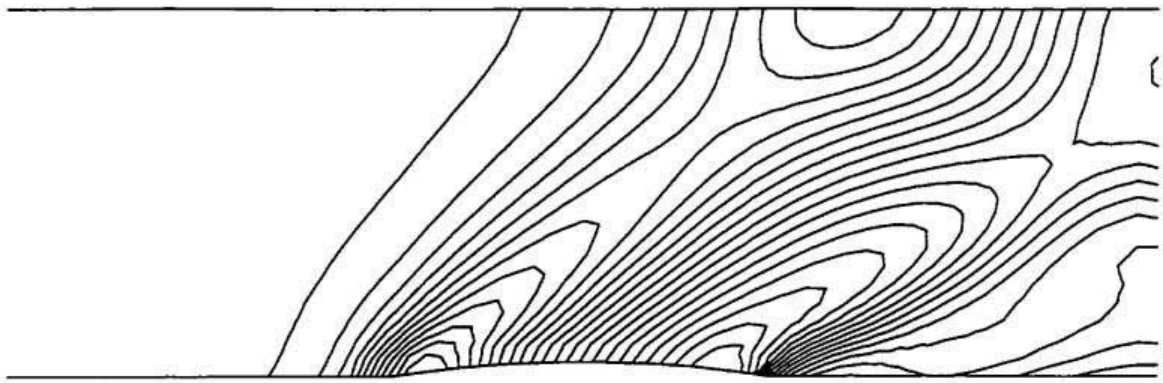

(a)

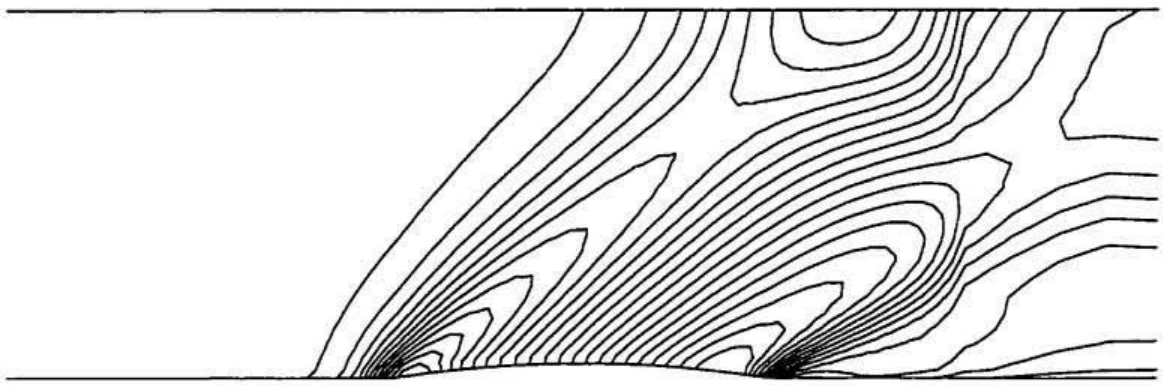

(b)

Figure 4.12: Supersonic inviscid flow through a channel with a circular arc bump: isoMach lines generated on (a) grid 1, and (b) grid 2.

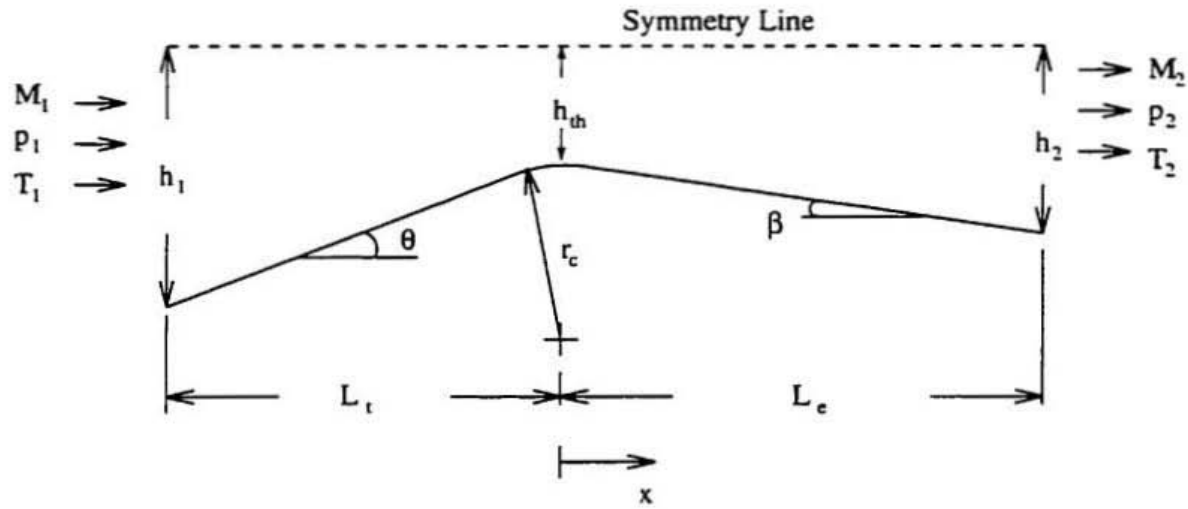

Figure 4.13: Inviscid flow through a planar converging-diverging nozzle: problem schematic.

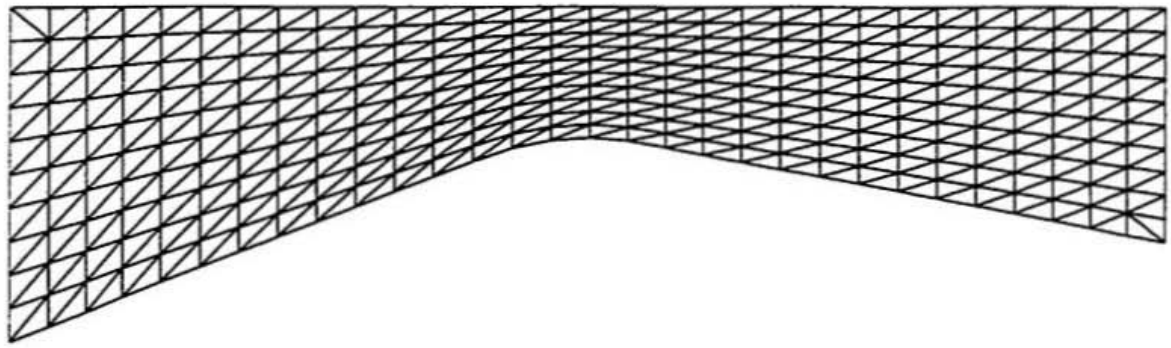

(a)

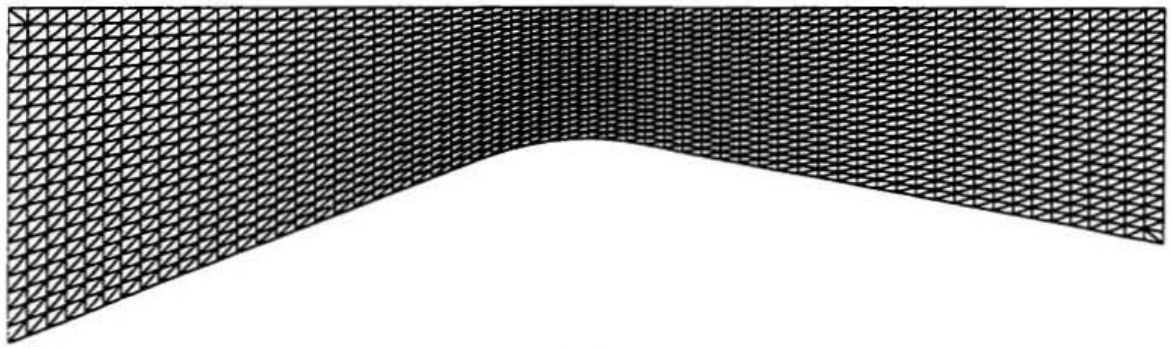

(b)

Figure 4.14: Inviscid flow through a planar converging-diverging nozzle: (a) 31×11 node grid, and (b) 61×21 node grid.

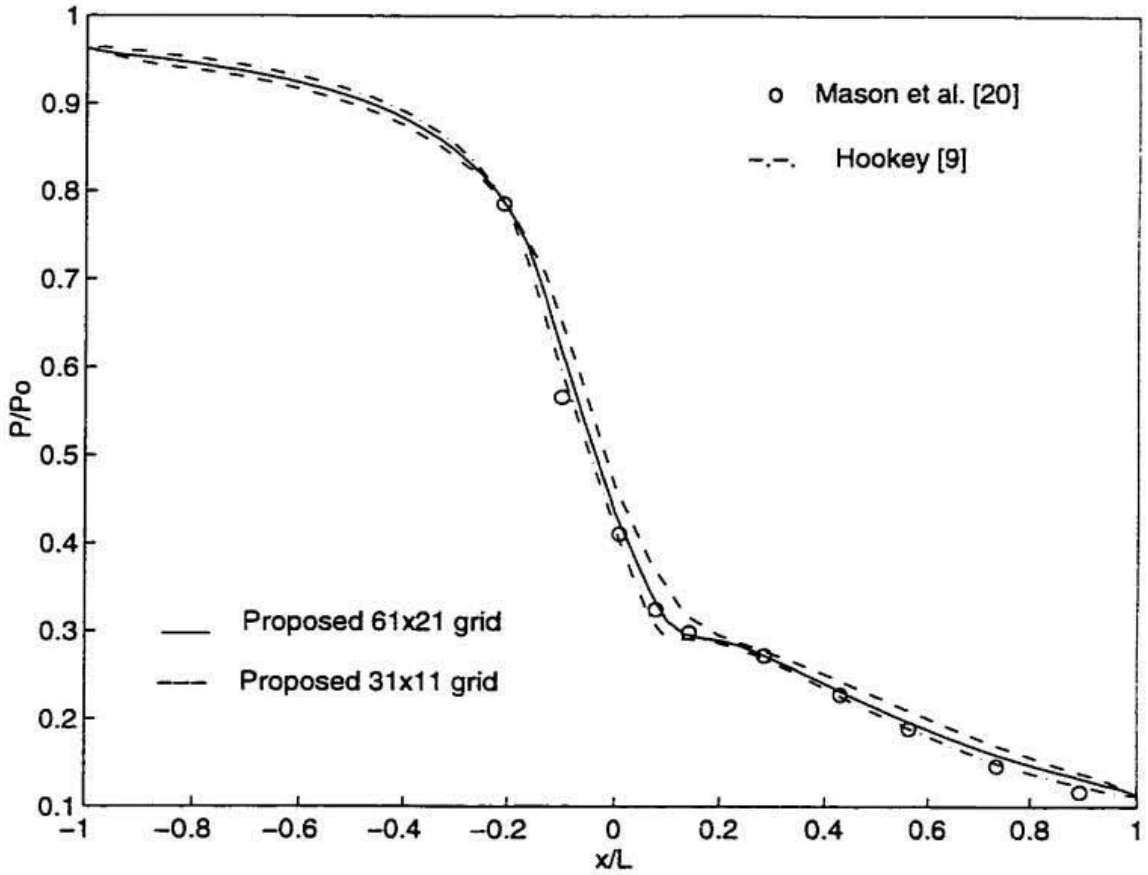

Figure 4.15: Inviscid flow through a planar converging-diverging nozzle: distribution of static to stagnation pressure ratio, p/p_0, along the lower wall of the nozzle.

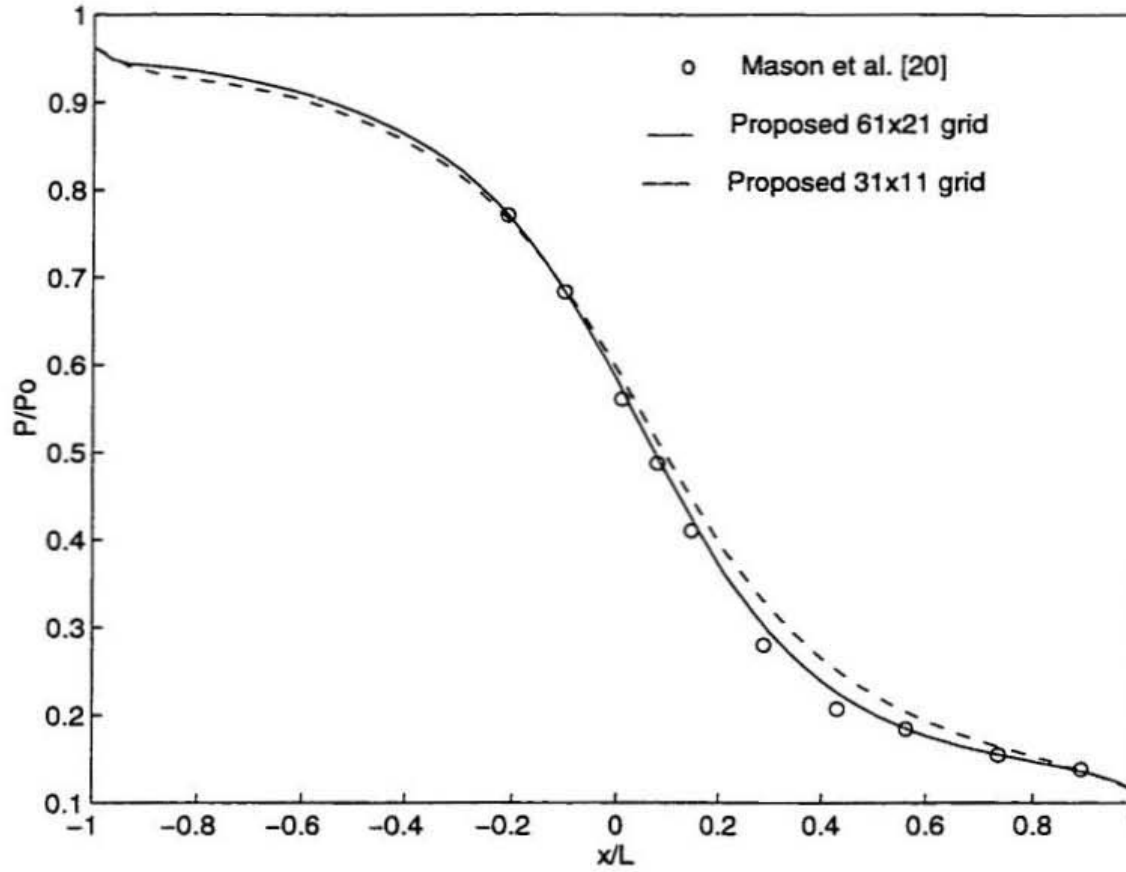

Figure 4.16: Inviscid flow through a planar converging-diverging nozzle: distribution of static to stagnation pressure ratio, p/p_0, along the symmetry plane of the nozzle.

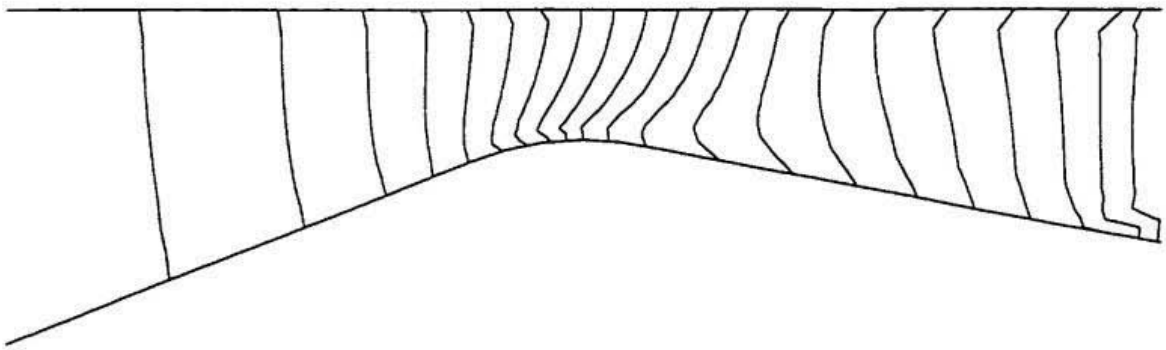

(a)

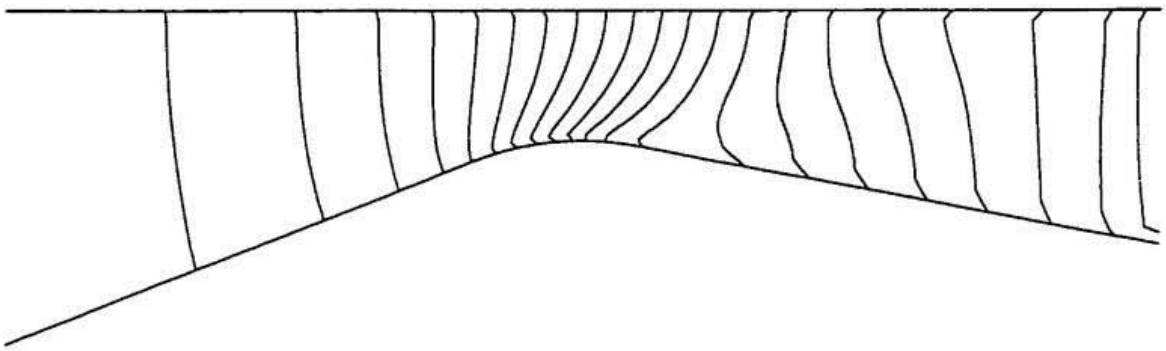

(b)

Figure 4.17: Inviscid flow through a planar converging-diverging nozzle: isoMach lines generated on (a) 31×11 node grid, and (b) 61×21 node grid.

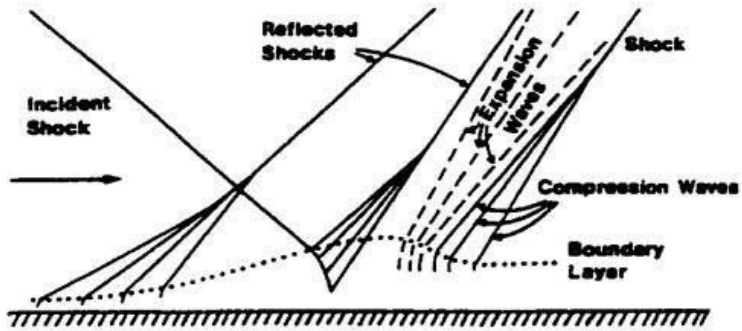

Figure 4.18: Schematic representation of the interaction of an incident shock with a laminar boundary layer [9].

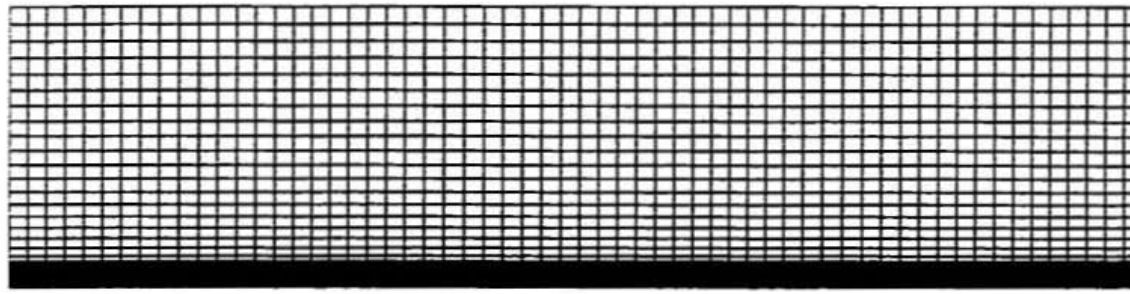

(a)

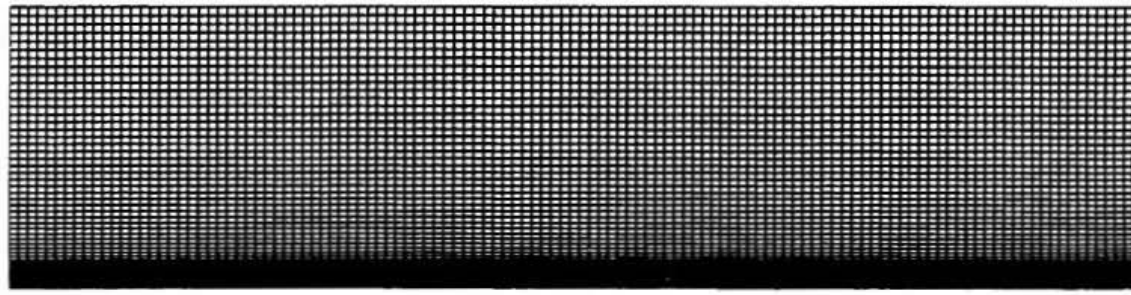

(b)

Figure 4.19: Shock-laminar boundary layer interaction: (a) 61×41 node grid; and (b) 121×81 node grid.

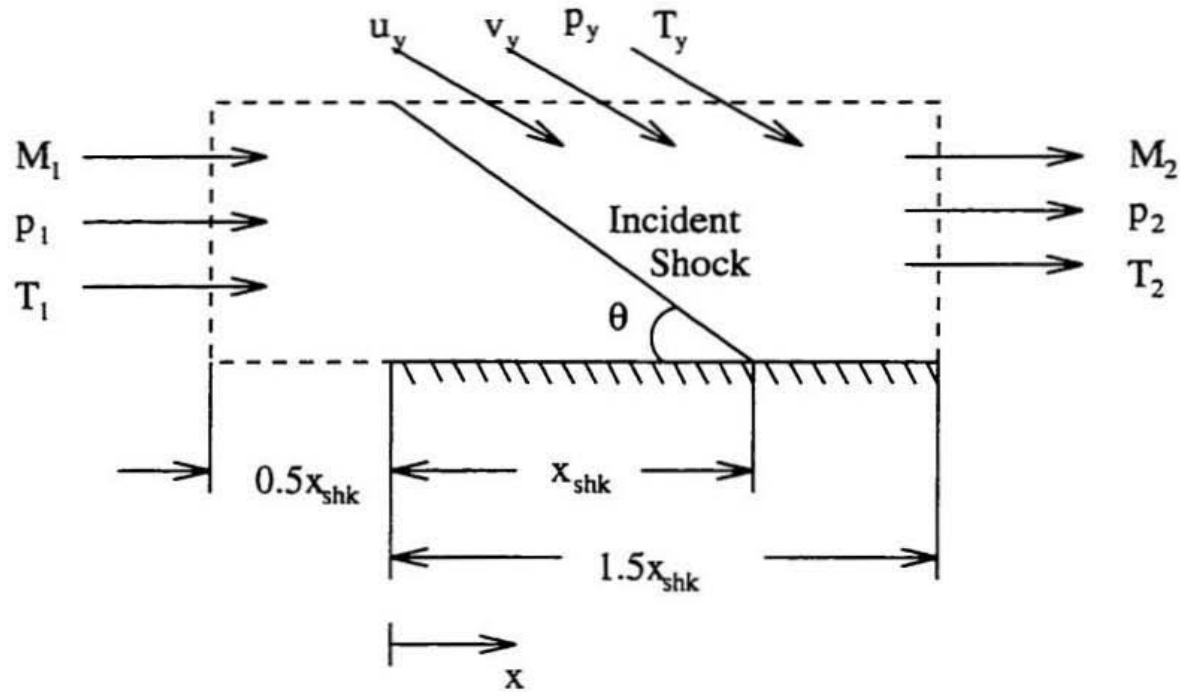

Figure 4.20: Shock-laminar boundary layer interaction: problem schematic.

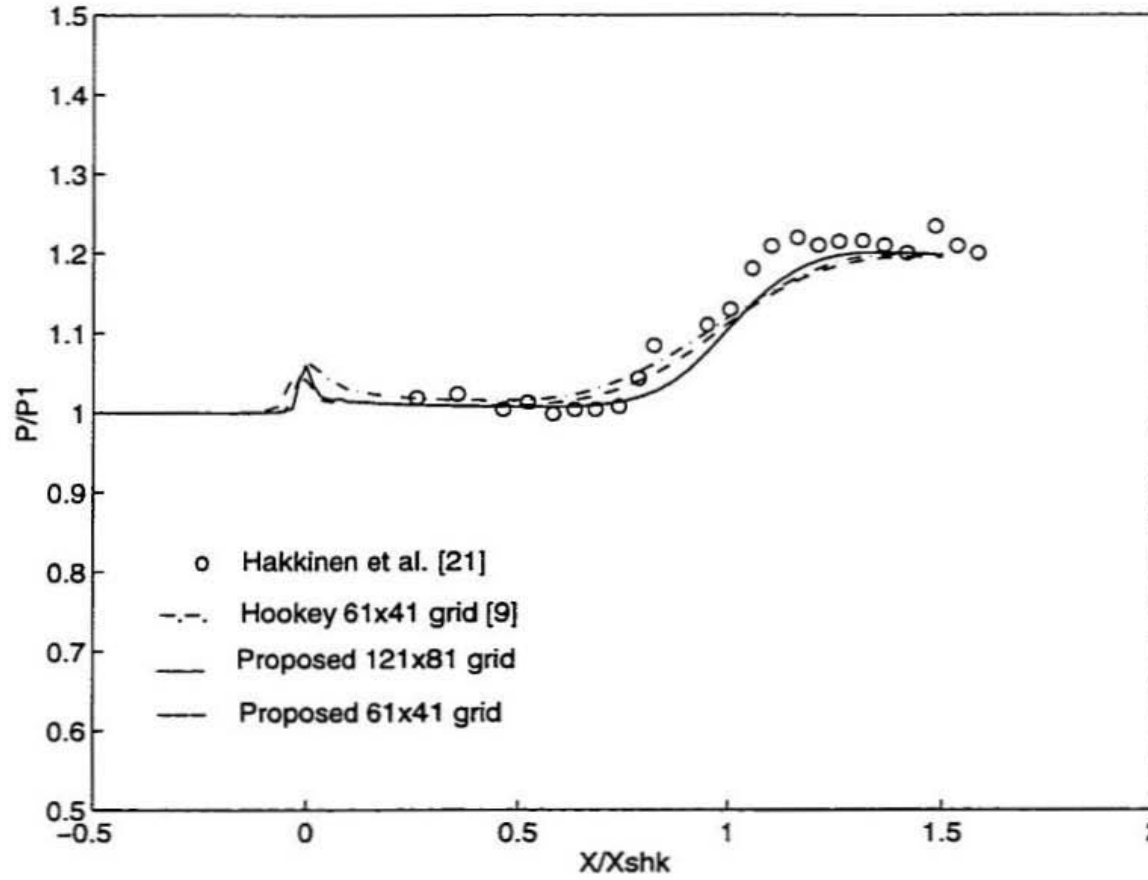

Figure 4.21: Shock-laminar boundary layer interaction: variation of the static pressure ratio, p/p_1, along the surface of the flat plate.

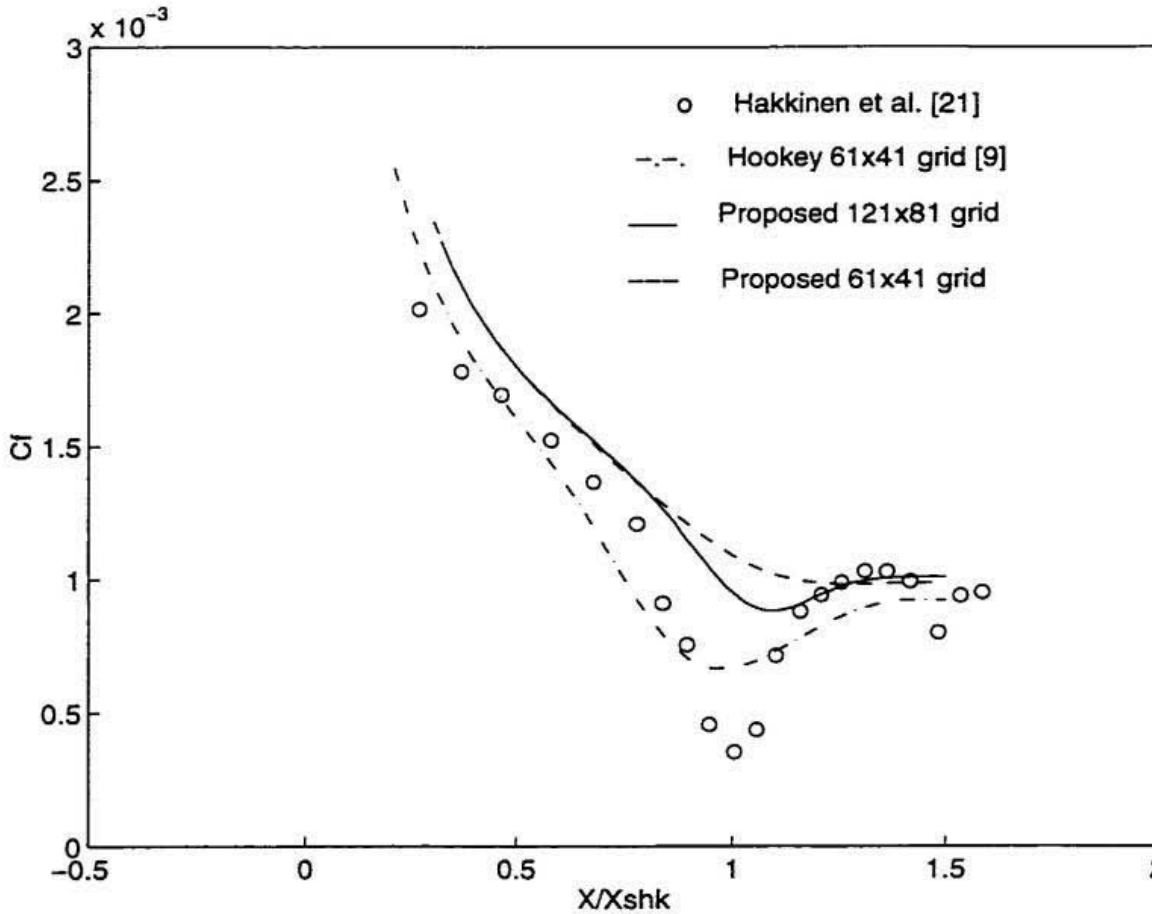

Figure 4.22: Shock-laminar boundary layer interaction: variation of the skin friction coefficient, c_f, along the surface of the flat plate.

Chapter 5

Conclusion

5.1 Contributions Of The Thesis

The formulation and implementation of two colocated CVFEM's for steady, quasi-one- and two-dimensional, viscous compressible fluid flow problems have been reported in this thesis. The proposed CVFEM's automatically capture all shocks within the calculation domain: the change in flow conditions across a shock is smeared over several nodes, however, resulting in finite gradient approximations of the essentially discontinuous physical change in flow conditions across a shock.

The proposed CVFEM's were formulated to solve the continuity, Navier-Stokes, energy, and state equations for a perfect gas. These methods can account for variable fluid properties, such as dynamic viscosity and thermal conductivity, however, in order to keep the source terms in the energy equation relatively uncomplicated, the specific heat, c_p, was assumed constant. The so-called primitive variables, velocity components, pressure and temperature, were used as the dependent variable set in the formulation of the proposed CVFEM's.

The MAss Weighted (MAW) scheme of upwind interpolation, used in the interpolation of convective terms, was modified for its application in triangular elements with three control volume faces. A pseudo-velocity field was defined to incorporate

the pressure gradients in the interpolation of 'mass conserving' velocities to prevent the oscillatory solution fields that may arise with colocation of dependent variable storage locations [14].

The proposed CVFEM's were applied to several test problems, and the solutions generated were compared with theoretical, experimental, and numerical results available in the literature. The one-dimensional CVFEM generated solutions in very good agreement with theoretical solutions of quasi-one-dimensional inviscid flow problems. The shock capturing ability of the proposed method was demonstrated in the simulation of a flow through a converging-diverging nozzle with a shock in the divergent portion of the nozzle. The method was shown to be first-order accurate at the high element Reynolds numbers encountered in the flow problems solved.

The two-dimensional CVFEM was used to solve four inviscid and one viscous flow problems. The results generated by the proposed CVFEM did not compare favourably with other numerical simulations. In particular, the low (first) order interpolation implicit in the MAW scheme was responsible for poor prediction of shock strength and position, and pressure recovery. This would indicate that the higher-order interpolation used by Hookey [9] or another higher-order interpolation scheme should be employed to improve the accuracy of the CVFEM prediction.

5.2 Proposed Extensions Of This Work

The proposed formulation provided a simpler implementation to the method proposed by Hookey [9], and the use of 'mass conserving' velocities helped to eliminate some convergence difficulties inherent to that method when it was applied to the solution of flow problems with fluids of constant densities. The MAW interpolation was found to be unsatisfatory for compressible flow problems. Future work

should concentrate on the implementation and evaluation of higher-order interpolation functions, in concert with the use of mass-conserving velocities, to develop a method that is at least as accurate as that in [9] but simpler to implement, and more stable.

References

[1] Baliga, B.R. and Patankar, S.V., "A New Finite-Element Formulation for Convection-Diffusion Problems", *Numer. Heat Transfer*, vol. 3, pp. 393-409, 1980.

[2] Baliga, B.R. and Patankar, S.V., "A Control Volume Finite-Element Method for Two-Dimensional Fluid Flow and Heat Transfer", *Numer. Heat Transfer*, vol. 6, pp. 245-261, 1983.

[3] Prakash, C. and Patankar, S.V., "A Control Volume-Based Finite-Element Method for Solving the Navier-Stokes Equations Using Equal-Order Velocity-Pressure Interpolation", *Numer. Heat Transfer*, vol.8, pp. 259-280, 1985.

[4] Prakash, C., "Examination of the Upwind (Donor-Cell) Formulation in Control Volume Finite-Element Methods for Fluid Flow and Heat Transfer", *Numer. Heat Transfer*, vol.11, pp. 401-416, 1987.

[5] Prakash, C., "An Improved Control Volume Finite-Element Method for Heat and Mass Transfer, and for Fluid Flow Using Equal-Order Velocity-Pressure Interpolation", *Numer. Heat Transfer*, vol.9, pp. 253-276, 1986.

[6] Hookey, N.A., "Evaluation and Enhancements of Control Volume Finite-Element Methods for Two-Dimensional Fluid Flow and Heat Transfer", M.Eng. thesis, McGill Univ., Montreal, Canada, 1986.

[7] Hookey, N.A., Baliga, B.R. and Prakash, C., "Evaluation and Enhancements of Some Control Volume Finite-Element Methods - Part 1. Convection-Diffusion Problems", *Numer. Heat Transfer*, vol.14, pp. 255-272, 1988.

[8] Hookey, N.A., Baliga, B.R., "Evaluation and Enhancements of Some Control Volume Finite-Element Methods - Part 2. Incompressible Fluid Flow Problems", *Numer. Heat Transfer*, vol. 14, pp. 273-293, 1988.

[9] Hookey, N.A., "A Control Volume Finite-Element Method for Steady Two-Dimensional Viscous Compressible Flows", Ph.D. thesis, McGill Univ., Montreal, Canada, 1989.

[10] Saabas, H.J. "A Control Volume Finite Element Method for Three-Dimensional, Incompressible Viscous Fluid Flow", Ph.D. thesis, McGill Univ., Montreal, Canada.

[11] Schneider, G.E. and Raw, M.J., "A Skewed Positive Influence Coefficient Upwinding Procedure for Control-Volume-Based Finite-Element Convection-Diffusion", *Numer. Heat Transfer*, vol.9, pp. 1-26, 1986.

[12] Schneider, G.E. and Raw, M.J., "Control Volume Finite-Element Method for Heat Transfer and Fluid Flow Using Colocated Variables -1. Comutational Procedure", *Numer. Heat Transfer*, vol.11, pp. 363-390, 1987.

[13] Schneider, G.E. and Raw, M.J., "Control Volume Finite-Element Method for Heat Transfer and Fluid Flow Using Colocated Variables - 2. Application and Validation", *Numer. Heat Transfer*, vol.11, pp. 391-400, 1987.

[14] Patankar, S.V., *Numerical Heat Transfer and Fluid Flow*, Hemisphere, Washington, D.C., 1980.

[15] LeDain-Muir, B., "A Control Volume Finite-Element Method for Three-Dimensional Elliptic Fluid Flow and Heat Transfer", M.Eng. thesis, McGill Univ., Montreal, Canada, 1983.

[16] Shapiro, A.H., *The Dynamics and Thermodynamics of Compressible Fluid Flow*, vol.1, Wiley, New York, 1953.

[17] Shapiro, A.H., *The Dynamics and Thermodynamics of Compressible Fluid Flow*, vol.2, Wiley, New York, 1953.

[18] Ni, R.-H., *A Multiple-Grid Scheme for Solving the Euler Equations*, vol.2, Robert E. Krieger Publ. Co., Florida, 1985.

[19] Eidelman, S., Colella, P. and Shreeve, R.P., "Application of the Godunov Method and its Second-Order Extension to Cascade Flow Modeling", *AIAA J.*, vol.22, pp. 1609-1615, 1984.

[20] Mason, M.L., Putnam, L.E. and Re, R.J., "The Effect of Throat Contouring on Two-Dimensional Converging-Diverging Nozzles at Static Conditions", *NASA TP-1704*, 1980.

[21] Hakkinen, R.J., Breber, I., Trilling, L. and Abarbanel, S.S., "The Interaction of an Oblique Shock Wave with a Laminar Boundary Layer". *NASA Memo 2-18-59W*, 1959.

[22] Baliga, B.R., Patankar, S.V., "Elliptic System: Finite Element Method II", in Minkowyez, W.J., Sparrow, E.M., Schneider, G.E., and Pletcher, R.H. (eds), *Handbook of Numerical Heat Transfer*, Chap. 11, pp. 421-461, Wiley, New York, 1988.

[23] Thompson, J.F., Warsi, Z.U.A. and Mastin, C.W., *Numerical Grid Generation Foundations and Applications*, Elsevier Science Publ. Co., New York, 1985.

[24] Thompson, J.F., "Grid Generation", in Mindowycz, W.J., Sparrow, E.M., Schneider, G.E. and Pletcher, R.H. (eds.), *Handbook of Numerical Heat Transfer*, Chap. 21, pp.905-947, Wiley, New York, 1988.

[25] White, F.M., *Viscous Fluid Flow*, McGraw-Hill Book Co. Ltd., New York, 1974.

[26] MacCormack, R.W., "An Efficient Explicit-Implicit-Characteristic Method for Solving the Compressible Navier-Stokes Equations", in Keller, H.B. (ed.), *Computational Fluid Dynamics: SIAM-AMS Proceedings*, vol.11, pp.130-155, American Mathematical Society, Rhode Island, 1978.

[27] MacCormack, R.W. and Baldwin, B.S., "A Numerical Method for Solving the Navier-Stokes Equations with Application to Shock-Boundary Layer Interactions", *AIAA Paper no. 75-1*, 1975.

[28] Galpin,P.F., Huget,R.G., Raithby,G.D., 'Fluid Flow Simulations in Complex Geometries', CNS/ANS Second Int. Conf. on Simulation Methods in Nuclear Engineering, Montreal, Oct., 1986.

[29] Van Doormaal,J.P., A.,Raithby,G.D., 'Evaluation of New Techniques for the Calculation of Internal Recirculating Flows', *paper AIAA-87-0059*, AIAA 25th Aerospace Sciences Meeting, Jan.12-15, 1987, Reno, Nevada.

[30] Dale A. Anderson, John C. Tannehill, Richard H. Pletcher, *Computational Fluid Mechanics and Heat Transfer*, McGraw-Hill Book Co. Ltd., New York, 1984.

Appendix A

Interpolation Functions for the Proposed One-Dimensional CVFEM

A.1 Interpolation of Pressure

In the proposed one-dimensional CVFEM, the pressure is interpolated linearly within an element:

$$p = a_p x + b_p \tag{A.1}$$

Substitution of the nodal values:

$$\begin{aligned} p &= p_1 \quad \text{at} \quad x = x_1 \\ p &= p_2 \quad \text{at} \quad x = x_2 \end{aligned} \tag{A.2}$$

into Eq. (A.1), and solving for a_p and b_p gives:

$$a_p = \frac{p_1 - p_2}{x_1 - x_2} \tag{A.3}$$

$$b_p = \frac{-p_1 x_2 + p_2 x_1}{x_1 - x_2} \tag{A.4}$$

The pressure gradient, dp/dx, is given by Eq. (A.3).

A.2 Interpolation of Area

In the proposed CVFEM, the variable area of a duct, w, is interpolated linearly within an element:

$$w = a_w x + b_w \tag{A.5}$$

where a_w and b_w are defined by similar expressions to Eqs. (A.3) and (A.4), for a_p and b_p.

A.3 Interpolation of Velocity

The mass weighted (MAW) interpolation scheme is used in the proposed CVFEM. in which upwind interpolation is used to interpolate velocity and temperature when they are convected scalars, and linear interpolation is used for velocity and temperature in diffusion terms. Linear interpolation is also used for the mass conserving velocities.

A.3.1 Interpolation of a Convected Scalar

In the one-dimensional case, the MAW interpolation reduces to a pure upwind scheme. Defining i and $i+1$ as two nodes of an element, and o as the CV face, the upwind scheme can be expressed as follows:

$$\begin{aligned} &\text{if} \quad u_i > 0, \quad u_o = u_i \\ &\text{if} \quad u_i < 0, \quad u_o = u_{i+1} \end{aligned} \tag{A.6}$$

This scheme is also applied to temperature by replacing u by T in Eq. (A.6).

A.3.2 Interpolation of a Diffused Scalar

Velocity is interpolated linearly in diffusion terms. and other terms where a gradient of velocity is required:

$$u = a_u x + b_u \tag{A.7}$$

where the coefficients a_u and b_u are evaluated in a similar manner to a_p and b_p in Eqs. (A.3) and (A.4). Temperature is also interpolated by a similar linear function in diffusion terms.

A.3.3 Interpolation of Mass Conserving Velocity

The mass conserving velocity is interpolated by linear interpolation of a pseudo velocity, $\hat{u}$, and a pressure coefficient, d^u. If the CV face is placed midway between

the nodes of an element, the mass conserving velocity at control volume face, u_o^m, can be written as follows:

$$u_o^m = \frac{\hat{u}_i + \hat{u}_{i+1}}{2} + \frac{d_i^u + d_{i+1}^u}{2}\frac{dp}{dx} \tag{A.8}$$

where, dp/dx is evaluated using Eq. (A.3).

A.4 Interpolation of Density

In the proposed CVFEM, the density is interpolated by an equation of state written in terms of a linear function of pressure. In this thesis, the equation of state for an ideal gas is used:

$$\rho = \frac{p}{RT} \tag{A.9}$$

The interpolated density is upwinded by upwinding both the pressure and temperature that appear in Eq. (A.9). It should be noted that pressure is upwinded **only** when it is being used to interpolated density: in all other terms pressure is interpolated linearly.

Appendix B

Integration of Fluxes in the Proposed One-Dimensional CVFEM

B.1 Introduction

In Chapter 2, the governing equations for steady, quasi-one-dimensional, viscous compressible flow through a duct of variable area, w, were written in the following conservative forms:

$$\frac{dJ}{dx} = Sw \tag{B.1}$$

$$\frac{dg}{dx} = 0 \tag{B.2}$$

where, J is the combined convection-diffusion transport, S is the source term, and g is the mass flow, ρwu. Equation (B.1) represents the momentum equation when:

$$J = \rho wuu - \mu w\frac{du}{dx} \quad ; \quad S = S^u - \frac{dp}{dx} + \frac{1}{3w}\frac{d}{dx}\left(\mu\frac{d}{dx}(uw)\right) \tag{B.3}$$

the energy equation when:

$$J = \rho wuT - \frac{k}{c_p}w\frac{dT}{dx} \quad ; \quad S = S_T = \frac{S^T}{c_p} + \frac{u}{c_p}\frac{dp}{dx} \tag{B.4}$$

Applying the appropriate conservation principle to a control volume V, which is fixed in space, integral forms of Eqs. (B.1) and (B.2) can be obtained:

$$\int_{\partial V}\frac{dJ}{dx}\,dx = \int_V Sw\,dx \tag{B.5}$$

$$\int_{\partial V} \frac{dg}{dx}\, dx \;=\; 0 \tag{B.6}$$

where ∂V is the surface of the control volume, and V is the volume of the control volume.

With reference to the control volume constructed around node i in Fig. 2.1, Eqs. (B.5) and (B.6) are cast in the following forms in Chapter 2:

$$J_0 - \int_V Sw\, dx \;+\; \left(\begin{array}{l}\text{Similar contributions from other}\\ \text{elements associated with node i}\end{array}\right) + \left(\begin{array}{l}\text{Boundary contributions,}\\ \text{if applicable}\end{array}\right) = 0 \tag{B.7}$$

$$g_0 \;+\; \left(\begin{array}{l}\text{Similar contributions from other}\\ \text{elements associated with node i}\end{array}\right) + \left(\begin{array}{l}\text{Boundary contributions,}\\ \text{if applicable}\end{array}\right) = 0 \tag{B.8}$$

To derive the element contributions to the discretized forms of the integral conservation equations, the integrated fluxes across the control volume face in each element must be evaluated. The algebraic approximation of these terms is described in the following three sections: first the combined convection-diffusion transport terms in the momentum equation are considered; then the integrated flux of energy is described; and finally the approximation of the mass flow across the control volume face is derived. All nomenclature used in this Appendix refers to that shown in Fig. 2.1. The complete assembly of the discretized forms of the governing equations will be discussed in Appendix C.

B.2 Momentum Equation

In the proposed one-dimensional CVFEM, the convected velocity term is upwinded. The diffused velocity, which occurs in the $\mu w du/dx$ term, and velocity gradients that appear in the viscous terms, and the source term are evaluated using linear interpolation. The following derivations are based on the assumption of flow in the positive x-direction, as shown in Fig. 2.1.

Using upwinding, Eq. (A.6), in the convection term, and linear interpolation, Eq. (A.7) in the diffusion terms, the interpolated convection-diffusion flux of x-

momentum at a control volume face, J_0^u, can be written as follows:

$$J_0 = \left((\rho w u)_0 + \frac{\mu w_0}{x_2 - x_1}\right) u_1 - \frac{\mu w_0}{x_2 - x_1} u_2 \tag{B.9}$$

where $w_0 = (w_1 + w_2)/2$, and $(\rho w u)_0$, is interpolated linearly from available values.

Rearranging J_0^u in terms of nodal velocities gives the following:

$$J_0 = c_1 u_1 + c_2 u_2 \tag{B.10}$$

where

$$c_1 = (\rho w u)_0 + \frac{\mu w_0}{x_2 - x_1} \quad ; \quad c_2 = -\frac{\mu w_0}{x_2 - x_1} \tag{B.11}$$

The integral of the source term, S, over the portion of the control volume (cv) about node 1 which is contributed by element 1-2 (see Fig. 2.1) is written as follows:

$$\int_{vol_1} S_u \, dx = S_c^u vol_1 + d_{11} u_1 + d_{12} u_2 + vol_1 \frac{dp}{dx} \tag{B.12}$$

where

$$d_{11} = S_p^u vol_1 - \mu \frac{5w_1 - 3w_0}{6(x_2 - x_1)} \tag{B.13}$$

$$d_{12} = \mu \frac{5w_1 - 3w_0}{6(x_2 - x_1)} \tag{B.14}$$

Element 1-2 also makes a contribution to the cv surrounding node 2. The integral of the source term, S_u, over this portion of the cv associated with node 2 is written as follows:

$$\int_{vol_2} S_u \, dx = S_c^u vol_2 + d_{21} u_1 + d_{22} u_2 + vol_2 \frac{dp}{dx} \tag{B.15}$$

where

$$d_{21} = \mu \frac{5w_0 - 3w_2}{6(x_2 - x_1)} \tag{B.16}$$

$$d_{22} = S_p^u vol_2 - \mu \frac{5w_0 - 3w_2}{6(x_2 - x_1)} \tag{B.17}$$

The volume terms, vol_1 and vol_2, in Eqs. (B.12) and (B.15), respectively, are defined as follows:

$$vol_1 = (w_1 + w_0)\Delta x/4 \quad ; \quad vol_2 = (w_2 + w_0)\Delta x/4 \tag{B.18}$$

and

$$w_0 = (w_1 + w_2)/2 \tag{B.19}$$

where linear interpolation has been used for the area, w, and Δx is the distance between the nodes.

B.3 Energy Equation

Temperature is interpolated in a similar manner to velocity, and the integration of the convection-diffusion flux over a cv face can be evaluated using the same procedure, and written in terms of the nodal temperatures as follows:

$$J_0 = C_1 T_1 + C_2 T_2 \tag{B.20}$$

where

$$C_1 = (\rho w u)_0 + \frac{k w_0}{c_p(x_2 - x_1)} \quad : \quad C_2 = -\frac{k w_0}{c_p(x_2 - x_1)} \tag{B.21}$$

The integration of the source term over the element 1-2 can be written in the following form:

$$\begin{aligned} \int_{vol} S_T w dx &= \frac{1}{c_p}\left(S_c^T + u_1 \frac{dp}{dx}\right) vol_1 + \frac{S_p^T}{c_p} T_1 vol_1 \\ &+ \frac{1}{c_p}\left(S_c^T + u_2 \frac{dp}{dx}\right) vol_2 + \frac{S_p^T}{c_p} T_2 vol_2 \end{aligned} \tag{B.22}$$

where, the pressure gradient is evaluated using Eq. (A.3) and vol_1 and vol_2 are defined in Eq. (B.18).

B.4 Continuity Equation

B.4.1 Introduction

In the proposed CVFEM, the mass flow rate across a control volume face, g_0, is linearized with respect to density and velocity:

$$g_0 = \tilde{g}_0 + \dot{g}_0 + \mathring{g}_0 \tag{B.23}$$

where $\tilde{g}$ is linearized with respect to velocity, $\dot{g}$ is linearized with respect to density, and $\mathring{g}$ is determined from available values of density and velocity. The algebraic approximation of the $\tilde{g}_0$, $\dot{g}_0$, and $\mathring{g}_0$ terms is described in the following subsections.

B.4.2 Algebraic Approximation of $\tilde{g}_0$

In the proposed CVFEM, the upwinded velocity is used to linearize the mass flow rate, and the mass conserving velocity formula is used to calculate this upwinded

velocity:

$$\tilde{g}_0 = (\rho w)_0 \left(\hat{u}_1 - d_1^u \frac{p_2 - p_1}{x_2 - x_1} \right) \tag{B.24}$$

where ρ_0 is interpolated linearly using available pressure and temperature values in the equation of state. w_0 is defined in Eq. (B.19). This equation may be written as follows:

$$\tilde{g}_0 = \frac{(\rho w)_0 \, d_1^u}{x_2 - x_1} \, p_1 - \frac{(\rho w)_0 \, d_1^u}{x_2 - x_1} \, p_2 + (\rho w)_0 \, \hat{u}_1 \tag{B.25}$$

B.4.3 Algebraic Approximation of $\dot{g}_0$

The linearization with respect to ρ_0 is performed by upwinding the density through upwinding both the pressure and temperature in the equation of state. Writing this expression in terms of pressure gives the following:

$$\dot{g}_0 = \frac{w_0 u_0}{R T_1} \, p_1 \tag{B.26}$$

where u_0 is calculated linearly from the nodal values of mass conserving velocity.

B.4.4 Algebraic Approximation of $\mathring{g}_0$

The $\mathring{g}_0$ term is calculated using available values of ρ, w, and mass conserving velocity u_0^m.

B.4.5 Complete Algebraic Approximation of the Linearized Mass Flow

Using the results from the last three subsections, the complete approximation of the linearized mass flow can be written in terms of p_1 and p_2 as follows:

$$\begin{aligned} g_0 &= \tilde{g}_0 + \dot{g}_0 + \mathring{g}_0 \\ &= E_1 \, p_1 + E_2 \, p_2 + B_0 \end{aligned} \tag{B.27}$$

where

$$E_1 = \frac{(\rho w)_0 \, d_1^u}{x_2 - x_1} + \frac{w_0 \, u_0^m}{R T_1} \tag{B.28}$$

$$E_2 = -\frac{(\rho w)_0 \, d_1^u}{x_2 - x_1} \tag{B.29}$$

$$B_0 = (\rho w)_0 \, (\hat{u}_1 - u_0^m) \tag{B.30}$$

B.4.6 Outflow Boundary Condition for the Continuity Equation

The outflow boundary condition in the continuity equation is treated differently than the outflow boundaries of the other equations due to the linearization of the mass flow rate. The mass outflow at boundary node i, g_i, is written as follows:

$$g_i = \tilde{g}_i + \dot{g}_i + \mathring{g}_i \tag{B.31}$$

where, $\tilde{g}_i$ is evaluated with the known density, and treating the mass conserving velocity as an unknown. Using the pseudo-velocity, $\tilde{u}_i$, and pressure coefficient, d_i^u, $\tilde{g}_i$ is written as follows:

$$\tilde{g}_i = \rho_i w_i \left(\tilde{u}_i - d_i^u \frac{p_i - p_{i-1}}{x_i - x_{i-1}} \right) \tag{B.32}$$

The $\dot{g}_i$ term is evaluated using the available mass conserving velocity, u_i^m, and unknown density, which is calculated using the equation of state:

$$\dot{g}_i = w_i u_i^m \frac{p_i}{RT_i} \tag{B.33}$$

The $\mathring{g}_i$ term is evaluated using the known nodal values of ρ_i and u_i^m:

$$\mathring{g}_i = \rho_i \, w_i \, u_i^m \tag{B.34}$$

The boundary outflow, g_i, can be written in terms of the nodal pressures p_i and p_{i-1}:

$$g_i = E_i^p \, p_i + E_{i-1}^p \, p_{i-1} + F_i^p \tag{B.35}$$

where,

$$E_i^p = \frac{w_i \, u_i^m}{RT_i} - \frac{\rho_i \, w_i \, d_i^u}{x_i - x_{i-1}} \tag{B.36}$$

$$E_{i-1}^p = \frac{\rho_i \, w_i \, d_i^u}{x_i - x_{i-1}} \tag{B.37}$$

$$F_i^p = \rho_i w_i \, (\tilde{u}_i - u_i^m) \tag{B.38}$$

Appendix C

Assembly of the Discretized Conservation Equations in the Proposed One-Dimensional CVFEM

C.1 Introduction

The methods used in the proposed one-dimensional CVFEM to approximate the integrated flux across the control volume face in an element, and the volume integration of the appropriate source terms, were presented in Appendix B. These integrated fluxes and source-related terms are used to compile the discretized forms of the integral conservation equations for a control volume. The compilation of the final forms of the discretized equations is presented in this Appendix. This discussion is separated into three sections devoted to the assembly of the momentum, energy, and continuity equations, respectively. All nomenclature refers to that shown in Fig. 2.1.

C.1.1 Assembly of the Momentum Equation

The integrated convection-diffusion flux across the control volume face in an element is approximated by the following expression in Appendix B:

$$J_0^u = c_1 u_1 + c_2 u_2 \tag{C.1}$$

The volume integration of the source term over an element is given by:

$$\int_{vol} S_u \, dx = S_c^u \, vol_1 + d_{11} u_1 + d_{12} u_2 + vol_1 \frac{dp}{dx}$$

$$+ S_c^u vol_2 + d_{21} u_1 + d_{22} u_2 + vol_2 \frac{dp}{dx} \qquad \text{(C.2)}$$

The assembly of the final discretized form of the momentum equation is done in an element-by-element manner. Visiting each element in turn, the coefficients in Eq. (C.1) and (C.2) are evaluated. These terms can be lumped into coefficients multiplying the appropriate dependent variable as follows:
For node (i):

$$A^c_{u(i)} = A^c_{u(i)} + c_1 - d_{11} \qquad \text{(C.3)}$$

$$A^e_{u(i)} = A^e_{u(i)} - c_2 + d_{12} \qquad \text{(C.4)}$$

$$A^{con}_{u(i)} = A^{con}_{u(i)} + S_c^u \, vol_1 - vol_1 \frac{dp}{dx} \qquad \text{(C.5)}$$

For node $(i+1)$:

$$A^c_{u(i+1)} = A^c_{u(i+1)} - c_2 - d_{22} \qquad \text{(C.6)}$$

$$A^w_{u(i+1)} = A^w_{u(i+1)} + c_1 + d_{21} \qquad \text{(C.7)}$$

$$A^{con}_{u(i+1)} = A^{con}_{u(i+1)} + S_c^u \, vol_2 - vol_2 \frac{dp}{dx} \qquad \text{(C.8)}$$

The coefficients appear on both sides of these equations, because contributions will also be made from another element, and previous contributions must be maintained. The contribution to the coefficient $A^c_{u(i)}$ is the portion of the net transport of momentum out of the control volume surrounding node i, associated with $u_{(i)}$, in the element $(i, i+1)$. The $A^e_{u(i)}$ coefficient is evaluated from the net transport of momentum into the control volume for node i. The volume integrated source-related terms, including the pressure gradient, are then added to the appropriate coefficient. A similar procedure is used to evaluate the coefficients at node $i+1$.

When the coefficients have been evaluated and assembled for every node in the calculation domain, the final form of the discretized momentum equation is written as follows:

$$A^c_{u(i)} \, u_{(i)} = A^e_{u(i)} \, u_{(i+1)} + A^w_{u(i)} \, u_{(i-1)} + A^{con}_{u(i)} \qquad \text{(C.9)}$$

This equation can be rewritten in the following convenient form:

$$a^u_i \, u_i = \sum_n a^u_n \, u_n + b^u_i \qquad \text{(C.10)}$$

where the summation is over the two neighbour nodes of node i, as shown in Fig. 2.1. This discretized form of the momentum equation involves three nodal velocities.

C.2 Assembly of the Energy Equation

In Appendix B the integrated convection-diffusion flux of energy across a control volume face is approximated by the following expression:

$$J_0^T = C_1 T_1 + C_2 T_2 \tag{C.11}$$

The volume integration of the source term over the element is written as follows:

$$\begin{aligned} \int_{vol} S_T w dx &= \frac{1}{c_p}\left(S_c^T + u_1 \frac{dp}{dx}\right) vol_1 + \frac{S_p^T}{c_p} T_1\, vol_1 \\ &+ \frac{1}{c_p}\left(S_c^T + u_2 \frac{dp}{dx}\right) vol_2 + \frac{S_p^T}{c_p} T_2\, vol_2 \end{aligned} \tag{C.12}$$

Equations (C.11) and (C.12) for the energy equation are similar to Eqs. (C.1) and (C.2) for the momentum equation, therefore, the discretized energy equation can be assembled in the same manner as the discretized momentum equation. A description of the assembly procedure will not be repeated, only the resulting coefficients are presented.

For node (i):

$$A^c_{T(i)} = A^c_{T(i)} + C_1 - \frac{S_p^T}{c_p} vol_1 \tag{C.13}$$

$$A^e_{T(i)} = A^e_{T(i)} - C_2 \tag{C.14}$$

$$A^{con}_{T(i)} = A^{con}_{T(i)} + \frac{1}{c_p}\left(S_c^T\, vol_1 + u_{(i)}\, vol_1 \frac{dp}{dx}\right) \tag{C.15}$$

For node $(i+1)$:

$$A^c_{T(i+1)} = A^c_{T(i+1)} - C_2 - \frac{S_p^T}{c_p} vol_2 \tag{C.16}$$

$$A^w_{T(i+1)} = A^w_{T(i+1)} + C_1 \tag{C.17}$$

$$A^{con}_{T(i+1)} = A^{con}_{T(i+1)} + \frac{1}{c_p}\left(S_c^T\, vol_2 + u_{(i+1)}\, vol_2 \frac{dp}{dx}\right) \tag{C.18}$$

When these coefficients have been assembled for every element in a calculation domain, the final form of the discretized energy equation for each node is obtained:

$$A^c_{T(i)}\, T_{(i)} = A^e_{T(i)}\, T_{(i+1)} + A^w_{T(i)}\, T_{(i-1)} + A^{con}_{T(i)} \tag{C.19}$$

This equation may be rewritten in the following compact form:

$$a_i^T T_i = \sum_n a_n^T T_n + b_i^T \tag{C.20}$$

where the summation is over the two neighbouring nodes of node i, in Fig. 2.1. therefore, Eq. (C.20) involves three temperature nodes.

C.3 Assembly of the Continuity Equation

In Appendix B, the algebraic approximation of the mass flow rate across a control volume face is written in terms of the nodal pressures as follows:

$$\begin{aligned} g_0 &= \tilde{g}_0 + \dot{g}_0 + \mathring{g}_0 \\ &= E_1^p\, p_1 + E_2^p\, p_2 + B_0 \end{aligned} \tag{C.21}$$

The discretized continuity equation can be assembled in the same manner as the discretized momentum equation. Since the assembly procedure is similar, only the resulting coefficients are presented.
For node (i):

$$A^c_{p(i)} = A^c_{p(i)} + E_1 \tag{C.22}$$

$$A^e_{p(i)} = A^e_{p(i)} - E_2 \tag{C.23}$$

$$A^{con}_{p(i)} = A^{con}_{p(i)} - B_0 \tag{C.24}$$

For node $(i+1)$:

$$A^c_{p(i+1)} = A^c_{p(i+1)} - E_2 \tag{C.25}$$

$$A^w_{p(i+1)} = A^w_{p(i+1)} + E_1 \tag{C.26}$$

$$A^{con}_{p(i+1)} = A^{con}_{p(i+1)} + B_0 \tag{C.27}$$

When these coefficients have been evaluated for every element in the calculation domain, the final form of the discretized continuity equation is obtained as follows:

$$A^c_{p(i)}\, p_{(i)} = A^e_{p(i)}\, p_{(i+1)} + A^w_{p(i)}\, p_{(i-1)} + A^{con}_{p(i)} \tag{C.28}$$

The above equation can be rewritten in the following compact form:

$$a_i^p\, p_i = \sum_n a_n^p\, p_n + b_i^p \tag{C.29}$$

where the summation is over the two nodes neighbouring node i in Fig. 2.1, therefore, Eq. (C.29) will involve three nodal pressures.

Appendix D

Interpolation Functions for the Proposed Two-Dimensional CVFEM

D.1 Interpolation of Pressure

In the proposed two-dimensional CVFEM, pressure is interpolated linearly within an element:

$$p = a_p x + b_p y + c_p \tag{D.1}$$

Substitution of the nodal values:

$$\begin{aligned} p &= p_1 \quad \text{at} \quad x = x_1 \text{ and } y = y_1 \\ p &= p_2 \quad \text{at} \quad x = x_2 \text{ and } y = y_2 \\ p &= p_3 \quad \text{at} \quad x = x_3 \text{ and } y = y_3 \end{aligned} \tag{D.2}$$

into Eq. (D.1) produces the following set of simultaneous, linear algebraic equations:

$$\begin{aligned} p_1 &= a_p x_1 + b_p y_1 + c_p \\ p_2 &= a_p x_2 + b_p y_2 + c_p \\ p_3 &= a_p x_3 + b_p y_3 + c_p \end{aligned} \tag{D.3}$$

Using Cramer's Rule to solve these equations results in the following expressions for the coefficients a_p, b_p, and c_p:

$$a_p = \frac{1}{det}\left((y_2 - y_3)p_1 + (y_3 - y_1)p_2 + (y_1 - y_2)p_3\right) \tag{D.4}$$

$$b_p = -\frac{1}{det}((x_2 - x_3)p_1 + (x_3 - x_1)p_2 + (x_1 - x_2)p_3) \quad (D.5)$$

$$c_p = \frac{1}{det}((x_2y_3 - x_3y_2)p_1 + (x_3y_1 - x_1y_3)p_2 + (x_1y_2 - x_2y_1)p_3) \quad (D.6)$$

where

$$det = x_1y_2 + x_2y_3 + x_3y_1 - y_1x_2 - y_2x_3 - y_3x_1 \quad (D.7)$$

Defining the following variables:

$$\begin{aligned} xmul_1 &= x_2 - x_3 \quad ymul_1 = y_2 - y_3 \quad xymul_1 = x_2y_3 - x_3y_2 \\ xmul_2 &= x_3 - x_1 \quad ymul_2 = y_3 - y_1 \quad xymul_2 = x_3y_1 - x_1y_3 \\ xmul_3 &= x_1 - x_2 \quad ymul_3 = y_1 - y_2 \quad xymul_3 = x_1y_2 - x_2y_1 \end{aligned} \quad (D.8)$$

allows the expressions for the coefficients to be rewritten more compactly as:

$$a_p = \frac{1}{det}\sum_{i=1}^{3} ymul_i p_i \quad (D.9)$$

$$b_p = -\frac{1}{det}\sum_{i=1}^{3} xmul_i p_i \quad (D.10)$$

$$c_p = \frac{1}{det}\sum_{i=1}^{3} xymul_i p_i \quad (D.11)$$

Furthermore, if variables D_i^x and D_i^y are defined:

$$D_i^x = ymul_i/det \quad ; \quad D_i^y = -xmul_i/det \quad (D.12)$$

then the pressure gradients may expressed in the following compact forms:

$$\frac{\partial p}{\partial x} = a_p = \sum_{i=1}^{3} D_i^x p_i \quad (D.13)$$

$$\frac{\partial p}{\partial y} = b_p = \sum_{i=1}^{3} D_i^y p_i \quad (D.14)$$

D.2 Interpolation of a Convected Scalar

In the proposed CVFEM, the MAss Weighted interpolation (MAW) scheme is used to interpolate convected scalars, e.g. the x and y components of velocity in the momentum equations, and temperature in the energy equation. The following

derivations are for the general scalar dependent variable ϕ, and all nomenclature is defined in Fig. 3.3. It is necessary to integrate the convective flux across the three control volume faces in an element. This integration is performed by assuming an integration point value on face k, ϕ_k^c, prevails over the control volume face. The following rules can be used to determine ϕ_k^c for the element shown in Fig. 3.3.

Control volume surface 1

$$\text{If } \dot{m}_1 > 0 \qquad \phi_1^c = f\phi_2^c + (1-f)\Phi_3 \tag{D.15}$$

$$\text{where} \qquad f = min\left[max\left(\frac{\dot{m}_2}{\dot{m}_1}, 0\right), 1\right] \tag{D.16}$$

$$\text{If } \dot{m}_1 < 0 \qquad \phi_1^c = f\phi_3^c + (1-f)\Phi_2 \tag{D.17}$$

$$\text{where} \qquad f = min\left[max\left(\frac{\dot{m}_3}{\dot{m}_1}, 0\right), 1\right] \tag{D.18}$$

Control volume surface 2

$$\text{If } \dot{m}_2 > 0 \qquad \phi_2^c = f\phi_3^c + (1-f)\Phi_1 \tag{D.19}$$

$$\text{where} \qquad f = min\left[max\left(\frac{\dot{m}_3}{\dot{m}_2}, 0\right), 1\right] \tag{D.20}$$

$$\text{If } \dot{m}_2 < 0 \qquad \phi_2^c = f\phi_1^c + (1-f)\Phi_3 \tag{D.21}$$

$$\text{where} \qquad f = min\left[max\left(\frac{\dot{m}_1}{\dot{m}_2}, 0\right), 1\right] \tag{D.22}$$

Control volume surface 3

$$\text{If } \dot{m}_3 > 0 \qquad \phi_3^c = f\phi_1^c + (1-f)\Phi_2 \tag{D.23}$$

$$\text{where} \qquad f = min\left[max\left(\frac{\dot{m}_1}{\dot{m}_3}, 0\right), 1\right] \tag{D.24}$$

$$\text{If } \dot{m}_3 < 0 \qquad \phi_3^c = f\phi_2^c + (1-f)\Phi_1 \tag{D.25}$$

$$\text{where} \qquad f = min\left[max\left(\frac{\dot{m}_2}{\dot{m}_3}, 0\right), 1\right] \tag{D.26}$$

The $\dot{m}_k$ terms are the integrated mass flow rate across the appropriate control volume face:

$$\dot{m}_k = \int_k \rho\vec{u} \cdot \vec{n}_k \, ds \tag{D.27}$$

therefore, the $\dot{m}_k$ term is positive when the velocity vector at the integration point is in the same direction as the assumed normal to the surface. The integration in Eq. (D.27) is performed using linear interpolation for ρ and $\vec{u}$.

In Eqs. (D.16) to (D.26), Φ represents the nodal value of ϕ, and ϕ_k^c represents the integration point values. Using Eqs. (D.16) to (D.26), the following system of equations may be obtained:

$$\begin{bmatrix} a_{11} & a_{12} & a_{13} \\ a_{21} & a_{22} & a_{23} \\ a_{31} & a_{32} & a_{33} \end{bmatrix} \begin{Bmatrix} \phi_1^c \\ \phi_2^c \\ \phi_3^c \end{Bmatrix} = \begin{bmatrix} b_{11} & b_{12} & b_{13} \\ b_{21} & b_{22} & b_{23} \\ b_{31} & b_{32} & b_{33} \end{bmatrix} \begin{Bmatrix} \Phi_1 \\ \Phi_2 \\ \Phi_3 \end{Bmatrix} \tag{D.28}$$

This can be written as:

$$[A]_{3\times 3} \{\phi^c\}_{3\times 1} = [B]_{3\times 3} \{\Phi\}_{3\times 1} \tag{D.29}$$

Multiplying both sides of the above equation by the inverse of $[A]$, the integration point values can be determined as:

$$\{\phi^c\}_{3\times 1} = [CC]_{3\times 3} \{\Phi\}_{3\times 1} \tag{D.30}$$

which may be rewritten as follows:

$$\phi_k^c = \sum_{j=1}^{3} CC_j^k \Phi_j \tag{D.31}$$

D.3 Interpolation of a Diffused Scalar

In the proposed CVFEM, the diffused scalars are interpolated linearly within an element. These scalars are, therefore, interpolated using function similar to Eq. (D.1), and Eqs. (D.9) to (D.11) define the interpolation function coefficients with the substitution of the appropriate dependent variable for the pressure, p.

D.4 Interpolation of Mass Conserving Velocity

In discretizing the momentum equations, the convected velocity components u and v are interpolated using the MAW scheme. Different interpolation functions are used for the 'mass conserving' velocities which appear in the continuity equation and in

the mass flux terms, $\rho\vec{v}\cdot\vec{n}$, in the momentum and energy equations. In the mass flux terms, the velocity components are interpolated by assuming a linear variation of the pseudo-velocities, $\hat{u}_i$ and $\hat{v}_i$, and pressure coefficients, d_0^u and d_0^v, used in conjunction with the local element pressure gradient. The following expressions define the 'mass conserving' velocities, u_i^m and v_i^m, at each node within an element:

$$u_i^m = \hat{u}_i - d_0^u \left(\frac{\partial p}{\partial x_i}\right)_e \tag{D.32}$$

$$v_i^m = \hat{v}_i - d_0^v \left(\frac{\partial p}{\partial y_i}\right)_e \tag{D.33}$$

The subscript, e, on the pressure gradient indicates that the element pressure gradient, and not the average pressure gradient over the control volume surrounding the node in question, is being used.

The pseudo-velocities and the pressure coefficients are known at the nodes. In order to determine the values of these quantities at the integration points on the control volume faces within the elements (see Fig. 3.3), a linear interpolation of the nodal values is used:

$$\hat{u}_i = a_u x + b_u y + c_u$$
$$d_0^u = a_d^u x + b_d^u y + c_d^u \tag{D.34}$$
$$\hat{v}_i = a_v x + b_v y + c_v$$
$$d_0^v = a_d^v x + b_d^v y + c_d^v \tag{D.35}$$

The coefficients in the above equations can be determined in the same manner as that used in Section D.1 for pressure.

D.5 Interpolation of Density

In the proposed CVFEM, the density is interpolated using the MAW scheme, therefore, the density at the integration point on face k can be written as follows:

$$\rho_k^c = \sum_{j=1}^{3} CC_j^k \rho_j \tag{D.36}$$

where the CC_j^k coefficients are defined as shown in Section D.2.

Appendix E

Integrated Fluxes in the Proposed Two-Dimensional CVFEM

E.1 Introduction

In Chapter 3, the governing equations for steady, two-dimensional, viscous compressible flows were written in the following conservative forms:

$$\vec{\nabla} \cdot \vec{J} = S \tag{E.1}$$

$$\vec{\nabla} \cdot \vec{g} = 0 \tag{E.2}$$

where, $\vec{J}$ is the combined convection-diffusion flux vector, S is the source term, and $\vec{g}$ is the mass flux vector $\rho\vec{v}$. Equation (E.1) represents the x-momentum equation when:

$$\vec{J} = \rho\vec{v}u - \mu\vec{\nabla}u \tag{E.3}$$

$$S = S^u - \frac{\partial p}{\partial x} + \frac{1}{3}\frac{\partial}{\partial x}\left(\mu\frac{\partial u}{\partial x}\right) + \frac{\partial}{\partial y}\left(\mu\frac{\partial v}{\partial x}\right) - \frac{2}{3}\frac{\partial}{\partial x}\left(\mu\frac{\partial v}{\partial y}\right) \tag{E.4}$$

the y momentum equation when:

$$\vec{J} = \rho\vec{v}v - \mu\vec{\nabla}v \tag{E.5}$$

$$S = S^v - \frac{\partial p}{\partial y} + \frac{1}{3}\frac{\partial}{\partial y}\left(\mu\frac{\partial v}{\partial y}\right) + \frac{\partial}{\partial x}\left(\mu\frac{\partial u}{\partial y}\right) - \frac{2}{3}\frac{\partial}{\partial y}\left(\mu\frac{\partial u}{\partial x}\right) \tag{E.6}$$

the energy equation when:

$$\vec{J} = \rho\vec{v}T - \frac{k}{c_p}\vec{\nabla}T \tag{E.7}$$

$$S = \frac{S^T}{c_p} + \frac{1}{c_p}\left(u\frac{\partial p}{\partial x} + v\frac{\partial p}{\partial y}\right) + \frac{1}{c_p}\Phi \tag{E.8}$$

and other conservation equations when:

$$\vec{J} = \rho\vec{v}\phi - \Gamma\vec{\nabla}\phi \quad : \quad S = S^{\phi} \tag{E.9}$$

Applying the appropriate conservation principle to a control volume V, which is fixed in space, integral forms of Eqs. (E.1) and (E.2) can be obtained:

$$\int_{\partial V} \vec{J} \cdot \vec{n}\, ds = \int_{V} S\, dV \tag{E.10}$$

$$\int_{\partial V} \vec{g} \cdot \vec{n}\, ds = 0 \tag{E.11}$$

where ∂V is the surface of the control volume, and $\vec{n}$ is unit outward vector normal to the differential area ds.

With reference to the polygonal control volume associated with a typical node 1 within the calculation domain, either an internal node or a boundary node as shown in Fig. 3.2, Eqs. (E.10) and (E.11) can be cast in the following forms:

$$\left[\int_{o}^{M_2} \vec{J} \cdot \vec{n}_2\, ds - \int_{o}^{M_3} \vec{J} \cdot \vec{n}_3\, ds - \int_{V} S\, dV\right] \tag{E.12}$$

$+$ [similar contributions from other elements associated with node 1]

$+$ [boundary contributions, if applicable] $= 0$

$$\left[\int_{o}^{M_2} \vec{g} \cdot \vec{n}_2\, ds - \int_{o}^{M_3} \vec{g} \cdot \vec{n}_3\, ds\right] \tag{E.13}$$

$+$ [similar contributions from other elements associated with node 1]

$+$ [boundary contributions, if applicable] $= 0$

To derive the element contributions to the control volume integral conservation equations, it is necessary to integrate the appropriate fluxes across the three control volume faces in an element. The procedures used in the proposed method to perform these integrations are described in this appendix. This discussion is presented in two sections: first the derivations for the convection-diffusion equation of scalar ϕ are discussed; then the necessary alterations for the momentum and energy equations are described; and finally, the integrals involved in the continuity equation are presented. All nomenclature used in this appendix is defined in Fig. 3.3. The assembly of the discretized forms of these equations will be discussed in Appendix F.

E.2 Convection-Diffusion Equation for Scalar ϕ

The convection-diffusion flux of ϕ is defined by Eq. (E.9). The integrated flux of ϕ across a control volume face k is expressed in the following manner:

$$\left(\begin{array}{c} \text{Integrated flux across} \\ \text{control volume face } k \end{array} \right) = \int_o^{M_k} \vec{J} \cdot \vec{n}_k \, ds \tag{E.14}$$

Substitution of Eq. (E.9) into this equation gives:

$$\int_o^{M_k} \vec{J} \cdot \vec{n}_k \, ds = \int_o^{M_k} \rho \vec{v} \phi \cdot \vec{n}_k \, ds - \int_o^{M_k} \Gamma \vec{\nabla} \phi \cdot \vec{n}_k \, ds \tag{E.15}$$

Using the MAW scheme in the convection terms and linear interpolation in the diffusion term, the integrated flux across control volume face k can be written as follows:

$$\int_o^{M_k} \vec{J} \cdot \vec{n}_k \, ds = \dot{m}^k \sum_{j=1}^{3} CC_j^k \, \phi_j \, \Delta s^k - \Gamma \left(A n_x + B n_y \right)^k \Delta s^k \tag{E.16}$$

In Eq. (E.16), $\dot{m}^k$ is the mass flow rate across control volume face k, which is evaluated using 'mass conserving' velocities, as shown in Section D.4. The coefficients A and B arise from the linear interpolation of ϕ in the diffusion term, and are defined by Eqs. (D.9) and (D.10) when p_i is replaced by ϕ_i. The components of the unit normal to face k, $\vec{n}_k$ are defined as follows:

$$n_x^k = \frac{y_k - y_o}{\Delta s^k} \quad ; \quad n_y^k = \frac{x_k - x_o}{\Delta s^k} \tag{E.17}$$

where x_k, y_k are the co-ordinates of side midpoint, M_k, and Δs^k is the length of control volume face k.

The integration in Eq. (E.16) can be rewritten in the following simple form:

$$\int_o^{M_k} \vec{J} \cdot \vec{n}_k \, ds = \sum_{j=1}^{3} C_j^k \, \phi_j \tag{E.18}$$

where:

$$C_j^k = \dot{m}^k CC_j^k - \Gamma \left(D_j^x n_x^k + D_j^y n_y^k \right) \Delta s^k \tag{E.19}$$

and the D_j^x and D_j^y terms are defined in Eq. (D.12).

The source term in Eq. (E.9) is linearized, and takes the following form for a subcontrol volume surrounding node i:

$$S = S_c^\phi + S_p^\phi \, \phi_i \tag{E.20}$$

where the value of ϕ_i is assumed to prevail over the subcontrol volume associated with node i, while S_c and S_p are evaluated at the centroid of an element, and these values are assumed to prevail over all subcontrol volumes within an element. The source term integration in Eq. (E.9) is simply:

$$\int_{V_e^i} S\,dv = S_c^\phi V_e^i + S_p^\phi \phi_i V_e^i \tag{E.21}$$

where V_e^i is the volume of the subcontrol volume within the element around node i.

E.3 Modifications for the Momentum and Energy Equations

E.3.1 Modifications for the Momentum Equations

The integrated convection-diffusion flux of x-momentum across control volume face k can be written in the same form as Eq. (E.18) when the diffusion coefficient, Γ, is replaced by the dynamic viscosity, μ, as follows:

$$\left(\begin{array}{c}\text{Integrated flux across}\\ \text{control volume face } k\end{array}\right) = \int_o^{M_k} \vec{J}\cdot\vec{n}_k\,ds = \sum_{j=1}^{3} C_j^k u_j \tag{E.22}$$

where

$$C_j^k = \dot{m}^k CC_j^k - \mu\left(D_j^x n_x^k + D_j^y n_y^k\right)\Delta s^k \tag{E.23}$$

The integral of the source term over the subcontrol volume in the element around node i, Eq. (E.4) can be written as follows:

$$\int_{V_e^i} S\,dV = S_c^u V_e^i + S_p^u u_i V_e^i - V_e^i \sum_{j=1}^{3} D_j^x p_j + S_{vis}^u \tag{E.24}$$

where S_{vis}^u represents the integration of the extra viscous terms over the subcontrol volume V_e^i and has the following form for the x-momentum equation:

$$\begin{aligned} S_{vis}^u &= \int_{V_e^i}\left[\frac{1}{3}\frac{\partial}{\partial x}\left(\mu\frac{\partial u}{\partial x}\right) + \frac{1}{3}\frac{\partial}{\partial x}\left(\mu\frac{\partial v}{\partial y}\right)\right]dV \\ &= \int_{V_e^i}\frac{\mu}{3}\vec{\nabla}\cdot\left(\frac{\partial u}{\partial x}\vec{i} + \frac{\partial v}{\partial x}\vec{j}\right)dV \end{aligned} \tag{E.25}$$

$$= \int_{\partial V_e^i} \frac{\mu}{3}\left(\frac{\partial u}{\partial x}\vec{i} + \frac{\partial v}{\partial x}\vec{j}\right)\cdot \vec{n} ds$$

$$= \int_{\partial V_e^i} \frac{\mu}{3}\left(a_u n_x + a_v n_y\right) ds$$

where a_u,b_u,a_v and b_v are the coefficients from the linearization of velocity components u and v that have the following formula:

$$a_u = \sum_{i=1}^{3} D_i^x u_i \quad ; \quad b_u = \sum_{i=1}^{3} D_i^y u_i$$
$$a_v = \sum_{i=1}^{3} D_i^x v_i \quad ; \quad b_v = \sum_{i=1}^{3} D_i^y v_i \tag{E.26}$$

With the reference to Fig. 3.2a, the elemental contribution of the integration of extra viscous terms, S_{vis}^u, for the control volume around node 1 may be written as follows:

$$\begin{aligned} S_{vis}^u &= S_u^3 + S_u^2 \\ &= \int_{\partial V_e^1} \frac{\mu}{3}\left(a_u n_x + a_v n_y\right) ds \\ &= \frac{\mu}{3}\left(a_u n_x^3 + a_v n_y^3\right)\Delta s^1 + \frac{\mu}{3}\left(a_u n_x^2 + a_v n_y^2\right)\Delta s^2 \end{aligned} \tag{E.27}$$

where

$$S_u^3 = \frac{\mu}{3}\left(a_u n_x^3 + a_v n_y^3\right)\Delta s^1 \tag{E.28}$$
$$S_u^2 = \frac{\mu}{3}\left(a_u n_x^2 + a_v n_y^2\right)\Delta s^2 \tag{E.29}$$

For the y-momentum equation, the integrated convection-diffusion flux across a control volume face k is defined by Eqs. (E.22) and (E.23). The source term integration is defined as follows:

$$\int_{V_e^i} S\, dV = S_c^v V_e^i + S_p^v v_i V_e^i - V_e^i \sum_{i=1}^{3} D_i^y p_i + S_{vis}^v \tag{E.30}$$

where S_{vis}^v are the extra viscous terms in the y-momentum equation, and this term is evaluated the same way as in x-momentum equation.

E.3.2 Modifications for the Energy Equations

For the energy equation, the diffusion coefficient, Γ, is replaced by k/c_p, and the integral of the convection-diffusion flux across a control volume face k within an

element can be written as follows:

$$\left(\begin{array}{c} \text{Integrated flux across} \\ \text{control volume face k} \end{array} \right) = \int_o^{\Delta l_k} \vec{J} \cdot \vec{n}_k \, ds = \sum_{j=1}^{3} C_j^k T_j \tag{E.31}$$

where

$$C_j^k = \dot{m}^k C C_j^k - \frac{k}{c_p} \left(D_j^x n_x^k + D_j^y n_y^k \right) \Delta s^k \tag{E.32}$$

The integration of the source term in the energy equation gives:

$$\int_V S dV = \int_V \frac{1}{c_p} \left(S^T + u \frac{\partial p}{\partial x} + v \frac{\partial p}{\partial y} + \Phi \right) dV \tag{E.33}$$

where

$$\Phi = \mu \left[2 \left(\frac{\partial u}{\partial x} \right)^2 + 2 \left(\frac{\partial v}{\partial y} \right)^2 + \left(\frac{\partial v}{\partial x} + \frac{\partial u}{\partial y} \right)^2 - \frac{2}{3} \left(\frac{\partial u}{\partial x} + \frac{\partial v}{\partial y} \right)^2 \right] \tag{E.34}$$

Using linear interpolation of u and v to evaluate Φ, and linear interpolation for pressure, Eq. (E.33) can be rewritten as:

$$\int_V S dV = \frac{V_e}{c_p} \left(S_c^T + S_p^T T + u_{av} \sum_{i=1}^{3} D_i^x p_i + v_{av} \sum_{i=1}^{3} D_i^y p_i + \Phi_c \right) \tag{E.35}$$

where

$$u_{av} = \frac{u_1 + u_2 + u_3}{3} \quad : \quad u_{av} = \frac{u_1 + u_2 + u_3}{3} \tag{E.36}$$

$$\Phi_c = \mu \left[2a_u^2 + 2b_v^2 + (a_v + b_u)^2 - \frac{2}{3}(a_u + b_v)^2 \right] \tag{E.37}$$

and a_u,a_v, etc. are defined in equation E.26.

E.4 Continuity Equation

E.4.1 Introduction

In the proposed CVFEM, the mass flux, $\vec{g} = \rho \vec{v}$, is linearized with respect to density and velocity:

$$\vec{g} = \vec{\tilde{g}} + \vec{\bullet} - \vec{\circ} \tag{E.38}$$

where $\vec{\tilde{g}}$ is linearized with respect to velocity:

$$\vec{\tilde{g}} = \rho^* \vec{v}^m \tag{E.39}$$

$\vec{\bullet}{\vec{g}}$ is linearized with respect to density:

$$\vec{\bullet}{\vec{g}} = \rho \vec{v}^{m*} \tag{E.40}$$

and $\vec{\circ}{\vec{g}}$ is determined from available values of density and velocity:

$$\vec{\circ}{\vec{g}} = \rho^* \vec{v}^{m*} \tag{E.41}$$

where variables with a superscript * are known or calculated from available values. This linearized mass flux is integrated over a control volume face k, to give:

$$\left(\begin{array}{l} \text{Integrated mass flux across} \\ \text{control volume face } k \end{array} \right) = \int_o^{M_k} \vec{g} \cdot \vec{n}_k \, ds \tag{E.42}$$
$$= \int_o^{M_k} \vec{\sim}{\vec{g}} \cdot \vec{n}_k \, ds + \int_o^{M_k} \vec{\bullet}{\vec{g}} \cdot \vec{n}_k \, ds - \int_o^{M_k} \vec{\circ}{\vec{g}} \cdot \vec{n}_k \, ds$$

The algebraic approximation to the integrals in Eq. (E.42) are described in the following subsections.

E.4.2 Integration of $\vec{\sim}{\vec{g}}$

The integration of $\vec{\sim}{\vec{g}}$ has the form:

$$\int_o^{M_k} \vec{\sim}{\vec{g}} \cdot \vec{n}_k \, ds = \int_o^{M_k} \rho^* \left(u^m n_x + v^m n_y \right) ds \tag{E.43}$$

Substitution of Eqs. (D.32) and (D.33) into the above integral gives:

$$\int_o^{M_k} \vec{\sim}{\vec{g}} \cdot \vec{n}_k \, ds$$
$$= \int_o^{M_k} \rho^* \left[(\hat{u} - d_0^u \frac{\partial p}{\partial x}) n_x + (\hat{v} - d_0^v \frac{\partial p}{\partial y}) n_y \right] \tag{E.44}$$

Writing the integral in terms of nodal pressures:

$$\int_o^{M_k} \vec{\sim}{\vec{g}} \cdot \vec{n}_k \, ds = \int_o^{M_k} \rho^* \left(\hat{u} n_x + \hat{v} n_y \right) ds + \int_o^{M_k} \rho^* \sum_{j=1}^{3} \left(-d_0^v D_j^y n_y - d_0^u D_j^x n_x \right) p_j \, ds \tag{E.45}$$

Using the MAW interpolation scheme for ρ^* and linear interpolation for the remaining variables, the integral is evaluated using Simpson's Rule.

E.4.3 Integration of $\vec{\dot{g}}$

The integration of $\vec{\dot{g}}$ takes the form:

$$\int_o^{M_k} \vec{\dot{g}} \cdot \vec{n}_k \, ds = \int_o^{M_k} \rho \left(u^{m^*} n_x + v^{m^*} n_y \right) ds \tag{E.46}$$

In the proposed method, the density is interpolated by the equation of state, therefore, this term is in effect linearized with respect to pressure, and is evaluated as follows:

$$\rho = \sum_{j=1}^{3} CC_j^k R \left(\frac{p_j}{T_j} \right) \tag{E.47}$$

The integral in Eq. (E.46) may be written in terms of nodal pressures as follows:

$$\int_o^{M_k} \vec{\dot{g}} \cdot \vec{n}_k \, ds = \int_o^{M_k} \sum_{j=1}^{3} \left[\left(u^{m^*} n_x + v^{m^*} n_y \right) R \left(\frac{CC_j^k}{T_j} \right) p_j \, ds \right] \tag{E.48}$$

Using linear interpolation for u^{m^*} and v^{m^*}, Eqs. (D.32) and (D.33), with available pressures included in the pressure gradients in these equations, the integral in Eq. (E.48) is evaluated using Simpson's Rule.

E.4.4 Integration of $\vec{\mathring{g}}$

Using available values in all terms, the integration of $\vec{\mathring{g}}$ can be written as follows:

$$\int_o^{M_k} \vec{\mathring{g}} \cdot \vec{n}_k \, ds = \int_o^{M_k} \rho^* \left(u^{m^*} n_x + v^{m^*} n_y \right) ds \tag{E.49}$$

Applying MAW interpolation for density, and linear interpolation for the mass conserving velocities, the integral can be evaluated by Simpson's Rule.

E.4.5 Integration of $\vec{g}$

Summarizing the last three subsections, the integral of the mass flux through control volume face k can be cast in the following form:

$$\int_o^{M_k} \vec{g} \cdot \vec{n}_k \, ds = E_j^k p_j + F^k \tag{E.50}$$

where

$$\begin{aligned} E_j^k &= \int_o^{M_k} \left[\rho^* \left(-d_0^v D_j^y n_y - d_0^u D_j^x n_x \right) + \left(u^{m^*} n_x + v^{m^*} n_y \right) R \left(\frac{CC_j^k}{T_j} \right) \right] ds \\ F^k &= \int_o^{M_k} \rho^* \left[\left(\hat{u} - u^{m^*} \right) n_x + \left(\hat{v} - v^{m^*} \right) n_y \right] ds \end{aligned} \tag{E.51}$$

and the integrals in Eq. (E.51) are evaluated using Simpson's Rule.

Appendix F

Assembly of the Discretized Conservation Equations in the Proposed Two-Dimensional CVFEM

F.1 Introduction

The methods used to integrate the fluxes of mass, momentum, and energy across the three control volume faces in an element were described in Appendix E. Integration of the appropriate source terms was also discussed. These integrated fluxes and source terms are used to compile the complete discretized forms of the integral conservation equations for a control volume. The appropriate compilation of the final forms of the discretized equations is presented in this Appendix. This discussion will be presented in three sections: the first section describes the assembly of the discretized forms of the x- and y-momentum equations; the second section concentrates on the assembly of the energy equation; and the third section focuses on the compilation of the continuity equation coefficients.

In the assembly of the discretized equations, reference is made to the nomenclature in Figs. 3.4 and 3.5. The polygonal control volume constructed around an internal node (i, j) in a calculation domain, and all of the elements that are associated with this control volume are shown in Fig. 3.5. Figure 3.4 shows the four types of elements that are used in Fig. 3.5, with their corresponding node numbering schemes. These four elements result from the two possible orientations of the diagonal. In these figures, the number of a control volume face is indicated by the

normal vectors. And these normal vectors are used in the integration of the fluxes described in Appendix E.

F.2 Assembly of the Momentum Equations

F.2.1 x-Momentum Equation

For the x-momentum equation, the integral of the flux across a control volume face k within an element is written as follows in Appendix E:

$$\left(\begin{array}{c} \text{Integrated flux across} \\ \text{control volume face k} \end{array} \right) = \int_o^{M_k} \vec{J} \cdot \vec{n}_k ds = \sum_{i=1}^{3} C_j^k u_j \qquad \text{(F.1)}$$

and the element contribution to the volume integration of the source for the control volume around node 1 is given by:

$$\int_{V_e^1} S dV = \frac{V_e}{3} \left(S_c^u + S_p^u u_1 - \sum_{i=1}^{3} D_i^x p_i \right) + S_u^3 + S_u^2 \qquad \text{(F.2)}$$

where V_e is the volume of the element, which is three times of the volume of sub-control volume associate with node 1, V_e^1.

The assembly of the final discretized form of the momentum equation is done in an element-by-element manner. When each element is considered separately, the appropriate C_j^k terms are derived for each node, j, and control volume face, k; this gives nine C_j^k terms per element. With reference to the node labeling in Fig. 3.5, new coefficients can be defined in each element that simplify the assembly of the control volume integral conservation equation.

With respect to the type 1 and quad 1 element in Fig. 3.4, the following coefficients can be evaluated when node 1 is node (i, j), node 2 is node $(i+1, j)$, and node 3 is node $(i+1, j+1)$:
With respect to node (i, j):

$$A_{u(i,j)}^c = A_{u(i,j)}^c + C_1^2 - C_1^3 - S_p^u \frac{V_e}{3} \qquad \text{(F.3)}$$

$$A_{u(i,j)}^e = A_{u(i,j)}^e + C_2^3 - C_2^2 \qquad \text{(F.4)}$$

$$A_{u(i,j)}^{ne} = A_{u(i,j)}^{ne} + C_3^3 - C_3^2 \qquad \text{(F.5)}$$

$$A_{u(i,j)}^{con} = A_{u(i,j)}^{con} + (S_c^u - \sum_{m=1}^{3} D_m^x p_m) \frac{V_e}{3} + S_u^2 + S_u^3 \qquad \text{(F.6)}$$

The coefficients appear on both sides of these equations, because contributions will also be made from other elements, and previous contributions must be maintained. The source-related terms are added to the appropriate coefficients to complete the assembly for node (i, j) in the type 1 and quad 1 element of Fig. 3.4. Similar procedures are used to assemble the coefficients at the other nodes in the element.

With respect to node $(i+1, j)$:

$$A^c_{u(i+1,j)} = A^c_{u(i+1,j)} + C^3_2 - C^1_2 - S^u_p \frac{V_e}{3} \tag{F.7}$$

$$A^n_{u(i+1,j)} = A^n_{u(i+1,j)} + C^1_3 - C^3_3 \tag{F.8}$$

$$A^w_{u(i+1,j)} = A^w_{u(i+1,j)} + C^1_1 - C^3_1 \tag{F.9}$$

$$A^{con}_{u(i+1,j)} = A^{con}_{u(i+1,j)} + (S^u_c - \sum_{m=1}^{3} D^x_m p_m)\frac{V_e}{3} + S^3_u + S^1_u \tag{F.10}$$

With respect to node $(i+1, j+1)$:

$$A^c_{u(i+1,j+1)} = A^c_{u(i+1,j+1)} + C^1_3 - C^2_3 - S^u_p \frac{V_e}{3} \tag{F.11}$$

$$A^{sw}_{u(i+1,j+1)} = A^{sw}_{u(i+1,j+1)} + C^2_1 - C^1_1 \tag{F.12}$$

$$A^s_{u(i+1,j+1)} = A^s_{u(i+1,j+1)} + C^2_2 - C^1_2 \tag{F.13}$$

$$A^{con}_{u(i+1,j+1)} = A^{con}_{u(i+1,j+1)} + (S^u_c - \sum_{m=1}^{3} D^x_m p_m)\frac{V_e}{3} + S^1_u + S^2_u \tag{F.14}$$

The contribution to the coefficient $A^c_{u(i+1,j+1)}$ is the portion of the net transport of x-momentum out of the control volume surrounding node $(i+1, j+1)$, associated with u_3 in Fig. 3.4 or $u_{i+1,j+1}$ in Fig. 3.5: this is calculated from the difference between the amount transported out over control volume face 1 in Fig. 3.4. C^1_3, less the amount transported in over face 2, C^2_3. The other coefficients are determined by the transport of x-momentum in over control volume face 2 less the amount transported out over face 1, in Fig. 3.4: the portion associated with u_2 is added to $A^w_{u(i+1,j+1)}$, and the portion associated with u_1 is added to $A^{sw}_{u(i+1,j+1)}$.

For the type 2 and quad 1 element of Fig. 3.4, the following coefficients can be evaluated when node 1 is node (i, j), node 2 is node $(i+1, j+1)$, and node 3 is node $(i, j+1)$:

With respect to node (i, j):

$$A^c_{u(i,j)} = A^c_{u(i,j)} + C^2_1 - C^3_1 - S^u_p \frac{V_e}{3} \tag{F.15}$$

$$A^{ne}_{u(i,j)} = A^{ne}_{u(i,j)} + C^3_2 - C^2_2 \tag{F.16}$$

$$A^{n}_{u(i,j)} = A^{n}_{u(i,j)} + C^3_3 - C^2_3 \tag{F.17}$$

$$A^{con}_{u(i,j)} = A^{con}_{u(i,j)} + (S^u_c - \sum_{m=1}^{3} D^x_m p_m)\frac{V_e}{3} + S^2_u + S^3_u \tag{F.18}$$

With respect to node $(i+1, j+1)$:

$$A^{c}_{u(i+1,j+1)} = A^{c}_{u(i+1,j+1)} + C^3_2 - C^1_2 - S^u_p\frac{V_e}{3} \tag{F.19}$$

$$A^{w}_{u(i+1,j+1)} = A^{w}_{u(i+1,j+1)} + C^1_3 - C^3_3 \tag{F.20}$$

$$A^{sw}_{u(i+1,j+1)} = A^{sw}_{u(i+1,j+1)} + C^1_1 - C^3_1 \tag{F.21}$$

$$A^{con}_{u(i+1,j+1)} = A^{con}_{u(i+1,j+1)} + (S^u_c - \sum_{m=1}^{3} D^x_m p_m)\frac{V_e}{3} + S^1_u + S^3_u \tag{F.22}$$

With respect to node $(i, j+1)$:

$$A^{c}_{u(i,j+1)} = A^{c}_{u(i,j+1)} + C^1_3 - C^2_3 - S^u_p\frac{V_e}{3} \tag{F.23}$$

$$A^{s}_{u(i,j+1)} = A^{s}_{u(i,j+1)} + C^2_1 - C^1_1 \tag{F.24}$$

$$A^{e}_{u(i,j+1)} = A^{e}_{u(i,j+1)} + C^2_2 - C^1_2 \tag{F.25}$$

$$A^{con}_{u(i,j+1)} = A^{con}_{u(i,j+1)} + (S^u_c - \sum_{m=1}^{3} D^x_m p_m)\frac{V_e}{3} + S^1_u + S^2_u \tag{F.26}$$

For the type 1 and quad 2 element in Fig. 3.4, the following coefficients can be evaluated when node 1 is node $(i+1, j)$, node 2 is node $(i, j+1)$, and node 3 is node (i, j):

With respect to node $(i+1, j)$:

$$A^{c}_{u(i+1,j)} = A^{c}_{u(i+1,j)} + C^2_1 - C^3_1 - S^u_p\frac{V_e}{3} \tag{F.27}$$

$$A^{nw}_{u(i+1,j)} = A^{nw}_{u(i+1,j)} + C^3_2 - C^2_2 \tag{F.28}$$

$$A^{w}_{u(i+1,j)} = A^{w}_{u(i+1,j)} + C^3_3 - C^2_3 \tag{F.29}$$

$$A^{con}_{u(i+1,j)} = A^{con}_{u(i+1,j)} + (S^u_c - \sum_{m=1}^{3} D^x_m p_m)\frac{V_e}{3} + S^2_u + S^3_u \tag{F.30}$$

With respect to node $(i, j+1)$:

$$A^{c}_{u(i,j+1)} = A^{c}_{u(i,j+1)} + C^3_2 - C^1_2 - S^u_p\frac{V_e}{3} \tag{F.31}$$

$$A^{se}_{u(i,j+1)} = A^{se}_{u(i,j+1)} + C^1_1 - C^3_1 \tag{F.32}$$

$$A^{s}_{u(i,j+1)} = A^{s}_{u(i,j+1)} + C^1_3 - C^3_3 \tag{F.33}$$

$$A^{con}_{u(i,j+1)} = A^{con}_{u(i,j+1)} + (S^u_c - \sum_{m=1}^{3} D^x_m p_m)\frac{V_e}{3} + S^1_u + S^3_u \tag{F.34}$$

With respect to node (i,j):

$$A^c_{u(i,j)} = A^c_{u(i,j)} + C^1_3 - C^2_3 - S^u_p \frac{V_e}{3} \tag{F.35}$$

$$A^e_{u(i,j)} = A^e_{u(i,j)} + C^2_1 - C^1_1 \tag{F.36}$$

$$A^n_{u(i,j)} = A^n_{u(i,j)} + C^2_2 - C^1_2 \tag{F.37}$$

$$A^{con}_{u(i,j)} = A^{con}_{u(i,j)} + (S^u_c - \sum_{m=1}^{3} D^x_m p_m)\frac{V_e}{3} + S^1_u + S^2_u \tag{F.38}$$

For the type 2 and quad 2 element of Fig. 3.4, the following coefficients can be evaluated when node 1 is node $(i+1,j)$, node 2 is node $(i+1,j+1)$, and node 3 is node $(i,j+1)$:

With respect to node $(i+1,j)$:

$$A^c_{u(i+1,j)} = A^c_{u(i+1,j)} + C^2_1 - C^3_1 - S^u_p \frac{V_e}{3} \tag{F.39}$$

$$A^n_{u(i+1,j)} = A^n_{u(i+1,j)} + C^3_2 - C^2_2 \tag{F.40}$$

$$A^{nw}_{u(i+1,j)} = A^{nw}_{u(i+1,j)} + C^3_3 - C^2_3 \tag{F.41}$$

$$A^{con}_{u(i+1,j)} = A^{con}_{u(i+1,j)} + (S^u_c - \sum_{m=1}^{3} D^x_m p_m)\frac{V_e}{3} + S^2_u + S^3_u \tag{F.42}$$

With respect to node $(i+1,j+1)$:

$$A^c_{u(i+1,j+1)} = A^c_{u(i+1,j+1)} + C^3_2 - C^1_2 - S^u_p \frac{V_e}{3} \tag{F.43}$$

$$A^w_{u(i+1,j+1)} = A^w_{u(i+1,j+1)} + C^1_3 - C^3_3 \tag{F.44}$$

$$A^s_{u(i+1,j+1)} = A^s_{u(i+1,j+1)} + C^1_1 - C^3_1 \tag{F.45}$$

$$A^{con}_{u(i+1,j+1)} = A^{con}_{u(i+1,j+1)} + (S^u_c - \sum_{m=1}^{3} D^x_m p_m)\frac{V_e}{3} + S^1_u + S^3_u \tag{F.46}$$

With respect to node $(i,j+1)$:

$$A^c_{u(i,j+1)} = A^c_{u(i,j+1)} + C^1_3 - C^2_3 - S^u_p \frac{V_e}{3} \tag{F.47}$$

$$A^{se}_{u(i,j+1)} = A^{se}_{u(i,j+1)} + C^2_1 - C^1_1 \tag{F.48}$$

$$A^e_{u(i,j+1)} = A^e_{u(i,j+1)} + C^2_2 - C^1_2 \tag{F.49}$$

$$A^{con}_{u(i,j+1)} = A^{con}_{u(i,j+1)} + (S^u_c - \sum_{m=1}^{3} D^x_m p_m)\frac{V_e}{3} + S^1_u + S^2_u \tag{F.50}$$

When these coefficients have been evaluated and assembled for every element in the calculation domain, the final form of the discretized x-momentum equation

for each node is obtained as follows:

$$\begin{aligned} A^c_{u(i,j)} u_{(i,j)} &= A^e_{u(i,j)} u_{(i+1,j)} + A^{ne}_{u(i,j)} u_{(i+1,j+1)} \\ &+ A^n_{u(i,j)} u_{(i,j+1)} + A^{nw}_{u(i,j)} u_{(i-1,j+1)} \\ &+ A^w_{u(i,j)} u_{(i-1,j)} + A^{sw}_{u(i,j)} u_{(i-1,j-1)} \\ &+ A^s_{u(i,j)} u_{(i,j-1)} + A^{se}_{u(i,j)} u_{(i+1,j-1)} \\ &+ A^{con}_{u(i,j)} \end{aligned} \tag{F.51}$$

Comparison of this equation with Fig. 3.5 shows that all of the nodes neighbouring node (i, j) make a contribution to the discretization equation. Equation (F.51) may be written in the following compact form:

$$a^u_i u_i = \sum_n a^u_n u_n + b^u_i \tag{F.52}$$

where the summation is over the eight nodes that are neighbouring node i, or (i, j), in Fig. 3.5. The discretized x-momentum equation involves nine u velocity nodes. Equation (F.51) includes the maximum number of neighbour coefficients: for nodes with less connections, the appropriate coefficients will have value zero.

F.2.2 y-Momentum Equation

As discussed in Appendix E, the C^k_i terms multiplying the nodal velocities in the expression for the integrated flux across a control volume face, Eq. (F.1), are identical for both the x- and y-momentum equations. This similarity is used during the computer implementation of the proposed method by setting the appropriate coefficients in the discretized y-momentum equation equal to those evaluated for the x-momentum equation. The coefficients which do not need to be reevaluated are A^e_v, A^{ne}_v, A^n_v, A^{nw}_v, A^w_v, A^{sw}_v, A^s_v and A^{se}_v. The coefficients containing source or pressure gradient terms, which are unique to the y-momentum equation, must be evaluated. These coefficients are specified using the same procedures as for the x-momentum equation, and are given by the following expressions. For the type 1 quad 1 element of Fig. 3.4, the following coefficients must be evaluated:
With respect to node (i, j):

$$A^c_{v(i,j)} = A^c_{v(i,j)} + C^2_1 - C^3_1 - S^v_p \frac{V_e}{3} \tag{F.53}$$

$$A^{con}_{(i,j)} = A^{con}_{(i,j)} + (S^v_c - \sum_{m=1}^{3} D^y_m p_m) \frac{V_e}{3} + S^2_v + S^3_v \tag{F.54}$$

With respect to node $(i+1, j)$:

$$A^{c}_{v(i+1,j)} = A^{c}_{v(i+1,j)} + C^{3}_{2} - C^{1}_{2} - S^{v}_{p}\frac{V_e}{3} \tag{F.55}$$

$$A^{con}_{(i+1,j)} = A^{con}_{(i+1,j)} + (S^{v}_{c} - \sum_{m=1}^{3} D^{y}_{m} p_m)\frac{V_e}{3} + S^{1}_{v} + S^{3}_{v} \tag{F.56}$$

With respect to node $(i+1, j+1)$:

$$A^{c}_{v(i+1,j+1)} = A^{c}_{v(i+1,j+1)} + C^{1}_{3} - C^{2}_{3} - S^{v}_{p}\frac{V_e}{3} \tag{F.57}$$

$$A^{con}_{v(i+1,j+1)} = A^{con}_{v(i+1,j+1)} + (S^{v}_{c} - \sum_{m=1}^{3} D^{y}_{m} p_m)\frac{V_e}{3} + S^{1}_{v} + S^{2}_{v} \tag{F.58}$$

For the type 2 and quad 1 element of Fig. 3.4, the following coefficients must be evaluated:
With respect to node (i, j):

$$A^{c}_{v(i,j)} = A^{c}_{v(i,j)} + C^{2}_{1} - C^{3}_{1} - S^{v}_{p}\frac{V_e}{3} \tag{F.59}$$

$$A^{con}_{v(i,j)} = A^{con}_{v(i,j)} + (S^{v}_{c} - \sum_{m=1}^{3} D^{y}_{m} p_m)\frac{V_e}{3} + S^{2}_{v} + S^{3}_{v} \tag{F.60}$$

With respect to node $(i+1, j+1)$:

$$A^{c}_{v(i+1,j+1)} = A^{c}_{v(i+1,j+1)} + C^{3}_{2} - C^{1}_{2} - S^{v}_{p}\frac{V_e}{3} \tag{F.61}$$

$$A^{con}_{v(i+1,j+1)} = A^{con}_{v(i+1,j+1)} + (S^{v}_{c} - \sum_{m=1}^{3} D^{y}_{m} p_m)\frac{V_e}{3} + S^{1}_{v} + S^{3}_{v} \tag{F.62}$$

With respect to node $(i, j+1)$:

$$A^{c}_{v(i,j+1)} = A^{c}_{v(i,j+1)} + C^{1}_{3} - C^{2}_{3} - S^{v}_{p}\frac{V_e}{3} \tag{F.63}$$

$$A^{con}_{v(i,j+1)} = A^{con}_{v(i,j+1)} + (S^{v}_{c} - \sum_{m=1}^{3} D^{y}_{m} p_m)\frac{V_e}{3} + S^{1}_{v} + S^{2}_{v} \tag{F.64}$$

For the type 1 and quad 2 element of Fig. 3.4, the following coefficients must be evaluated:
With respect to node $(i+1, j)$:

$$A^{c}_{v(i+1,j)} = A^{c}_{v(i+1,j)} + C^{2}_{1} - C^{3}_{1} - S^{v}_{p}\frac{V_e}{3} \tag{F.65}$$

$$A^{con}_{v(i+1,j)} = A^{con}_{v(i+1,j)} + (S^{v}_{c} - \sum_{m=1}^{3} D^{y}_{m} p_m)\frac{V_e}{3} + S^{2}_{v} + S^{3}_{v} \tag{F.66}$$

With respect to node $(i, j+1)$:

$$A^c_{v(i,j+1)} = A^c_{v(i,j+1)} + C^3_2 - C^1_2 - S^v_p \frac{V_e}{3} \tag{F.67}$$

$$A^{con}_{v(i,j+1)} = A^{con}_{v(i,j+1)} + (S^v_c - \sum_{m=1}^{3} D^y_m p_m)\frac{V_e}{3} + S^1_v + S^3_v \tag{F.68}$$

With respect to node (i, j):

$$A^c_{v(i,j)} = A^c_{v(i,j)} + C^1_3 - C^2_3 - S^v_p \frac{V_e}{3} \tag{F.69}$$

$$A^{con}_{v(i,j)} = A^{con}_{v(i,j)} + (S^v_c - \sum_{m=1}^{3} D^y_m p_m)\frac{V_e}{3} + S^1_v + S^2_v \tag{F.70}$$

For the type 2 and quad 2 element of Fig. 3.4, the following coefficients must be evaluated:

With respect to node $(i+1, j)$:

$$A^c_{v(i+1,j)} = A^c_{v(i+1,j)} + C^2_1 - C^3_1 - S^v_p \frac{V_e}{3} \tag{F.71}$$

$$A^{con}_{v(i+1,j)} = A^{con}_{v(i+1,j)} + (S^v_c - \sum_{m=1}^{3} D^y_m p_m)\frac{V_e}{3} + S^2_v + S^3_v \tag{F.72}$$

With respect to node $(i+1, j+1)$:

$$A^c_{v(i+1,j+1)} = A^c_{v(i+1,j+1)} + C^3_2 - C^1_2 - S^v_p \frac{V_e}{3} \tag{F.73}$$

$$A^{con}_{v(i+1,j+1)} = A^{con}_{v(i+1,j+1)} + (S^v_c - \sum_{m=1}^{3} D^y_m p_m)\frac{V_e}{3} + S^1_v + S^3_v \tag{F.74}$$

With respect to node $(i, j+1)$:

$$A^c_{v(i,j+1)} = A^c_{v(i,j+1)} + C^1_3 - C^2_3 - S^v_p \frac{V_e}{3} \tag{F.75}$$

$$A^{con}_{v(i,j+1)} = A^{con}_{v(i,j+1)} + (S^v_c - \sum_{m=1}^{3} D^y_m p_m)\frac{V_e}{3} + S^1_v + S^2_v \tag{F.76}$$

When these coefficients have been evaluated and assembled for every element in the calculation domain, the final form of the discretized y-momentum equation for each node is obtained as follows:

$$\begin{aligned} A^c_{v(i,j)}\, v_{(i,j)} &= A^e_{v(i,j)}\, v_{(i+1,j)} + A^{ne}_{v(i,j)}\, v_{(i+1,j+1)} \\ &+ A^n_{v(i,j)}\, v_{(i,j+1)} + A^{nw}_{v(i,j)}\, v_{(i-1,j+1)} \\ &+ A^w_{v(i,j)}\, v_{(i-1,j)} + A^{sw}_{v(i,j)}\, v_{(i-1,j-1)} \\ &+ A^s_{v(i,j)}\, v_{(i,j-1)} + A^{se}_{v(i,j)}\, v_{(i+1,j-1)} \\ &+ A^{con}_{(i,j)} \end{aligned} \tag{F.77}$$

Equation (F.77) may be written in the following compact form:

$$a_i^v v_i = \sum_n a_n^v v_n + b_i^v \tag{F.78}$$

where the summation is over the eight nodes that are neighbouring node i, or (i,j), in Fig. 3.5. The discretized y-momentum equation involves a maximum of nine v velocity nodes.

F.3 Assembly of the Energy Equation

As discussed in Appendix E, the coefficients C_j^k are identical for any convection-diffusion equation. In the computer implementation of the proposed method, these coefficients are set equal to those evaluated for x- and y-momentum equations. The coefficients which do not need to be reevaluated are A_T^e, A_T^{ne}, A_T^n, A_T^{nw}, A_T^w, A_T^{sw}, A_T^s and A_T^{se}. The coefficients concerning source or pressure gradient terms, which are unique to the energy equation, must be evaluated. These coefficients are specified using the same procedures as for the x- and y-momentum equations, and are given by the following expressions: for the type 1 quad 1 element of Fig. 3.4.
With respect to node (i,j):

$$A^c_{T(i,j)} = A^c_{T(i,j)} + C_1^2 - C_1^3 - S_p^T \frac{V_e}{3} \tag{F.79}$$

$$A^{con}_{(i,j)} = A^{con}_{(i,j)} + \frac{V_e}{3c_p}\left(S_c^T + u_{av}\sum_{m=1}^{3} D_m^x p_m + v_{av}\sum_{m=1}^{3} D_m^y p_m + \Phi_c\right) \tag{F.80}$$

With respect to node $(i+1,j)$:

$$A^c_{T(i+1,j)} = A^c_{T(i+1,j)} + C_2^3 - C_2^1 - S_p^T \frac{V_e}{3} \tag{F.81}$$

$$A^{con}_{(i+1,j)} = A^{con}_{(i+1,j)} + \frac{V_e}{3c_p}\left(S_c^T + u_{av}\sum_{m=1}^{3} D_m^x p_m + v_{av}\sum_{m=1}^{3} D_m^y p_m + \Phi_c\right) \tag{F.82}$$

With respect to node $(i+1,j+1)$:

$$A^c_{T(i+1,j+1)} = A^c_{T(i+1,j+1)} + C_3^1 - C_3^2 - S_p^T \frac{V_e}{3} \tag{F.83}$$

$$A^{con}_{(i+1,j+1)} = A^{con}_{(i+1,j+1)} + \frac{V_e}{3c_p}\left(S_c^T + u_{av}\sum_{m=1}^{3} D_m^x p_m + v_{av}\sum_{m=1}^{3} D_m^y p_m + \Phi_c\right) \tag{F.84}$$

For the type 2 and quad 1 element of Fig. 3.4, the following coefficients must be evaluated:

With respect to node (i, j):

$$A^c_{T(i,j)} = A^c_{T(i,j)} + C^2_1 - C^3_1 - S^T_p \frac{V_e}{3} \tag{F.85}$$

$$A^{con}_{(i,j)} = A^{con}_{(i,j)} + \frac{V_e}{3c_p}\left(S^T_c + u_{av}\sum_{m=1}^{3} D^x_m p_m + v_{av}\sum_{m=1}^{3} D^y_m p_m + \Phi_c\right) \tag{F.86}$$

With respect to node $(i+1, j+1)$:

$$A^c_{T(i+1,j+1)} = A^c_{T(i+1,j+1)} + C^3_2 - C^1_2 - S^T_p \frac{V_e}{3} \tag{F.87}$$

$$A^{con}_{(i+1,j+1)} = A^{con}_{(i+1,j+1)} + \frac{V_e}{3c_p}\left(S^T_c + u_{av}\sum_{m=1}^{3} D^x_m p_m + v_{av}\sum_{m=1}^{3} D^y_m p_m + \Phi_c\right) \tag{F.88}$$

With respect to node $(i, j+1)$:

$$A^c_{T(i,j+1)} = A^c_{T(i,j+1)} + C^1_3 - C^2_3 - S^T_p \frac{V_e}{3} \tag{F.89}$$

$$A^{con}_{(i,j+1)} = A^{con}_{(i,j+1)} + \frac{V_e}{3c_p}\left(S^T_c + u_{av}\sum_{m=1}^{3} D^x_m p_m + v_{av}\sum_{m=1}^{3} D^y_m p_m + \Phi_c\right) \tag{F.90}$$

For the type 1 and quad 2 element of Fig. 3.4, the following coefficients must be evaluated:

With respect to node $(i+1, j)$:

$$A^c_{T(i+1,j)} = A^c_{T(i+1,j)} + C^2_1 - C^3_1 - S^T_p \frac{V_e}{3} \tag{F.91}$$

$$A^{con}_{(i+1,j)} = A^{con}_{(i+1,j)} + \frac{V_e}{3c_p}\left(S^T_c + u_{av}\sum_{m=1}^{3} D^x_m p_m + v_{av}\sum_{m=1}^{3} D^y_m p_m + \Phi_c\right) \tag{F.92}$$

With respect to node $(i, j+1)$:

$$A^c_{T(i,j+1)} = A^c_{T(i,j+1)} + C^3_2 - C^1_2 - S^T_p \frac{V_e}{3} \tag{F.93}$$

$$A^{con}_{(i,j+1)} = A^{con}_{(i,j+1)} + \frac{V_e}{3c_p}\left(S^T_c + u_{av}\sum_{m=1}^{3} D^x_m p_m + v_{av}\sum_{m=1}^{3} D^y_m p_m + \Phi_c\right) \tag{F.94}$$

With respect to node (i,j):

$$A^c_{T(i,j)} = A^c_{T(i,j)} + C^1_3 - C^2_3 - S^T_p \frac{V_e}{3} \tag{F.95}$$

$$A^{con}_{(i,j)} = A^{con}_{(i,j)} + \frac{V_e}{3c_p}\left(S^T_c + u_{av}\sum_{m=1}^{3} D^x_m p_m + v_{av}\sum_{m=1}^{3} D^y_m p_m + \Phi_c\right) \tag{F.96}$$

For the type 2 and quad 2 element of Fig. 3.4, the following coefficients must be evaluated:

With respect to node $(i+1,j)$:

$$A^c_{T(i+1,j)} = A^c_{T(i+1,j)} + C^2_1 - C^3_1 - S^T_p \frac{V_e}{3} \tag{F.97}$$

$$A^{con}_{(i+1,j)} = A^{con}_{(i+1,j)} + \frac{V_e}{3c_p}\left(S^T_c + u_{av}\sum_{m=1}^{3} D^x_m p_m + v_{av}\sum_{m=1}^{3} D^y_m p_m + \Phi_c\right) \tag{F.98}$$

With respect to node $(i+1,j+1)$:

$$A^c_{T(i+1,j+1)} = A^c_{T(i+1,j+1)} + C^3_2 - C^1_2 - S^T_p \frac{V_e}{3} \tag{F.99}$$

$$A^{con}_{(i+1,j+1)} = A^{con}_{(i+1,j+1)} + \frac{V_e}{3c_p}\left(S^T_c + u_{av}\sum_{m=1}^{3} D^x_m p_m + v_{av}\sum_{m=1}^{3} D^y_m p_m + \Phi_c\right) \tag{F.100}$$

With respect to node $(i,j+1)$:

$$A^c_{T(i,j+1)} = A^c_{T(i,j+1)} + C^1_3 - C^2_3 - S^T_p \frac{V_e}{3} \tag{F.101}$$

$$A^{con}_{(i,j+1)} = A^{con}_{(i,j+1)} + \frac{V_e}{3c_p}\left(S^T_c + u_{av}\sum_{m=1}^{3} D^x_m p_m + v_{av}\sum_{m=1}^{3} D^y_m p_m + \Phi_c\right) \tag{F.102}$$

When these coefficients have been evaluated and assembled for every element in the calculation domain, the final form of the discretized energy equation for each node is obtained as follows:

$$\begin{aligned} A^c_{T(i,j)}T_{(i,j)} &= A^e_{T(i,j)}T_{(i+1,j)} + A^{ne}_{T(i,j)}T_{(i+1,j+1)} \\ &+ A^n_{T(i,j)}T_{(i,j+1)} + A^{nw}_{T(i,j)}T_{(i-1,j+1)} \\ &+ A^w_{T(i,j)}T_{(i-1,j)} + A^{sw}_{T(i,j)}T_{(i-1,j-1)} \\ &+ A^s_{T(i,j)}T_{(i,j-1)} + A^{se}_{T(i,j)}T_{(i+1,j-1)} \\ &+ A^{con}_{(i,j)} \end{aligned} \tag{F.103}$$

Equation (F.103) may be written in the following compact form:

$$a_i^T T_i = \sum_n a_n^T T_n + b_i^T \tag{F.104}$$

where the summation is over the eight nodes that are neighbouring node i, or (i,j), in Fig. 3.5. The discretized energy equation, therefore, involves nine temperature nodes.

F.4 Assembly of the Continuity Equation

In Appendix E, the mass flowing across a control volume face k within an element is written as follows:

$$\left(\begin{array}{c} \text{Integrated flux across} \\ \text{control volume face k} \end{array} \right) = \int_0^{M_k} \vec{g} \cdot \vec{n}_k \, ds = \sum_{j=1}^{3} E_j^k p_j + F^k \tag{F.105}$$

Equation (F.105) for the continuity equation is similar in form to Eq. (F.1) for the x-momentum equation, therefore, the discretized form of the continuity equation may be assembled in the same manner as the discretized momentum equations. Since the assembly procedure is similar, only the resulting coefficients are presented here.

With respect to the type 1 and quad 1 element in Fig. 3.4, the following coefficients can be evaluated when node 1 is node (i,j), node 2 is node $(i+1,j)$, and node 3 is node $(i+1,j+1)$:
With respect to node (i,j):

$$A^c_{p(i,j)} = A^c_{p(i,j)} + E^2_1 - E^3_1 \tag{F.106}$$
$$A^e_{p(i,j)} = A^e_{p(i,j)} + E^3_2 - E^2_2 \tag{F.107}$$
$$A^{ne}_{p(i,j)} = A^{ne}_{p(i,j)} + E^3_3 - E^2_3 \tag{F.108}$$
$$A^{con}_{(i,j)} = A^{con}_{(i,j)} + F^3 - F^2 \tag{F.109}$$

With respect to node $(i+1,j)$:

$$A^c_{p(i+1,j)} = A^c_{p(i+1,j)} + E^3_2 - E^1_2 \tag{F.110}$$
$$A^n_{p(i+1,j)} = A^n_{p(i+1,j)} + E^1_3 - E^3_3 \tag{F.111}$$
$$A^w_{p(i+1,j)} = A^w_{p(i+1,j)} + E^1_1 - E^3_1 \tag{F.112}$$
$$A^{con}_{(i+1,j)} = A^{con}_{(i+1,j)} + F^1 - F^3 \tag{F.113}$$

With respect to node $(i+1, j+1)$:

$$A^{c}_{p(i+1,j+1)} = A^{c}_{p(i+1,j+1)} + E^{1}_{3} - E^{2}_{3} \tag{F.114}$$

$$A^{s}_{p(i+1,j+1)} = A^{s}_{p(i+1,j+1)} + E^{2}_{2} - E^{1}_{2} \tag{F.115}$$

$$A^{sw}_{p(i+1,j+1)} = A^{sw}_{p(i+1,j+1)} + E^{2}_{1} - E^{1}_{1} \tag{F.116}$$

$$A^{con}_{(i+1,j+1)} = A^{con}_{(i+1,j+1)} + F^{2} - F^{1} \tag{F.117}$$

For the type 2 and quad 1 element of Fig. 3.4, the following coefficients can be evaluated when node 1 is node (i, j), node 2 is node $(i+1, j+1)$, and node 3 is node $(i, j+1)$:
With respect to node (i, j):

$$A^{c}_{p(i,j)} = A^{c}_{p(i,j)} + E^{2}_{1} - E^{3}_{1} \tag{F.118}$$

$$A^{ne}_{p(i,j)} = A^{ne}_{p(i,j)} + E^{3}_{2} - E^{2}_{2} \tag{F.119}$$

$$A^{n}_{p(i,j)} = A^{n}_{p(i,j)} + E^{3}_{3} - E^{2}_{3} \tag{F.120}$$

$$A^{con}_{(i,j)} = A^{con}_{(i,j)} + F^{3} - F^{2} \tag{F.121}$$

With respect to node $(i+1, j+1)$:

$$A^{c}_{p(i+1,j+1)} = A^{c}_{p(i+1,j+1)} + E^{3}_{2} - E^{1}_{2} \tag{F.122}$$

$$A^{w}_{p(i+1,j+1)} = A^{w}_{p(i+1,j+1)} + E^{1}_{3} - E^{3}_{3} \tag{F.123}$$

$$A^{sw}_{p(i+1,j+1)} = A^{sw}_{p(i+1,j+1)} + E^{1}_{1} - E^{3}_{1} \tag{F.124}$$

$$A^{con}_{(i+1,j+1)} = A^{con}_{(i+1,j+1)} + F^{1} - F^{3} \tag{F.125}$$

With respect to node $(i, j+1)$:

$$A^{c}_{p(i,j+1)} = A^{c}_{p(i,j+1)} + E^{1}_{3} - E^{2}_{3} \tag{F.126}$$

$$A^{s}_{p(i,j+1)} = A^{s}_{p(i,j+1)} + E^{2}_{1} - E^{1}_{1} \tag{F.127}$$

$$A^{e}_{p(i,j+1)} = A^{e}_{p(i,j+1)} + E^{2}_{2} - E^{1}_{2} \tag{F.128}$$

$$A^{con}_{(i,j+1)} = A^{con}_{(i,j+1)} + F^{2} - F^{1} \tag{F.129}$$

For the type 1 and quad 2 element in Fig. 3.4, the following coefficients can be evaluated when node 1 is node $(i+1, j)$, node 2 is node $(i, j+1)$, and node 3 is node (i, j):
With respect to node $(i+1, j)$:

$$A^{c}_{p(i+1,j)} = A^{c}_{p(i+1,j)} + E^{2}_{1} - E^{3}_{1} \tag{F.130}$$

$$A^{nw}_{p(i+1,j)} = A^{nw}_{p(i+1,j)} + E^3_2 - E^2_2 \quad \text{(F.131)}$$
$$A^{w}_{p(i+1,j)} = A^{w}_{p(i+1,j)} + E^3_3 - E^2_3 \quad \text{(F.132)}$$
$$A^{con}_{(i+1,j)} = A^{con}_{(i+1,j)} + F^3 - F^2 \quad \text{(F.133)}$$

With respect to node $(i, j+1)$:

$$A^{c}_{p(i,j+1)} = A^{c}_{p(i,j+1)} + E^3_2 - E^1_2 \quad \text{(F.134)}$$
$$A^{se}_{p(i,j+1)} = A^{se}_{p(i,j+1)} + E^1_1 - E^3_1 \quad \text{(F.135)}$$
$$A^{s}_{p(i,j+1)} = A^{s}_{p(i,j+1)} + E^1_2 - E^3_2 \quad \text{(F.136)}$$
$$A^{con}_{(i,j+1)} = A^{con}_{(i,j+1)} + F^1 - F^3 \quad \text{(F.137)}$$

With respect to node (i, j):

$$A^{c}_{p(i,j)} = A^{c}_{p(i,j)} + E^1_3 - E^2_3 \quad \text{(F.138)}$$
$$A^{e}_{p(i,j)} = A^{e}_{p(i,j)} + E^2_1 - E^1_1 \quad \text{(F.139)}$$
$$A^{n}_{p(i,j)} = A^{n}_{p(i,j)} + E^2_2 - E^1_2 \quad \text{(F.140)}$$
$$A^{con}_{(i,j)} = A^{con}_{(i,j)} + F^2 - F^1 \quad \text{(F.141)}$$

For the type 2 and quad 2 element of Fig. 3.4, the following coefficients can be evaluated when node 1 is node $(i+1, j)$, node 2 is node $(i+1, j+1)$, and node 3 is node $(i, j+1)$:
With respect to node $(i+1, j)$:

$$A^{c}_{p(i+1,j)} = A^{c}_{p(i+1,j)} + E^2_1 - E^3_1 \quad \text{(F.142)}$$
$$A^{n}_{p(i+1,j)} = A^{n}_{p(i+1,j)} + E^3_2 - E^2_2 \quad \text{(F.143)}$$
$$A^{nw}_{p(i+1,j)} = A^{nw}_{p(i+1,j)} + E^3_3 - E^2_3 \quad \text{(F.144)}$$
$$A^{con}_{(i+1,j)} = A^{con}_{(i+1,j)} + F^3 - F^2 \quad \text{(F.145)}$$

With respect to node $(i+1, j+1)$:

$$A^{c}_{p(i+1,j+1)} = A^{c}_{p(i+1,j+1)} + E^3_2 - E^1_2 \quad \text{(F.146)}$$
$$A^{w}_{p(i+1,j+1)} = A^{w}_{p(i+1,j+1)} + E^1_3 - E^3_3 \quad \text{(F.147)}$$
$$A^{s}_{p(i+1,j+1)} = A^{s}_{p(i+1,j+1)} + E^1_1 - E^3_1 \quad \text{(F.148)}$$
$$A^{con}_{(i+1,j+1)} = A^{con}_{(i+1,j+1)} + F^1 - F^3 \quad \text{(F.149)}$$

With respect to node $(i, j+1)$:

$$A^c_{p(i,j+1)} = A^c_{p(i,j+1)} + E^1_3 - E^2_3 \tag{F.150}$$

$$A^{se}_{p(i,j+1)} = A^{se}_{p(i,j+1)} + E^2_1 - E^1_1 \tag{F.151}$$

$$A^e_{p(i,j+1)} = A^e_{p(i,j+1)} + E^2_2 - E^1_2 \tag{F.152}$$

$$A^{con}_{(i,j+1)} = A^{con}_{(i,j+1)} + F^2 - F^1 \tag{F.153}$$

When these coefficients have been evaluated and assembled for every element in the calculation domain, the final form of the discretized continuity equation for each node is obtained as follows:

$$\begin{aligned} A^c_{p(i,j)} p_{(i,j)} &= A^e_{p(i,j)} p_{(i+1,j)} + A^{ne}_{p(i,j)} p_{(i+1,j+1)} \\ &+ A^n_{p(i,j)} p_{(i,j+1)} + A^{nw}_{p(i,j)} p_{(i-1,j+1)} \\ &+ A^w_{p(i,j)} p_{(i-1,j)} + A^{sw}_{p(i,j)} p_{(i-1,j-1)} \\ &+ A^s_{p(i,j)} p_{(i,j-1)} + A^{se}_{p(i,j)} p_{(i+1,j-1)} \\ &+ A^{con}_{(i,j)} \end{aligned} \tag{F.154}$$

Comparison of Eq. (F.154) with Fig. 3.5 shows that all of the nodes neighbouring node (i, j) make a contribution to the discretization equation. Equation (F.154) may be written in the following compact form:

$$a^p_i p_i = \sum_n a^p_n p_n + b^p_i \tag{F.155}$$

where the summation is over the eight nodes that are neighbouring node i, or (i, j), in Fig. 3.5. The discretized continuity equation, therefore, involves nine pressure nodes. Equation (F.154) includes the maximum number of neighbour coefficients: for nodes with less connections, the appropriate coefficients will have value zero.